PhD Thesis

Quantum effects of thermoelectricity in two-dimensional materials

(二次元物質における熱電特性の量子効果)

Nguyen Tuan Hung

Department of Physics
Graduate School of Science
Tohoku University
2018

Acknowledgments

I would like to use this opportunity to thank the many people who contributed to this thesis over the two years and haft of my PhD course study at Tohoku University. First of all, I am very grateful to my supervisor, Professor Riichiro Saito, for his teaching me fundamentals of research, basic ideas in solid state physics, proper English usage, and also scientist attitudes. I really appreciate his patience with my bad language ability and my bad understanding of even simple facts in physics. He has also inspired me to pursue physics with many new insights and thoughts, which I have never learned before. I would like to thank our collaborator Professor Mildred S. Dresselhaus (MIT) for her kind advices for thermoelectricity. I'll never forget the first time to discuss with her in thermoelectric field at Sendai in 2016. After that discussion, we have published the first two articles in Physical Review about thermoelectricity of low-dimensional materials. I also would like to thank Professor Teng-Yang and Professor Li-Chang Yin (IMR, CAS) for many discussions not only in thermoelectricity but also in battery. I would like to express my gratitude to Professor A. R. T. Nugraha for teaching me (again) proper English usage and physics. He is also a very important co-author in many our papers, we have had a lot of discussions to improve our work. For all of my lab mates: Hasdeo-san, Shoufie-san, Shirakura-san, Tatsumi-san, it has been a great time to work with you all.

I am very thankful to Interdepartmental Doctoral Degree Program for Multidimensional Materials Science Leaders (MD Program) in Tohoku University for financially supporting my study. I also would like to thank the International Graduate Program for Advanced Science (IGPAS) in Tohoku University, and thank the Japan Society for the Promotion of Science (JSPS) for supporting the scholarship (DC2) and the JSPS KAKENHI (Grant No. JP18J10151). Finally, above all else, I would like to say thank you to my family whom unwavering love carries me through all of life's adventures. No matter what happens, they are always there. I would especially appreciate a woman who give the meaning to my life, Trang, my lovely wife who is the most gentle and loyal woman I have ever seen. Her endless love and support make the every moment of my life give me motivation to make our life happier.

Contents

Chapter 1

Introduction

1.1 Purpose of the study

Thermoelectricity is the simplest technology applicable and environmentally friendly solution for direct heat-to-electricity energy conversion. A typical thermoelectric (TE) module is composed of n-type and p-type semiconductors connected electrically by metallic conductive contact pads. When a temperature gradient is applied to a TE module, the charge carriers at the hot side tend to diffuse to the cold side, producing an electrical voltage. Since these TE generators have no moving parts, they are small and quite reliable. It is why they are used in some spacecraft (like Voyager, Cassini, and others). However, the TE is not a very efficient device due to their small power factor (PF) and figure of merit (ZT) values, which are key parameter for describing the performance of TE materials. The PF and ZT depends on the electrical conductivity, the Seebeck coefficient, and the thermal conductivity. In order to increase the PF and ZT values, a theory to confined the electrons using low-dimensional materials was proposed by Prof. Dresselhaus (MIT, USA) in 1993 [1, 2]. This general theory showed that the TE power factor is enhanced by the confinement effect, which is determined by the effective size of the electron wave functions in the nonprincipal direction for low-dimensional materials, such as the thickness in thin films and the diameter in nanowires. The Dresselhaus theory has really spurred the development of the TE over the last 25 years. Since 1993, TE field has made a lot of progress on low-dimensional nanostructure and their applications in TE. However, they also noticed that some common materials such as Si nanowires did not show enhancement of the PF although their confinement length is sufficiently small [3, 4]. Recently, we proposed a update theory for the Dresselhaus theory, which can answer the question that why the Dresselhaus theory fails in some exceptional materials. By theoretically investigate the PF of the low-dimensional semiconductors, we found that the PF is enhanced only when the confinement length is smaller than the thermal de Broglie wavelength, which about 5-100 nm depends on the effective mass of electron. Since it might be difficult for experimentalists to obtain one-dimensional nanowires with diameters down to few nanometers, the two-dimensional (2D) monolayer materials with extremely small thickness (~ 1 nm) are naturally a good candidate as a thermoelectric material. *However*, the thermoelectric performance of 2D materials still need to be improved for industrial applications, which requires a ZT value > 2 at room temperature.

The *purpose* of this thesis is to find new strategies to improve the thermoelectric performance in 2D materials including monolayer InSe and tetradymites (Bi_2Se_3, Bi_2Te_2Se, and Bi_2Te_2S). This thesis also presents a new dimensionless parameter consisting of the optimum PF and lattice thermal conductivity (without electronic thermal conductivity), it is possible to unify optimum ZT of both bulk and low-dimensional semiconductors into a single universal curve that covers many materials with different dimensionalities.

1.2 Organization

This thesis is organized into five chapters. Chapters 1 and 2 form basic information of this thesis. In the remaining part of Chapter 1, we explain the background of the study. In Chapter 2, we review the fundamentals of transport properties of low-dimensional semiconductors and explain the methods we use in this study, the so-called one-band and two-band models. We also introduce the density functional theory (DFT) calculations for electrical and thermal conductivities. In Chapter 3, we review a quantum effect in thermoelectricity of low-dimensional materials. The main results of this thesis are presented in Chapters 4, 5 and 6. In Chapter 4, we show calculated results for the thermoelectric performance of 2D InSe. In Chapter 5, we show calculated results for the power factor and figure of merit of 2D tetradymites (Bi_2Se_3, Bi_2Te_2Se, and Bi_2Te_2S). In Chapter 6, we show an universal curve of optimum thermoelectric figure of merit for bulk and low-dimensional materials. Finally, in Chapter 7, a summary of this thesis is given.

1.3 Backgrounds

In this section, we review some backgrounds in the thermoelectric field that motivate the present work. We will discuss the fundamental effects of thermoelectricity including the Seebeck effect and the Peltier effect. Then, we show some general concepts on thermoelectric devices, such as the power factor PF, the figure-of-merit ZT, and the output power density Q. Finally we briefly discuss the enhancement mechanisms and strategies for higher performance thermoelectric materials.

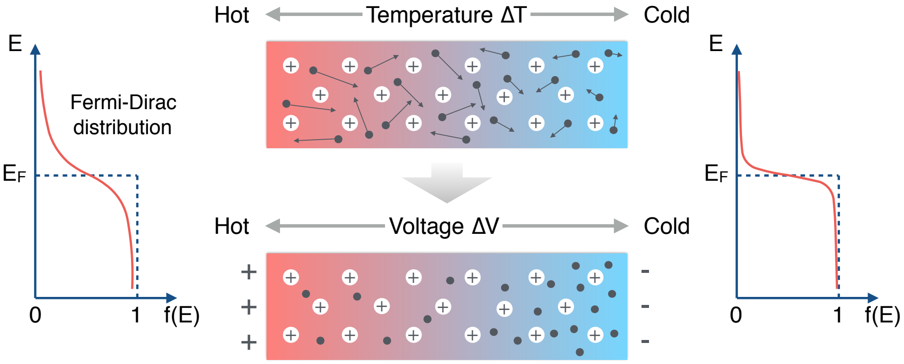

Figure 1.1 Illustration of the Seebeck effect. By moving electron from left to right, voltage appears.

1.3.1 Entangling heat and charge

Thermoelectricity was discovered experimentally in 1821 by a German physicist, Thomas Johann Seebeck. It is thus not surprising that the thermoelectric coefficient is called as the Seebeck coefficient S, but often it is also referred to as thermoelectric power (TEP) or thermopower. T. J. Seebeck made an important observation. After connecting a bismuth wire to an antimony wire, he found a voltage between the two free ends of the pair of wires by heating the junction region between the two wires. This was the first thermoelectric effect with electricity. The Seebeck coefficient, S, is defined by how much voltage difference, ΔV, develops in response to the applied temperature gradient ΔT, which can be expressed as

$$S = -\frac{\Delta V}{\Delta T}. \tag{1.1}$$

The units of the Seebeck coefficient is volts per kelvin (V/K) in SI units.

The origin of the voltage in the Seebeck effect can be understood by the following simple explanation. Imagine a semiconductor (or metal) wire whose one end is touched to a cold source and the other in a hot source, as shown in Fig. 1.1. There is a large distribution charge of the carrier above the Fermi energy, E_{F}, at the hot region based on the Fermi-Dirac distribution function as shown in Fig. 1.1 left. In contrast, there is small distribution of the carrier above E_{F} at the cold region as shown in Fig. 1.1 right. In addition, the carrier at the hot region have higher kinetic energy (KE), since the averaged value of KE $= \frac{3}{2}k_{\mathrm{B}}T$ for an ideal gas, where k_{B} is the Boltzmann constant and T is the absolute temperature. The carriers are thus more agile than those at the cold region. Therefore, the carriers (either electrons or holes) will flow from the hot region to the cold region, which may generate a voltage difference ΔV in the semiconductor wire [Fig. 1.1]. However, if the electrons and holes move in the same direction, we do

---

Fig. 1.1: Fig/chapter1-fig1.pdf

not get the net electronic current because they will cancel each other. Thermoelectric devices are thus made by two types (n-type and p-type) of semiconductor [Fig. 1.2], which allow major electrons (n-type) or holes (p-type) moving.

The second thermoelectric effect, which is the inverse of the Seebeck effect, was discovered in 1834 by a French physicist Jean-Charles Peltier. While the Seebeck effect can occurs in a single wire of conducting material, the Peltier effect is observed when two different conductors are brought together at a junction. By passing a direct current I through the two junctions, it can create a temperature difference between the two junctions. This effect may sound similar to Joule heating, which is the generation of heat by passing an electric current through a metal, but in fact it is not. In Joule heating, the current is only increasing the temperature in the material in which it flows. However, in Peltier effect devices, a temperature difference is created, i.e., one junction becomes cooler and the other junction becomes hotter. Generation of the heat $\pm Q$ per unit time occurs at the two junctions depending on the direction of the electric current. The Peltier coefficient, Π, is defined by [5]

$$\Pi = -\frac{Q}{I}. \tag{1.2}$$

The units of the Peltier coefficients is the volts (V) in SI units. Twenty years later, William Thomson (the future Lord Kelvin) argued that Seebeck and Peltier effects were intimately connected and same phenomenon. The Seebeck and Peltier coefficients are related by the Kelvin relationship [5]

$$\Pi = ST, \tag{1.3}$$

which can be derived by applying irreversible thermodynamics [5].

The Seebeck effect is the basis for power-generation devices and the Peltier effect is the basis for many modern refrigeration devices. The devices are not using only one semiconductor “legs”; they use two types (n-type and p-type) of semiconductor that are connected in series (thermocouple), as shown in Figs. 1.2 (a) and (b). Negatively charged electrons carry electrical current in the n-type leg, whereas positively charged holes carry the current in the p-type leg. A thermoelectric module is built up of an array of these couples, arranged electrically in series and thermally in parallel [6], as shown in Fig. 1.2 (c).

1.3.2 Thermodynamic origin of thermoelectricity

As show in Section 1.3.1, we can explain the thermoelectric effects by using the Fermi-Dirac distribution. In this section, we will try to answer the following question: What is the basic physic picture for observing an electric field by a thermal gradient? Does we need a Fermi-Dirac distribution to explain the Seebeck effect?

Fig. 1.2: Fig/chapter1-fig2.pdf

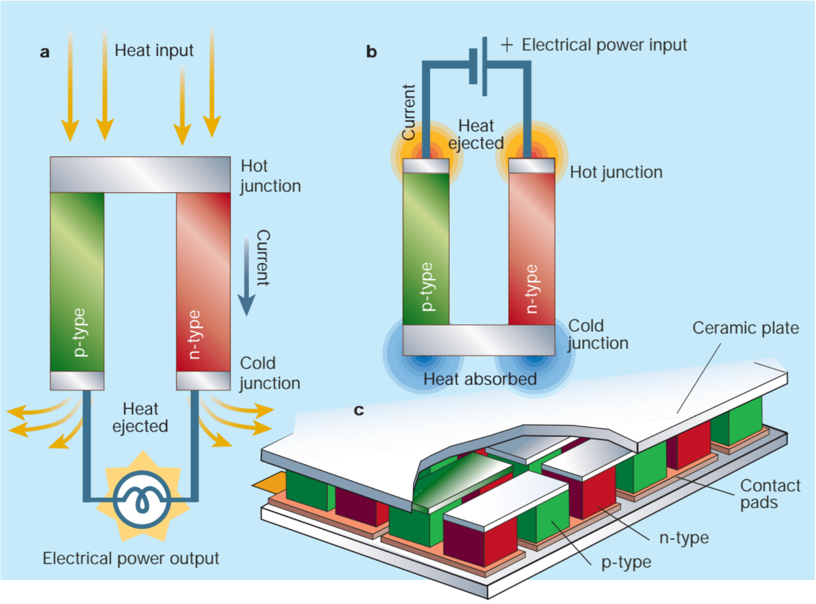

Figure 1.2 Thermoelectric devices are shown, configured for (a) power generation (Seebeck effect) or (b) refrigeration (Peltier effect). Thermocouple is a simple thermoelectric device including both the n-type and p-type semiconductors that are connected in series. (c) State-of-the-art thermoelectric modules can contain up to several thousand individual thermocouples. (Taken from graphics of S. Williams, www.thermoelectrics.com.)

The answer is YES and this answer is given by the paper which was published by Herbert Callen in 1948 [7]. In his paper, the thermoelectric effect are explained by using the first and second law of thermodynamics. In equilibrium thermodynamics, an infinitesimal change in Gibbs free energy, δG, can be expressed as

$$\delta G = T\delta\tilde{S} + \mu\delta N + p\delta V, \tag{1.4}$$

where, the entropy $\tilde{S}$, number of particle N, and volume V are extensive quantities, and the temperature T, chemical potential μ, and pressure P are intensive quantities. The extensive parameters depend on the size of the system, while the intensive ones do not. Let us neglect the $P\delta V$ term since the P and V do not play a role in the generation of thermoelectricity. To consider the energy flow in such a system, we will quantify the energy flux as the amount of energy flowing per second and per unit area:

$$\mathcal{J}^G = T\mathcal{J}^{\tilde{S}} + \mu\mathcal{J}^N, \tag{1.5}$$

where, $\mathcal{J}^{\tilde{S}}$ and $\mathcal{J}^N$ are flux densities of entropy and number of particle per second and per unit area, respectively. According Eq. (1.5), there are two ways of carrying energy from one place to the other. One way is to move a finite entropy (i.e. a finite number of configurations) at a given temperature. Another way is to displace a number of particles, each with their chemical potential. We now want to know how the system responds to a temperature gradient or a gradient of chemical potential. Let us take the divergence of Eq. (1.5):

$$\nabla \cdot \mathcal{J}^G = \nabla T \cdot \mathcal{J}^{\tilde{S}} + T\nabla \cdot \mathcal{J}^{\tilde{S}} + \nabla\mu \cdot \mathcal{J}^N + \mu\nabla \cdot \mathcal{J}^N. \tag{1.6}$$

According to *the first law of thermodynamics*, energy is conserved, that means that in any given region of the system, the flow of incoming and outgoing energy should cancel out for thermal equilibrium state. We thus have

$$\nabla \cdot \mathcal{J}^G = 0. \tag{1.7}$$

Here, we consider the system in which the number of particles is conserved, then we can take

$$\nabla \cdot \mathcal{J}^N = 0. \tag{1.8}$$

On the other hand, according to *the second law of thermodynamics*, entropy is not conserved. In contrast to the Gibbs free energy G and the particle number N in a steady-state system, entropy $\tilde{S}$ can grow with time as

$$\nabla \cdot \mathcal{J}^{\tilde{S}} = \dot{s}, \tag{1.9}$$

where $\dot{s}$ is the changing rate in entropy per volume.

With all constraints in Eqs. (1.7), (1.8), (1.9), Eq. (1.6) can be rewritten as

$$0 = \nabla T \cdot \mathcal{J}^{\tilde{S}} + T\dot{s} + \nabla\mu \cdot \mathcal{J}^N. \tag{1.10}$$

For the sake of simplicity, let us consider on the case of $\dot{s} = 0$ (no new entropy is produced as time goes on). When, we apply a gradient of the chemical potential ($\nabla\mu \neq 0$), the particles moving along or opposite to this gradient lose or gain a energy as they flow. Since each particle has a finite degree of freedom, the flow of particles is also a flow of entropy. In order to conserve the total energy, a temperature gradient ($\nabla T \neq 0$) is generated to eliminate the total energy flow from Eq. (1.10). Therefore, in any system where both energy and number of particle are conserved, a gradient in the chemical potential generates a temperature gradient and vice versa. This is the fundamental reason for the existence of the thermoelectricity in any materials. In other words, *the thermoelectricity is a consequence of the first and second laws of thermodynamics in a system with a fixed number of particles.* We note that in almost all macroscopic systems, the particles are scattered during their moving from one side of the system to the other side. Therefore, the local entropy are generated ($\dot{s} \neq 0$). For this general case, the sign and magnitude of the temperature gradient is given by balance between the change in the potential energy and the continuous production of entropy.

1.3.3 Seebeck coefficient as a measure of entropy per carrier

The Seebeck coefficient of a given material is defined as the electric field (or voltage) generated by a temperature gradient in Eq. (1.1). However, this definition does not explain physical meaning of the Seebeck coefficient. There is an alternative definition of the Seebeck coefficient that was formulated by Callen in 1948 [7]. According to the Callen's paper, *the Seebeck coefficient is the ratio of entropy flow to particle flow in the absence of a thermal gradient.* Let us consider a system as shown in Fig. 1.1, the energy per carrier is equal at any position in this system for a steady state,

$$U(T_1) + qV(T_1) = U(T_2) + qV(T_2), \tag{1.11}$$

where $U(T)$ and $V(T)$ are the energy of carrier and themoelectric voltage at temperature T, q is charge of carrier. In the limit of $T_1 \to T_2$, the Seebeck coefficient $S = -\mathrm{d}V/\mathrm{d}T$ reduces to

$$S = \left(\frac{\mathrm{d}U}{\mathrm{d}T}\right)/q, \tag{1.12}$$

$\mathrm{d}U/\mathrm{d}T$ is equal to the specific heat c per carrier. If c is linear to T (i.e., $c = \alpha T$), then the entropy $\tilde{S}$ is given by $\tilde{S} = \int c \ \mathrm{d}T/T = \int \alpha \ \mathrm{d}T = c$. Then Eq. (1.12) can be rewritten as $S = \tilde{S}/q = c/q$. Therefore, the Seebeck coefficient is *a measure of the entropy per carrier* or a measure of the number of degrees of freedom traveling carriers with itself. Since the entropy is positive, the sign of S is equal to the sign of the carrier, and thus S is negative and positive for electrons and holes, respectively.

Now we are going to see how to explain the experimental observations of S value in the metal and semiconductor by using the notion of the entropy per carrier. In particular let us discuss the reason why S values in the metals are usually smaller than $k_\mathrm{B}/e \sim 87$ µV/K. Of course, these observations can be also explained by using the Boltzmann's transport equation, which requires more complex calculations while it does not provide a simple physical picture.

For the metals, let us consider a metal as a degenerate electron gas with a temperature much less than the Fermi temperature (typically on the order of ~ 10000 K). When we heat the system from 0 K, the state of the electron does not differ much from the ground state: A few of the electron have been excited, from states *just inside* the Fermi surface ($E_\mathrm{F} - k_\mathrm{B}T \leq E < E_\mathrm{F}$) to states *just outside* ($E_\mathrm{F} < E \leq E_\mathrm{F} + k_\mathrm{B}T$), where E_F is Fermi energy. Let us consider these electrons close to the Fermi energy behave like the ideal gas, then the energy of an ideal gas is

$$U = \frac{3}{2} N k_\mathrm{B} T, \tag{1.13}$$

where N is the number of excited electron (not the total number of electrons in system). We can estimate N with the number of electrons that are within the energy interval of $\mathrm{d}E = k_\mathrm{B}T$ inside the Fermi surface, then

$$N = 2\int_{E_\mathrm{F}-k_\mathrm{B}T}^{E_\mathrm{F}+k_\mathrm{B}T} \mathcal{D}(E)f(E)\mathrm{d}E, \tag{1.14}$$

where the factor of 2 again comes from the spin states of the electrons. $\mathcal{D}$ is the density of states, and $\mathcal{D}$ at the Fermi energy as $\mathcal{D}(E_\mathrm{F}) = 3N_\mathrm{tot}/4E_\mathrm{F}$ for the case of three dimension, where N_tot is the total number of electrons. $f(E)$ is the Fermi-Dirac distribution, and inside and close to the Fermi surface, $f(E) \sim 1$. Equation (1.14) can be rewritten as

$$N \approx 2\frac{3N_\mathrm{tot}}{4E_\mathrm{F}}k_\mathrm{B}T = \frac{3}{2}N_\mathrm{tot}\frac{k_\mathrm{B}T}{E_\mathrm{F}}. \tag{1.15}$$

By inserting Eq. (1.15) into Eq. (1.13), we get the energy for the excited electrons as

$$U \approx \frac{9}{4}N_\mathrm{tot}k_\mathrm{B}\frac{k_\mathrm{B}T^2}{E_\mathrm{F}}. \tag{1.16}$$

The electronic heat capacity per carrier is then

$$c \approx \frac{1}{N_\mathrm{tot}}\frac{\mathrm{d}U}{\mathrm{d}T} = \frac{9}{4}k_\mathrm{B}\frac{k_\mathrm{B}T}{E_\mathrm{F}}. \tag{1.17}$$

The Seebeck coefficient for a metal is thus given by

$$S = \frac{c}{e} \approx \frac{9}{4}\frac{k_\mathrm{B}}{e}\frac{k_\mathrm{B}T}{E_\mathrm{F}} \ll \frac{k_\mathrm{B}}{e} \approx 87\ \mu\mathrm{V/K}. \tag{1.18}$$

Thus the characteristic S of a metal decreases with decreasing temperature and is much smaller than k_B/e. It is much less than $S \approx 3/2(k_\mathrm{B}/e)$ which is the case of the classical electron gas [8].

For a semiconductor, on the other hand, we consider a simplest case with only one type of carrier, say electrons in the conduction band (n-type). The energy of the electrons is essentially given by the half of energy band gap $E_g/2$. The "heat" of a carrier is the difference in its energy from the chemical potential $\mu \approx E_\mathrm{F}$, i.e., "heat" $= \langle E - \mu \rangle \sim E_g - \mu \sim E_g/2$. The Seebeck coefficient for a semiconductor is thus given by

$$S \approx \frac{E_g/2}{eT} \approx \frac{k_\mathrm{B}}{e}\frac{E_g}{2k_\mathrm{B}T} \gg \frac{k_\mathrm{B}}{e} \approx 87\ \mu\mathrm{V/K}. \tag{1.19}$$

Therefore, the characteristic of S for a semiconductor is much larger than 87 µV/K and S increases with decreasing temperature. Since the Seebeck coefficient is a kind of entropy, one might expect that it must go to zero as $T \to 0$. However, if there are no carriers then their entropy does not matter. Thus the real requirement of the third law of thermodynamics is $\lim_{T\to 0} \sigma S = 0$, where σ is electrical conductivity of carrier. A semiconductor for example has divergent S when $T \to 0$, but a faster decrease in σ when $T \to 0$.

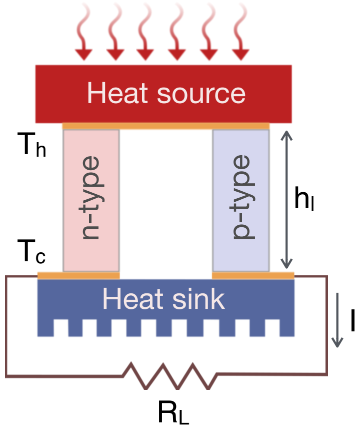

Figure 1.3 A thermoelectric power generator consists of two semiconductors (n-type and p-type). In a temperature gradient, electrons and holes tend to move from the hot to the cold side, which generates a voltage.

1.3.4 Power factor PF and figure of merit ZT

In section 1.3.1, 1.3.2 and 1.3.3, we discussed the Seebeck coefficient and its thermodynamics origin. In this section, we will discuss which parameters are important for a thermoelectric devices. A thermoelectric device should be operated at maximum power and/or maximum efficiency. In applications where the heat source is essentially free of charge (e.g., solar heat, nuclear power, or waste-heat from cars), the minimum cost of generating total power is achieved by operating at maximum power [9]. On the other hand, when heat source is expensive (e.g., fossil fuel combustion), the maximum efficiency is important to reduce the cost of generating power. For maximizing the power or the efficiency, it is required to optimize the electrical power density Q or the figure of merit ZT, respectively.

The electrical power P_{out} or the Joule heat delivered to the load as shown in Fig. 1.3 is given by

$$P_{\mathrm{out}} = I^2 R_L, \tag{1.20}$$

where I is the electric current and R_L is the resistance of the load. The units of P_{out} is the watt (W) in SI units. If we ignore the thermal and electrical contact resistance, the current I is induced by the Seebeck effect

$$I = \frac{S(T_h - T_c)}{R_L + R}, \tag{1.21}$$

where, $S = S_p - S_n$ and $R = R_p + R_n$ represent the Seebeck coefficient and resistivity of the thermocouple (p-type and n-type legs) in the thermoelectric device. T_h and T_c are the temperatures at the hot and cold sites, respectively. Here, we assume that S

Fig. 1.3: Fig/chapter1-fig3.pdf

and R are constants, and T_h and T_c are given by the boundary condition. We can now determine the maximum output power as a function of R_L from Eqs. (1.20) and (1.21) by solving $\mathrm{d}(P_{\text{out}})/\mathrm{d}(R_L) = 0$. The maximum out power, $P_{\max}$, is found to be

$$P_{\max} = \frac{1}{4}\frac{S^2(T_h - T_c)^2}{R}, \tag{1.22}$$

which occurs the case that the load resistance is $R_L = R$. The electrical resistance of the thermocouple ($R = h_l/\sigma A$) can be written in terms of the thermocouple geometry (that is sum of cross-sectional areas for the n-type and p-type legs $A = A_p + A_n$ and leg length $h_l = h_p = h_n$) and the electrical conductivity, $\sigma = \sigma_p\sigma_n/(\sigma_p + \sigma_n)$, of the thermocouple. Using σ and A, Eq. (1.22) can then be written by

$$P_{\max} = \frac{1}{4h_l}S^2\sigma(T_h - T_c)^2 A. \tag{1.23}$$

In Eq. (1.23), the term $S^2\sigma$ is known as the power factor $\mathrm{PF} = S^2\sigma$. Out power density Q is defined by

$$Q = \frac{P_{\max}}{A} = \frac{1}{4h_l}\mathrm{PF}(T_h - T_c)^2, \tag{1.24}$$

The units of Q for the thermocouple is the watt per unit area (W/m^2). Equation (1.24) shows that high PF is required for optimizing Q. The output power density can increased, too, by decreasing the leg h_l of the thermocouple.

Now let us consider the heat flow into the hot side, P_{in}, which consists of three components. They are: (1) the heat flow through the thermoelectric material due to the thermal conductance of the material (P_{cond}), (2) the absorbed heat at the hot junction due to the Peltier effect (P_{Pelt}), and (3) the heat that arrives at the hot side due to the Joule heating of the thermocouple with the assumption that half of this heat goes to the hot side and the other half to the cold side (P_{Joule}). We can write as

$$P_{\text{in}} = P_{\text{cond}} + P_{\text{Pelt}} - P_{\text{Joule}} = \kappa\frac{A}{h_l}(T_h - T_c) + SIT_h - \frac{1}{2}I^2R, \tag{1.25}$$

where $\kappa = \kappa_p\kappa_n/(\kappa_p + \kappa_n)$ is the thermal conductivity of the thermocouple (p-type and n-type legs).

Since the output power and the input power are both observed, the efficiency can be computed. The efficiency η of a thermoelectric generation device is measured as the ratio of output power delivered to the load (P_{out}) to the heat flow into the hot side of the thermocouple (P_{in}).

$$\eta = \frac{P_{\text{out}}}{P_{\text{in}}}. \tag{1.26}$$

In the case of maximum of power output ($P_{\max}$), and substituting Eqs. (1.22) and (1.25) into Eq. (1.26), η can be expressed as

$$\eta = \frac{T_h - T_c}{\dfrac{3T_h + T_c}{2} + \dfrac{4}{Z}}. \tag{1.27}$$

where Z is given by

$$Z = \frac{S^2\sigma}{\kappa}. \tag{1.28}$$

The quantity Z is intrinsically determined by the physical properties of the thermocouple. However, $R_L = R$, that is the condition for $P_{\max}$, is not the condition for maximizing efficiency. If we denote $m = R_L/R$ and substituting Eqs. (1.20), (1.21), and (1.25) into Eq. (1.26), then η is generally expressed as

$$\eta = \frac{T_h - T_c}{T_h} \frac{\dfrac{m}{1+m}}{1 + \dfrac{1+m}{T_h Z} - \dfrac{T_h - T_c}{2T_h(1+m)}}. \tag{1.29}$$

We can see from Eq. (1.29), η is a function of the temperatures at the hot and cold junctions, of Z, and of m. By solving $\mathrm{d}(\eta)/\mathrm{d}(m) = 0$, the maximum efficiency is given by

$$\eta_{\max} = \frac{T_h - T_c}{T_h} \frac{\sqrt{1+ZT} - 1}{\sqrt{1+ZT} + \dfrac{T_h}{T_c}}, \tag{1.30}$$

whereas the corresponding value for m is $m = \sqrt{1+ZT}$. Here, the average temperature T of the hot and cold side is defined by

$$T = \frac{T_h + T_c}{2}. \tag{1.31}$$

The unit of Z is (1/K), but the commonly used combined quantity ZT is dimensionless. It is then named the (dimensionless) figure-of-merit, which can be rewritten as

$$ZT = \frac{\mathrm{PF}}{\kappa} T, \tag{1.32}$$

One realizes that the larger ZT is the higher efficiency. Equations (1.24) and (1.30) show that increasing the PF value is important to enhance not only Q but also ZT for power generation applications, respectively.

1.3.5 Enhancement mechanisms and strategies for higher performance thermoelectric materials

As is discussed in Section 1.3.4, the efficiency of a solid-state thermoelectric power-generator is evaluated by the power factor $\mathrm{PF} = S^2\sigma$ and the dimensionless figure of merit, $ZT = S^2\sigma\kappa^{-1}T$. A fundamental aspect in the research of thermoelectricity is the demand to maximize the PF and ZT values by having large S, high σ, and low κ. However, since the transport characteristics, σ and κ, are generally interdependent according to the Wiedemann-Franz law $\kappa/\sigma = LT$, in which $L \sim 2.44 \times 10^{-8}$ WΩK^{-2}, it has always been challenging for researchers to find materials with $ZT > 2$ at room temperature [10, 11]. Huge efforts have been dedicated to reduce κ using semiconducting materials by adopting low-dimensional structures, in which κ is dominated by phonon heat transport. For example, Boukai et al. [3] showed that experiments using Si nanowires have observed that κ can be reduced below the theoretical limit of bulk Si (0.99 W/mK) because the phonon mean free path is limited by boundary scattering in nanostructures. In their experiments, the reduction of the semiconducting nanowire diameter is likely to achieve a large enhancement in thermoelectric efficiency with $ZT > 1$ at room temperature [3, 4]. The success in reducing κ thus leads to the next challenge for increasing the thermoelectric power factor $\mathrm{PF} = S^2\sigma$.

The importance of maximizing the PF can be recognized by the fact as we discussed in Section 1.3.4 that when the heat source is unlimited, the ZT value is no longer a good parameter to evaluate the thermoelectric efficiency. In this case, the output power density Q is important to be evaluated [12, 13]. The PF term appears in the definition of Q, particularly for its maximum value, $Q_{\max} = \mathrm{PF}(T_h - T_c)^2/4h_\ell$ [Eq. (2.24)]. Since the term $(T_h - T_c)^2/4h_\ell$ is given by the boundary condition, Q is mostly affected by the PF. Therefore, increasing the PF value is important to enhance not only ZT but also Q for power generation applications.

In this thesis, we thus would like to consider several mechanisms to improve PF such as using low-dimensional materials (Chapter 3), convergence of electronic bands, in particular the two-dimensional InSe (Chapter 4) and tetradymites (Chapter 5). We also introduce a new performance parameters (Chapter 6), which show a directly relationship between the PF and ZT despite of the fact that the two quantities are generally given by different values of chemical potentials.

1.3.5.1 Low-dimensional materials

The phenomenon of thermoelectricity was first observed by Thomas Johann Seebeck in 1821. For over a century thermocouples were made from metallic conductors and though many different metals were investigated, efficiencies rarely exceeded 3% [8]. The voltage generated by the metallic thermocouples are relatively small and it is not enough to make a practical thermoelectric generator. Following the development of semiconductors in the 1950s, by replacing the metals with bulk semiconductors improved the efficiency of thermocouples by more than an order of magnitude [8]. The commercial solid-state power generation systems using bulk semiconductors have been the technology for the space missions, including the Voyager I and II probes to the outer planets and, more recently, the Cassini mission to Saturn [11]. A big improvement, but normal thermoelectric technology would still cost too much and consume too much electricity to replace that conventional generators in industry.

With the introduction of low-dimensional materials and concepts based on nanostructuring, however, the thermoelectricity field has witnessed truly dramatic growth over the past 25 years. Heremans et al. [14] have shown the evolution of the

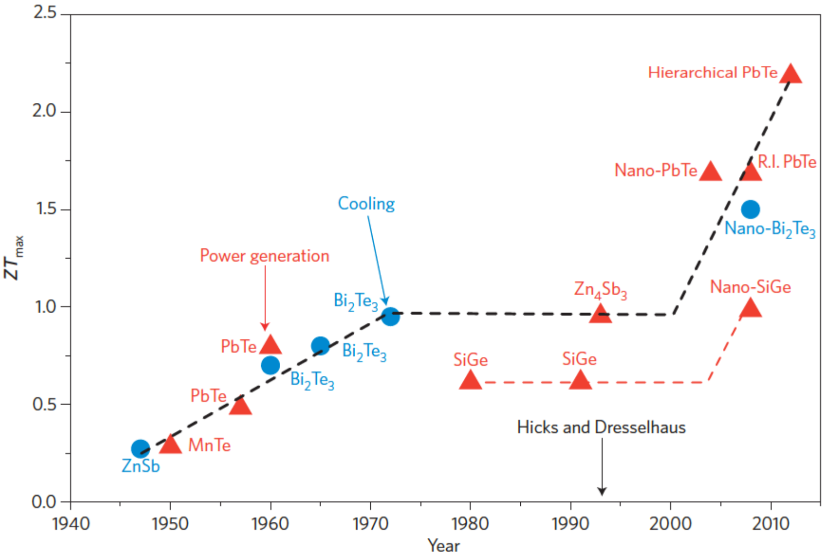

Figure 1.4 Evolution of the maximum ZT over time [Ref. [14]]. Materials for thermoelectric cooling are shown as blue dots and for thermoelectric power generation as red triangles. The material systems that have achieved $ZT > 1$ have been based on nanostructuring.

thermoelectric efficiency, which is characterized by figure-of-merit ZT value, as a function of time as shown in Fig. 1.4. It is important to note that some material systems that have achieved high ZT values have been based on nanostructuring. A theoretical study by Hicks and Dresselhaus in 1993 predicted the potential benefits of low-dimensional materials to thermoelectrics in their seminal articles [1, 2] on the modeling of thermoelectric thin films and nanowires. In these structures, electrons are confined to a physical space with lower dimensions, and the resulting density of states exhibits sharp transitions with respect to energy in particular near the Fermi energy, which is desirable for a high Seebeck coefficient. This quantum confinement effect was confirmed experimentally in 1996 using PbTe/Pb$_{1-x}$Eu$_x$Te, which exhibited a thermoelectric figure-of-merit value up to about five times greater than that of the corresponding bulk value [15]. It is thus intriguing to evaluate thermoelectricity in low-dimensional semiconductors that might have excellent thermoelectric performance, either theoretically or experimentally. *However*, if we look at some previous works more carefully into the subject of the confinement effects on the PF, there were some experiments which showed that the PF values of Si nanowires is still similar to that of the bulk values [3, 4], while other experiments on Bi nanowires show an enhanced PF values compared to its bulk state values [16]. This situation indicates that there is another parameter that can be compared with the confinement length.

In this thesis, we will show that the thermal de Broglie length is a key parameter

---

Fig. 1.4: Fig/chapter1-fig4.pdf

that defines the quantum effects in thermoelectricity (Chapter 3). In order to show these effects, we investigate the quantum confinement effects on the PF for typical low-dimensional semiconductors. By comparing the confinement length with the thermal de Broglie length, we can obtain an appropriate condition to optimize the PF.

1.3.5.2 Two-dimensional InSe

Let us discuss some particular low-dimensional materials that we discuss in this thesis including 2D InSe (Chapter 4) and 2D tetradymites (Chapter 5). Recent advances in the fabrication and characterization of 2D materials such as the transition metal dichalcogenides (TMDs), black phosphorus (BP), and group III chalcogenides have allowed researchers to look up unique electronic properties of the materials and utilize them in various electronic applications [17, 18, 19]. Research on thermoelectricity, which is intended to convert waste heat into electric energy, should also benefit from the advances of the 2D materials. Unlike graphene, the TMDs, BP, and group III chalcogenides have finite values of energy band gaps that could enable the enhancement of thermoelectric properties due to the quantum confinement effects in the low-dimensional semiconductors [20]. It is thus important to predict the best thermoelectric 2D material theoretically.

The improvement of thermoelectric PF and ZT strongly depend on the optimization of electronic and thermal transport properties, in which the 2D materials may serve as a good candidate [21, 22, 23, 24, 25]. For example, using the electric-double-layer transistor configuration, it was found that the Seebeck coefficient of 2D BP reached 510 µV/K at 210 K, which is much higher than the bulk BP (340 µV/K at 300 K) [21]. Monolayer BP also exhibits a strong spatial anisotropy in electrical and thermal conductivities, which makes the ZT in the armchair direction larger than that in the zigzag direction [23]. *However*, it is known that the 2D BP reacts strongly with chemical species in air and thus the thermoelectric device can be quickly degrading. As for TMDs such as MoS_2, $MoSe_2$, WS_2 and WSe_2, these materials show thickness-dependent thermoelectric properties and maximum PF of about 0.34 and 0.15 W/K^2m for n-type monolayer $MoSe_2$ and p-type MoS_2 monolayers, respectively, which are much higher than those of bulk (0.02 and 0.03 W/K^2m for bulk n-type $MoSe_2$ and p-type MoS_2, respectively) [26].

In the family of 2D semiconductors, the band structure of monolayer group III chalcogenides such as InSe, GaSe, or GaS are rather unusual, having combination of a flat band in the top of the valence band and a parabolic band in the bottom of conduction band. This feature leads to appearance of a very sharp peak in the electronic density of states (DOS) at the top of the valence band and an almost constant DOS at the bottom of the conduction band [27, 28, 29], as shown in Fig. 1.5. A recent report by Geim's group has shown that the carrier mobility in few-layer InSe may exceed 10^3 $cm^2V^{-1}s$ at room temperature [30] as shown in Fig. 1.5. In an earlier experiment,

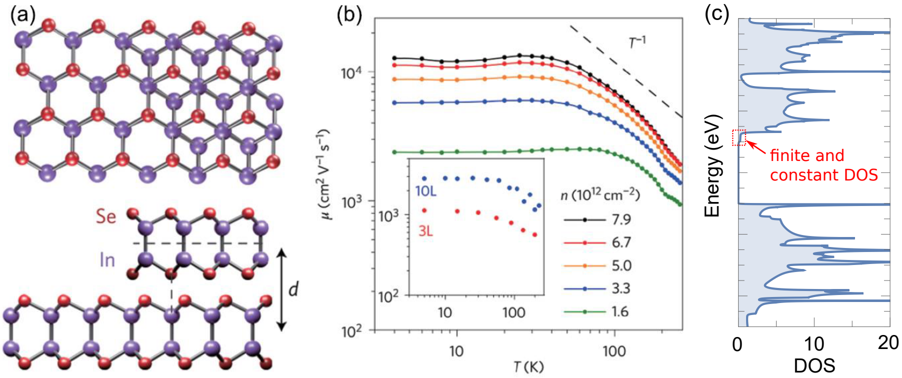

Figure 1.5 (a) Crystal structure of the two-dimensional InSe, in which purple and red spheres correspond to indium and selenium atoms, respectively. (b) T dependence of the Hall mobility μ for the 6-layers InSe [30]. (c) The density of states (DOS) of the monolayer InSe. Relatively constant DOS in the conduction band is enclosed by a dotted box [29].

Rhyee et al. showed that the bulk InSe crystal exhibits a low thermal conductivity, $\kappa < 1.2$ W/mK, at room temperature [31], and the thermal conductivity decreases with increasing temperature (0.74 W/mK at 705 K), giving $ZT = 1.48$. By using constant relaxation time in Boltzmann transport theory, Wickramaratne et al. [32], showed thickness-dependent thermoelectric properties of 2D group III chalcogenides. From these results, it seems that both the electrical and thermal transport properties of InSe are beneficial for thermoelectric performance and efficiency with both high PF and ZT. We thus expect that InSe in its 2D form could be a good thermoelectric material, which we will discuss in Chapter 4.

1.3.5.3 Two-dimensional tetradymites

Semiconductors based on heavy elements in a tetradymite structure (such as Bi_2Te_3, Sb_2Te_3, and Bi_2Se_3), as shown in Fig. 1.6, are the most investigated TE materials and have been of interest as the best ZT value for near room temperature TE applications [33]. Recently, Kim et al. [34] claimed a record $ZT \sim 1.85$ at 320 K for $Bi_{0.5}Sb_{1.5}Te_3$ nano-particles in which grain boundary and point-defect scattering suppress lattice thermal conductivity, which has the potential to revolutionize the TE industry. *However*, as the structure with a high density of dislocation arrays between grains is difficult to control in the synthesis and large volume production for industry.

On the other hand, the tetradymites have also emerged as important materials for the topological surface state, which creates additional energy levels that are available to electrons at the surface. Recent first-principles calculations show that the topological nature of the surface states remains robust with the film thickness of the

---

Fig. 1.5: Fig/chapter1-fig5.pdf

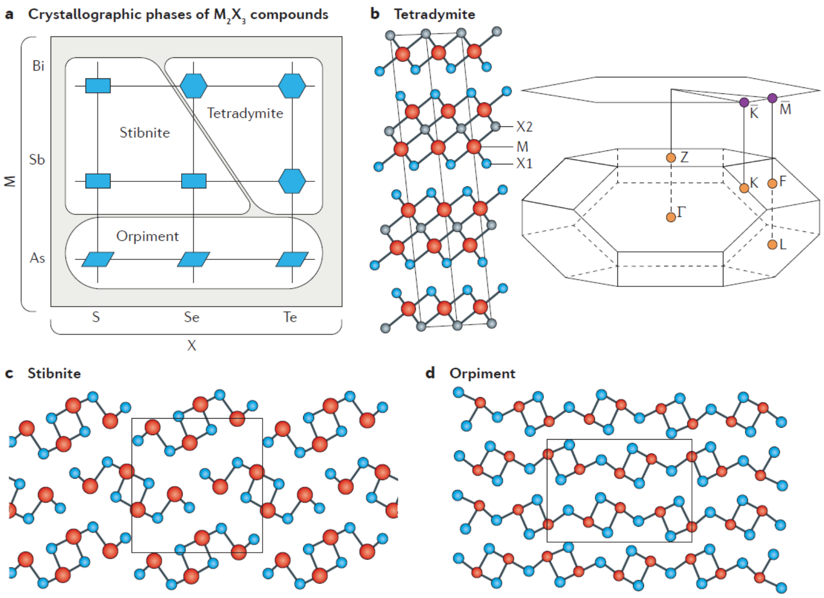

Figure 1.6 (a) Crystal structure of the tetradymite compounds M_2X_3. As the difference in electronegativity between M and X increases from the top right corner to the bottom left corner, these materials crystallize in progressively more distorted lattices, resulting in a structure evolves from tetradymite (b) to stibnite (c), and to orpiment (d) [33].

two-dimensional (2D) Bi_2Te_3 and Sb_2Te_3 [35]. In particular, for 2D tetradymites consisting of layers of five atomic planes (a quintuple layer), the surface states can exhibit the intrinsic convergence of multivalley bands, which is the most effective way to improve the TE power factor PF $= S^2\sigma$ [36]. Moreover, as expected for heavy elements and weak chemical bonds, the phonon properties of tetradymites produce a very low intrinsic $\kappa_{\rm ph}$ due to small sound velocities [33]. From these results, it seems that both the electrical and thermal transport properties of 2D tetradymites are beneficial for thermoelectric performance and efficiency with both high the PF and ZT. Recently, Sharma et al. [37] showed that the ZT value of a single quintuple layer Bi_2Te_3 is up to 0.8 and 1.4 at 300K and 500K, respectively; *however*, these ZT values are still smaller than 2 at operating temperature range of $300 - 500$ K of the industry application. Therefore, we should encourage the exploration of new thermoelectric materials in the family of 2D tetradymite compounds with $ZT > 2$ at near room temprature.

In this thesis, the two-dimensional (2D) tetradymites with M_2X_3 compounds including Bi_2Se_3, Bi_2Te_2Se, and Bi_2Te_2S are theoretically investigated for thermoelectricity in Chapter 5. We find a variety of favorable properties for high power factor in the 2D tetradymites such as small energy gaps, high group velocities, small effective masses, nonparabolic Kane bands and multi-valleys convergences. By mixtures of X elements

---

Fig. 1.6: Fig/chapter1-fig6.pdf

at the middle and surface layers, we can tune the multi-valleys convergences effect, which leads to improve the power factor whereas the lattice thermal conductivity is decreased. Our first-principles calculations show that the p-type 2D $\mathrm{Bi_2Te_2Se}$ is a promising p-type material with large PF and intrinsically low κ_{ph}, resulting in a high ZT from 1.4 to 2.0 at 300K and 500K, respectively.

1.3.5.4 Performance parameters

It is well-known that obtaining the optimum ZT (ZT_{opt}) for a certain TE material, where ZT_{opt} is defined as the maximum value of ZT as a function of the chemical potential, is often complicated by the interdependence of S, σ, and κ (see Eq. (1.32)). Therefore, finding the best material to obtain as large ZT_{opt} as possible has been a great challenge for many years. As one strategy, using low-dimensional semiconductors as discussed above. Another strategy to find the best thermoelectric materials is by defining a material parameter that can be the most essential one to determine ZT_{opt}. We can mention several efforts by researchers in the past who proposed some parameters for evaluating ZT_{opt}. For example, in 1996, Mahan and Sofo introduced a dimensionless material parameter $k_{\mathrm{B}}T/E_b$ [38], where k_{B} and E_b, are the Boltzmann constant and the energy band width, respectively. When E_b is infinitesimal, the transport distribution function $\mathcal{T} = v^2\tau\mathcal{D}$ forms a delta function that leads to the largest possible value of ZT_{opt}, where v is the carrier velocity, τ is the carrier relaxation time, and $\mathcal{D}$ is the density of states of the carrier at the Fermi energy. This work was revisited from a Landauer perspective by Jeong et al. [39], they found that a finite E_b dispersion produces a higher ZT when the lattice thermal conductivity is finite. Much earlier, in 1959, Chasmar and Stratton suggested that a parameter $B = 5.745 \times 10^{-6}(\mu/\kappa_l)(m/m_0)^{3/2}T^{5/2}$, where μ, κ_l, m, and m_0 are the carrier mobility, the lattice thermal conductivity, the carrier effective mass, and the free electron mass, respectively, determines the optimum ZT [40]. Here we note that the product of μ and $(m/m_0)^{3/2}$ was commonly called weighted mobility. A large B usually corresponds to a high ZT value at a certain chemical potential. The advantage of the parameter B is that to obtain a good TE material, instead of checking all the interdependent transport properties, one should look for a semiconductor with a high weighted mobility and a low lattice thermal conductivity κ_l, which are less dependent on each other. Although E_b and B have been used to guide researches in thermoelectricity for many years, it is not possible to directly identify ZT_{opt} by using only these parameters. On the other hand, there have been a lot of efforts dedicated to optimize the PF, giving the optimum power factor $\mathrm{PF_{opt}}$ that can be obtained by changing the chemical potential [5]. Since ZT_{opt} generally occurs at a different chemical potential from $\mathrm{PF_{opt}}$, i.e., $ZT_{\mathrm{opt}} \neq \mathrm{PF_{opt}}\kappa^{-1}T$, one always needs to measure or estimate ZT_{opt} independently from $\mathrm{PF_{opt}}$ by checking again chemical potential dependence of ZT. Therefore, it should be useful for thermoelectric applications if we can calculate ZT_{opt}

from the information of $\mathrm{PF}_{\mathrm{opt}}$ or other simple parameters.

In this thesis, we propose that a new material parameter $\alpha = (\mathrm{PF}_{\mathrm{opt}}/\kappa_l)T$ can be defined to directly determine ZT_{opt} (Chapter 6). Although, ZT_{opt} and $\mathrm{PF}_{\mathrm{opt}}$ are generally optimized at *different* chemical potentials, the value of ZT_{opt} can be calculated using an analytical formula that involves the so-called Lambert W function, where α can be used as an input parameter. Without losing generality, the analytical formula for ZT_{opt} is derived within the one-band model and nondegenerate semiconductor approximation. We will show that ZT_{opt} for both bulk and low-dimensional semiconductors can be unified into a single universal curve, which allows us to predict and understand the materials of different dimensions that can have better ZT_{opt} by simply calculating the α parameter.

Chapter 2

Theoretical methods

In this chapter, first the transport properties will be discussed for the semiconductors, starting from the Boltzmann transport equation (BTE) in Section 2.1. Then the the Seebeck coefficient S, electrical conductivity σ, and electronic thermal conductivity κ_e are obtained from the BTE for electrons within framework one-band model of semiconductor in Section 2.1.1. Then we discuss the physical meaning of S, σ, and κ_e in Section 2.1.1.1. Similarly, the lattice thermal conductivity κ_ph will be given from the BTE for phonons. The results will be particularized to low-dimensional material for the case of thermoelectric power factor (Section 2.1.2).

2.1 Boltzmann transport formalism for carriers

The central concept in the Boltzmann approach is the existence of the distribution function $f(\mathbf{r}, \mathbf{k}, t)$, which is the probability of occupation of a carrier (electron or hole) at time t at $\mathbf{r}$ with the wavevector lying between $\mathbf{k}$. Under the condition equilibrium without external electric or magnetic field and thermal gradients, the distribution function is given by quantum-statistical physics as the Fermi-Dirac function for Fermions

$$f_0(E) = \frac{1}{1 + e^{\frac{E(\mathbf{k}) - \mu(\mathbf{r})}{k_\mathrm{B} T(\mathbf{r})}}}, \tag{2.1}$$

where $E(\mathbf{k})$ is the energy of the electron, $\mu(\mathbf{r})$ is the chemical potential, $T(\mathbf{r})$ is the absolute temperature as a function of position $\mathbf{r}$, and k_B is the Boltzmann constant. Here we assume that $\mu(\mathbf{r})$ and $T(\mathbf{r})$ are slowly changing with changing $\mathbf{r}$ so that local thermal equilibrium works. It is thus known that the transport properties of solids are given by the energy dispersion relations $E(\mathbf{k})$ near the Fermi energy.

For a given external perturbation such as an electric field or a thermal gradients, the carriers in a semiconductor move and change momentum in their trajectory $[\mathbf{r}(t),\ \mathbf{k}(t)]$. In Fig. 2.1, we show several trajectories in the phase space. Let us consider a carrier at the A$'$ and A positions on the trajectory 2 at time t and $t - \mathrm{d}t$, respectively. There

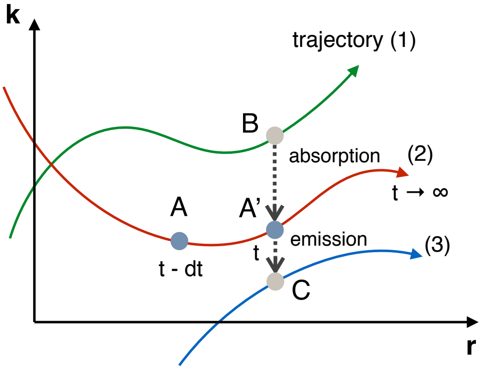

Figure 2.1 Illustration of trajectories in position-momentum space. Carriers move along a trajectory according to Newton's laws. Scattering changes the carrier's momentum, but does not affect its position.

are three possible processes under a carrier moving from A to A$'$: the diffusion, the effect of external forces and the collisions.

Let us take a fixed $\mathbf{k}$, one can say that the carriers in the small volume d$\mathbf{r}$ at the position $\mathbf{r}$ at the time t are those who were at the position $\mathbf{r}-\mathbf{v}\mathrm{d}t$ at the time $t-\mathrm{d}t$, where $\mathbf{v}=\mathrm{d}\mathbf{r}/\mathrm{d}t$ is the velocity of a carrier. The probability of occupation of a carrier at the time t is the same as the probability of occupation of a carrier at the time $t-\mathrm{d}t$. So $f(\mathbf{r},\mathbf{k},t)=f(\mathbf{r}-\mathbf{v}\mathrm{d}t,\mathbf{k},t-\mathrm{d}t)=f(\mathbf{r},\mathbf{k},t-\mathrm{d}t)-\mathbf{v}\frac{\partial f}{\partial \mathbf{r}}\mathrm{d}t$. We can write this as

$$\left.\frac{\partial f}{\partial t}\right|_{\text{diffusion}} = -\mathbf{v}\frac{\partial f}{\partial \mathbf{r}}. \tag{2.2}$$

Similarly for a given position $\mathbf{r}$, one can say that the carriers of wavevector $\mathbf{k}$ at the time t had the wavevector $\mathbf{k}-\frac{\partial \mathbf{k}}{\partial t}\mathrm{d}t$ at the time $t-\mathrm{d}t$. This gives that $f(\mathbf{r},\mathbf{k},t)=f(\mathbf{r},\mathbf{k}-\frac{\partial \mathbf{k}}{\partial t}\mathrm{d}t,t-\mathrm{d}t)=f(\mathbf{r},\mathbf{k},t-\mathrm{d}t)-\frac{\partial \mathbf{k}}{\partial t}\frac{\partial f}{\partial \mathbf{k}}\mathrm{d}t$. We can write this as

$$\left.\frac{\partial f}{\partial t}\right|_{\text{fields}} = -\frac{\partial \mathbf{k}}{\partial t}\frac{\partial f}{\partial \mathbf{k}}. \tag{2.3}$$

The remaining change of $f(\mathbf{r},\mathbf{k},t)$ as a function of the time t can be treated by $\left.\frac{\partial f}{\partial t}\right|_{\text{collisions}}$, in which a carrier is scattered by collision of the electron-phonon interaction or scattered by the defect.

Finally, we obtain the Boltzmann equation as

$$\begin{aligned}\frac{\partial f}{\partial t} &= \left.\frac{\partial f}{\partial t}\right|_{\text{diffusion}} + \left.\frac{\partial f}{\partial t}\right|_{\text{fields}} + \left.\frac{\partial f}{\partial t}\right|_{\text{collisions}} \\ &= -\mathbf{v}\frac{\partial f}{\partial \mathbf{r}} - \frac{\partial \mathbf{k}}{\partial t}\frac{\partial f}{\partial \mathbf{k}} + \left.\frac{\partial f}{\partial t}\right|_{\text{collisions}} .\end{aligned} \tag{2.4}$$

The Boltzmann equation is solved using the following two approximations:

Fig. 2.1: Fig/chapter2-fig1.pdf

1. The perturbation due to external fields and forces is assumed to be sufficiently small so that the distribution function can be linearized and written as

$$f = f_0 + f_1, \tag{2.5}$$

where $f_0(E)$ is the Fermi-Dirac equilibrium distribution function in Eq. (2.1), while $f_1(\mathbf{r}, \mathbf{k})$ is the perturbation term.

2. The collision term in the Boltzmann equation is written in the relaxation time approximation (RTA) so that the system returns to equilibrium experimentally

$$\left.\frac{\partial f}{\partial t}\right|_{\text{collisions}} = -\frac{f - f_0}{\tau} = -\frac{f_1}{\tau}, \tag{2.6}$$

where τ is the relaxation time and in general, τ is a function of wavevector $\mathbf{k}$, i.e., $\tau = \tau(\mathbf{k})$. The physical interpretation of τ is the time associated with the rate of returning to the equilibrium distribution when the external fields or thermal gradients are turned off. Here we consider a system when the fields are turned off at $t = 0$ (i.e. no diffusion and no effect of forces and fields), the Boltzmann equation in Eq. (2.4) becomes

$$\frac{\partial f}{\partial t} = \left.\frac{\partial f}{\partial t}\right|_{\text{collisions}} = -\frac{f - f_0}{\tau}, \tag{2.7}$$

which has solutions

$$f(t) = f_0 + \big(f(0) - f_0\big)e^{-t/\tau}, \tag{2.8}$$

where f_0 is the equilibrium distribution and $f(0)$ is the non-equilibrium distribution function at time $t = 0$. This result suggests that any perturbation in the system will decay exponentially by a characteristic time constant τ.

Using the approximations, the Boltzmann equation in Eq. (2.4) can be written as

$$\frac{\partial(f_0 + f_1)}{\partial t} = -\mathbf{v}\frac{\partial(f_0 + f_1)}{\partial \mathbf{r}} - \frac{\partial \mathbf{k}}{\partial t}\frac{\partial(f_0 + f_1)}{\partial \mathbf{k}} - \frac{f_1}{\tau}. \tag{2.9}$$

When the distribution function reaches a steady state and considered uniform systems so that there is no gradient of f_1 with respect to $\mathbf{r}$, $\mathbf{k}$, and t, ($\frac{\partial f_1}{\partial t} = \frac{\partial f_1}{\partial \mathbf{r}} = \frac{\partial f_1}{\partial \mathbf{k}} = 0$) then Eq. (2.9) can be rewritten as

$$\frac{f_1}{\tau} = -\mathbf{v}\frac{\partial f_0}{\partial \mathbf{r}} - \frac{\partial \mathbf{k}}{\partial t}\frac{\partial f_0}{\partial \mathbf{k}}. \tag{2.10}$$

As for the external force, let us consider the electric force $\mathcal{F} = \hbar \mathrm{d}\mathbf{k}/\mathrm{d}t = q\mathcal{E}$, where $q = \pm e$ is the unit charge of a carrier and $\mathcal{E}$ is the electric field. The the Boltzmann equation is obtained as

$$\frac{f_1}{\tau} = -\mathbf{v}\left(\frac{\partial \mu}{\partial \mathbf{r}}\frac{\partial f_0}{\partial \mu} + \frac{\partial T}{\partial \mathbf{r}}\frac{\partial f_0}{\partial T}\right) - \frac{q\mathcal{E}}{\hbar}\left(\frac{\partial E}{\partial \mathbf{k}}\frac{\partial f_0}{\partial E}\right), \tag{2.11}$$

where we adopt the assumption of $\mu(\mathbf{r})$ and $T(\mathbf{r})$ as discussed above. Substituting Eq.(2.1) and using the definition of the velocity $\mathbf{v} = 1/\hbar(\partial E/\partial \mathbf{k})$ into Eq. (2.11), we get

$$f_1 = \tau \mathbf{v} \frac{\partial f_0}{\partial E} \left(\nabla \mu + \frac{E-\mu}{T} \nabla T - q\mathcal{E} \right). \tag{2.12}$$

Eq. (2.12) is a solution of the Boltzmann equation in the presence of $\nabla\mu$, ∇T and $\mathcal{E}$ and it applies equally for holes and electrons in a semiconductor.

2.1.1 One-band model for semiconductors

Let us apply Eq. (2.12) for semiconductor that have one energy band. The number of charge carriers per unit volume in the range of energy from E to $E + \mathrm{d}E$ is given by $f_1\mathcal{D}(E)\mathrm{d}E$, where f_1 is the occupation probability of a carrier that given by Eq. (2.12), and $\mathcal{D}(E)$ is the density of state (DOS). Because the carriers with a charge $q = -e$ for the electron and $q = +e$ for the hole, move with a velocity v_α in the α direction ($\alpha = x, y, z$), the electric current density $\mathcal{J}$ is defined by

$$\mathcal{J} = \int q\mathbf{v} f_1 \mathcal{D}(E)\mathrm{d}E. \tag{2.13}$$

Further, since $E - \mu$ represents the total energy transported by a carrier, the flux of the energy $\mathcal{W}$ is defined by

$$\mathcal{W} = \int (E-\mu)\mathbf{v} f_1 \mathcal{D}(E)\mathrm{d}E. \tag{2.14}$$

By inserting Eq. (2.12) into Eqs. (2.13) and (2.14), we get, respectively,

$$\mathcal{J} = \int q\mathbf{v}\tau\mathbf{v} \frac{\partial f_0}{\partial E} \left(\nabla \mu + \frac{E-\mu}{T} \nabla T - q\mathcal{E} \right) \mathcal{D}(E)\mathrm{d}E, \tag{2.15}$$

and

$$\mathcal{W} = \int (E-\mu)\mathbf{v}\tau\mathbf{v} \frac{\partial f_0}{\partial E} \left(\nabla \mu + \frac{E-\mu}{T} \nabla T - q\mathcal{E} \right) \mathcal{D}(E)\mathrm{d}E. \tag{2.16}$$

From Eq. (2.15), we can obtain an expression for the electrical conductivity, by setting a zero temperature gradient $\nabla T = 0$ and a zero carrier concentration gradient $\nabla\mu = 0$, so that the electrical conductivity tensor σ is expressed by

$$\sigma = \frac{\mathcal{J}}{\mathcal{E}} = \int -q^2 \mathbf{v}\tau\mathbf{v} \frac{\partial f_0}{\partial E} \mathcal{D}(E)\mathrm{d}E. \tag{2.17}$$

When we use the definition of the electric field $\mathcal{E} = -\nabla\varphi(\mathbf{r})$ and the chemical potential $\mu(\mathbf{r}) = \Phi - q\varphi(\mathbf{r})$, where Φ is the electrochemical potential, and $\varphi(\mathbf{r})$ is the electrostatic potential energy, Eq. (2.15) can be rewritten as

$$\mathcal{J} = \int q\mathbf{v}\tau\mathbf{v} \frac{\partial f_0}{\partial E} \left(\nabla \Phi + \frac{E-\mu}{T} \nabla T \right) \mathcal{D}(E)\mathrm{d}E. \tag{2.18}$$

For obtaining the Seebeck coefficient, we now set a non-zero temperature gradient $\nabla T \neq 0$, when the circuit is open and no electric current flows (i.e. $\mathcal{J} = 0$ in Eq. (2.18)), then we obtain the tensor of the Seebeck coefficient from Eq. (2.18) as

$$S = -\frac{\nabla V}{\nabla T} = -\frac{1}{q}\frac{\nabla \Phi}{\nabla T} = \frac{1}{qT}\frac{\displaystyle\int q\mathbf{v}\tau\mathbf{v}\frac{\partial f_0}{\partial E}(E-\mu)\mathcal{D}(E)\mathrm{d}E}{\displaystyle\int q\mathbf{v}\tau\mathbf{v}\frac{\partial f_0}{\partial E}\mathcal{D}(E)\mathrm{d}E}. \tag{2.19}$$

On the other hand, the electronic thermal conductivity tensor κ_e can be obtained by setting no current flows (i.e. $\mathcal{J} = 0$). Using Eq. (2.16), we get

$$\kappa_\mathrm{e} = -\frac{\mathcal{W}}{\nabla T} = -\frac{1}{T}\left[\int \mathbf{v}\tau\mathbf{v}\frac{\partial f_0}{\partial E}(E-\mu)^2\mathcal{D}(E)\mathrm{d}E + \frac{\left(\displaystyle\int \mathbf{v}\tau\mathbf{v}\frac{\partial f_0}{\partial E}(E-\mu)\mathcal{D}(E)\mathrm{d}E\right)^2}{\displaystyle\int \mathbf{v}\tau\mathbf{v}\frac{\partial f_0}{\partial E}\mathcal{D}(E)\mathrm{d}E}\right]. \tag{2.20}$$

All of the integrations that appear in Eqs. (2.17), (2.19), and (2.20) have the similar form to one another. They may be expressed conveniently as

$$\mathcal{L}_i = \int \mathcal{T}(E)(E-\mu)^i\left(-\frac{\partial f_0}{\partial E}\right)\mathrm{d}E, \quad (i = 0, 1, 2), \tag{2.21}$$

where a tensor for the transport distribute function as a function of E $\mathcal{T}(E)$ is defined as

$$\mathcal{T}(E) = \mathbf{v}(E)\mathbf{v}(E)\tau(E)\mathcal{D}(E). \tag{2.22}$$

Thus, the transport coefficients σ, S, and κ_e within the one-band model can be written in terms of the transport integrals $\mathcal{L}_\alpha$ as

$$\sigma = q^2\mathcal{L}_0, \tag{2.23}$$

$$S = \frac{1}{qT}\frac{\mathcal{L}_1}{\mathcal{L}_0}, \tag{2.24}$$

$$\kappa_e = \frac{1}{T}\left(\mathcal{L}_2 - \frac{\mathcal{L}_1^2}{\mathcal{L}_0}\right). \tag{2.25}$$

2.1.1.1 A physical picture of transport coefficients

In this section, we wish to focus on the physics of Eqs. (2.23), (2.24), and (2.25). We saw that the three transport coefficients S, σ, and κ_e are expressed as the product of a quantized physical quantity and the convolution of two functions. Of the two

---

Fig. 2.2: Fig/chapter2-fig2.pdf

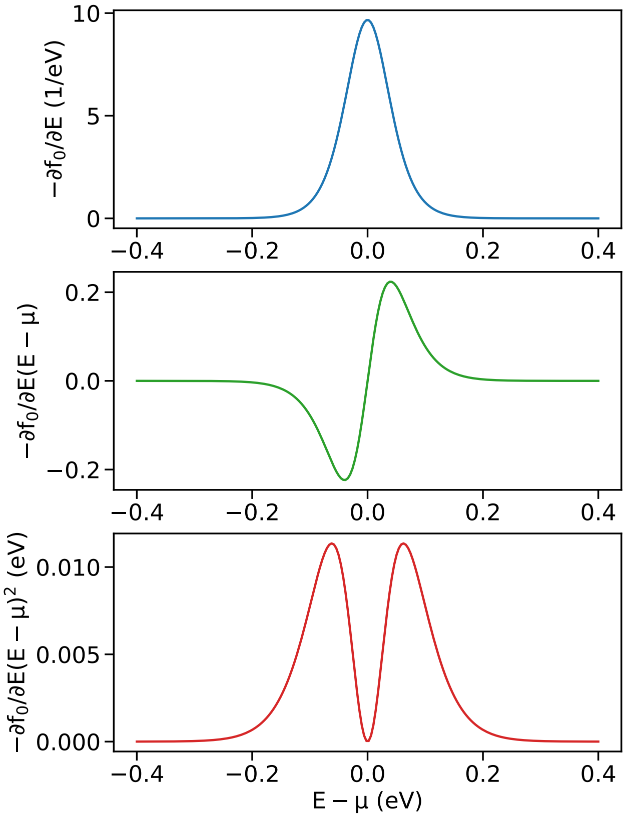

Figure 2.2 Function $\mathcal{I}_i = -\partial f_0/\partial E(E-\mu)^i$ of the integrals defining transport coefficients.

functions, one is the materials-specific transport distribution function $\mathcal{T}(E)$, and the other is a function, $\mathcal{I}_i$, defined as

$$\mathcal{I}_i = (E-\mu)^i \left(-\frac{\partial f_0}{\partial E}\right), \quad (i = 0, 1, 2). \tag{2.26}$$

The profiles of the three $\mathcal{I}_i$ functions are plotted in Fig. 2.2 as a function of $E-\mu$. This functions lead to selection of relevant carriers for different transport coefficients. In the case of charge conductivity [Eq. (2.23)], $\mathcal{I}_0$ probes carriers residing on the Fermi surface. In the case of entropy transport (that is both Seebeck coefficient [Eq. (2.24)] and electronic thermal conductivity [Eq. (2.25)]), the carriers which has slightly lower or slightly higher energy than the chemical potential contribute to S by $\mathcal{I}_1$ and κ_e by $\mathcal{I}_2$, respectively. These profiles also explain the reason why the electrical and thermal conductivities can only be positive, while the Seebeck coefficient can present either of the two signs since $\mathcal{I}_0 > 0$ and $\mathcal{I}_2 > 0$, but $\mathcal{I}_1$ can have both positive and negative values. From Eq. (2.21), it is noted that the sign of the transport coefficients is set by not only $\mathcal{I}_i$ but also $\mathcal{T}$ functions. However, in x direction, $\mathcal{T}$ can be expressed by $\mathcal{T} = v_x^2\tau\mathcal{D}$, which always has a positive value and does not depend on chemical potential. Therefore, the sign of the transport coefficients is only set by $\mathcal{I}_i$ function.

2.1.1.2 Transport coefficients of low-dimensional materials

The calculation of transport coefficients S, σ, and κ_e requires knowledge of the transport distribution function $\mathcal{T} = \mathbf{v}\mathbf{v}\tau\mathcal{D}$, which depends on the carrier group velocity $\mathbf{v}(E)$ of the energy band, the relaxation time $\tau(E)$, and the density of state $\mathcal{D}(E)$. For the sake of simplicity, we consider a single parabolic band, in which the energy band structure can be given as $E(\mathbf{k}) = \hbar^2\mathbf{k}^2/2m$, where $\mathbf{k}$ is wavevector of the carrier, m is the carrier effective mass, and $\hbar$ is the Planck constant. We assume that the material is isotropic with a dimension $d = 1, 2, 3$ for one-, two-, and three-dimensional materials, respectively. In such case, $\mathbf{v}(E)$, $\tau(E)$, and $\mathcal{D}(E)$ are given by

$$\mathbf{v}^2(E) = \frac{2E}{md}, \tag{2.27}$$

$$\tau(E) = \tau_0\left(\frac{E}{k_\mathrm{B}T}\right)^r, \tag{2.28}$$

$$\mathcal{D}(E) = \frac{1}{L^{3-d}2^{d-1}\pi^{d/2}\Gamma\left(\frac{d}{2}\right)}\left(\frac{2m}{\hbar^2}\right)^{d/2}E^{d/2-1}, \tag{2.29}$$

where r is a characteristic exponent for $\tau(E)$, τ_0 is the relaxation time constant, and L is the confinement length for a particular material dimension, $\Gamma(p) = \int_0^{+\infty} x^{p-1}e^{-x}\mathrm{d}x$ is the Gamma function.

Substituting Eqs. (2.27), (2.28), and (2.29) into Eq. (2.21) yields

$$\begin{aligned}\mathcal{L}_i = &\frac{-4\tau_0 m^{d/2-1}}{dL^{3-d}(2\pi)^{d/2}\hbar^d\Gamma(\frac{d}{2})(k_\mathrm{B}T)^r}\\ &\times\int\frac{\partial f_0}{\partial E}E^{r+d/2}\left[E^i - \left(\begin{array}{c} i \\ 1 \end{array}\right)E^{i-1}\mu + \left(\begin{array}{c} i \\ 2 \end{array}\right)E^{i-2}\mu^2 + \dots\right]\mathrm{d}E,\ (i = 0, 1, 2),\end{aligned} \tag{2.30}$$

where the symbol of $\left(\begin{array}{c} i \\ n \end{array}\right)$ is the number of combination,

$$\left(\begin{array}{c} i \\ n \end{array}\right) = \frac{i!}{n!(i-n)!} \quad \text{for} \quad 0 \le n \le i, \tag{2.31}$$

which is a specific positive integer known as a binomial coefficient. The integrals term in Eq. (2.30) can be simplified using the product rule for $j = 0, 1, 2$ as

$$\int\frac{\partial f_0}{\partial E}E^j\mathrm{d}E = f_0E^j\big|_0^\infty - j\int f_0E^{j-1}\mathrm{d}E = -j\int f_0E^{j-1}\mathrm{d}E. \tag{2.32}$$

Then defining the reduced band energy $\xi = E/k_\mathrm{B}T$ and the reduced chemical potential $\eta = \mu/k_\mathrm{B}T$, Eq. (2.32) is rewritten as

$$\int \frac{\partial f_0}{\partial E} E^j \mathrm{d}E = -j(k_\mathrm{B}T)^j \int f_0 \xi^{j-1} \mathrm{d}\xi = -j(k_\mathrm{B}T)^j F_{j-1}, \tag{2.33}$$

where

$$F_j = \int f_0 \xi^j \mathrm{d}\xi, \tag{2.34}$$

which is called the Fermi-Dirac integral [41]. Inserting Eq. (2.33) into Eq. (2.30), we get after some calculation

$$\begin{aligned}\mathcal{L}_i = \frac{-4\tau_0 m^{d/2-1}(k_\mathrm{B}T)^{d/2+i}}{dL^{3-d}(2\pi)^{d/2}\hbar^d\Gamma(\frac{d}{2})} \Bigg[& -(r + \frac{d}{2} + i)F_{r+d/2+i-1} \\ & + \eta \begin{pmatrix} i \\ 1 \end{pmatrix} (r + \frac{d}{2} + i - 1)F_{r+d/2+i-2} \\ & - \eta^2 \begin{pmatrix} i \\ 2 \end{pmatrix} (r + \frac{d}{2} + i - 2)F_{r+d/2+i-3} + \ldots \Bigg].\end{aligned} \tag{2.35}$$

Substituting Eq. (2.35) with $i = 0$ and 1 into Eqs. (2.23) and (2.24) we obtain the following formula for σ and S as

$$\sigma = q^2\mathcal{L}_0 = \frac{4q^2\tau_0 m^{d/2-1}(k_\mathrm{B}T)^{d/2}\left(r + \frac{d}{2}\right)}{dL^{3-d}(2\pi)^{d/2}\hbar^d\Gamma(\frac{d}{2})} F_{r+d/2-1}, \tag{2.36}$$

and

$$S = \frac{1}{qT}\frac{\mathcal{L}_1}{\mathcal{L}_0} = -\frac{k_\mathrm{B}}{q}\left(\eta - \frac{\frac{d}{2} + r + 1}{\frac{d}{2} + r} \times \frac{F_{d/2+r}}{F_{d/2+r-1}}\right). \tag{2.37}$$

2.1.2 Power factor of low-dimensional materials

Using Eqs. (2.36) and (2.36), let us give an analytical formula for the power factor PF. By changing η, we get the optimum PF value which can show the interplay between the quantum confinement length and the thermal de Broglie wavelength in low-dimensional semiconductors [20].

The thermal de Broglie wavelength, Λ, a measure of the thermodynamic uncertainty (see detail in Appendix A) for the localization of a particle (electron or hole in this case) of mass m, is defined by

$$\Lambda = \sqrt{\frac{2\pi\hbar^2}{k_\mathrm{B}Tm}}. \tag{2.38}$$

For a given $\tau(E)$, the carrier mobility is defined by

$$\mu_0 = \frac{q\langle\langle\tau(E)\rangle\rangle}{m}, \tag{2.39}$$

where

$$\langle\langle\tau(E)\rangle\rangle \equiv \frac{\langle E\tau(E)\rangle}{\langle E\rangle}, \tag{2.40}$$

where $\langle x\rangle = \int_0^\infty xe^{-E/k_\mathrm{B}T}\mathrm{d}E$ is a canonical average of x. Here, the quantity $\langle\langle\tau(E)\rangle\rangle$ is introduced to make an energy-dependent relaxation time. When we insert $\tau(E)$ in power law form as $\tau(E) = \tau_0[E(\mathbf{k})/k_\mathrm{B}T]^r$ in Eq. (2.40), we find

$$\langle\langle\tau(E)\rangle\rangle = \tau_0\frac{\int_0^\infty(\mathbf{k}^2/2mk_\mathrm{B}T)^r e^{-\mathbf{k}^2/2mk_\mathrm{B}T}\mathbf{k}^4\mathrm{d}\mathbf{k}}{\int_0^\infty e^{-\mathbf{k}^2/2mk_\mathrm{B}T}\mathbf{k}^4\mathrm{d}\mathbf{k}}. \tag{2.41}$$

With the substitution, $y = \mathbf{k}^2/2mk_\mathrm{B}T$,

$$\langle\langle\tau(E)\rangle\rangle = \tau_0\frac{\int_0^\infty y^{r+3/2}e^{-y}\mathrm{d}y}{\int_0^\infty y^{3/2}e^{-y}\mathrm{d}y}. \tag{2.42}$$

After recalling the definition of the Gamma function, $\Gamma(t) = \int_0^\infty x^{t-1}e^{-x}\mathrm{d}x$, we can rewrite Eq. (2.40) as

$$\langle\langle\tau(E)\rangle\rangle = \tau_0\frac{\Gamma\left(\frac{5}{2}+r\right)}{\Gamma\left(\frac{5}{2}\right)}. \tag{2.43}$$

From Eqs. (2.28), (2.39), and (2.43), the carrier relaxation time $\tau(E)$ can be rewritten as

$$\tau(E) = \frac{\mu_0 m\Gamma\left(\frac{5}{2}\right)}{q\Gamma\left(\frac{5}{2}+r\right)}\left(\frac{E}{k_\mathrm{B}T}\right)^2. \tag{2.44}$$

Substituting Eqs. (2.38) and (2.44) into Eq. (2.36) we obtain the following formula for the electrical conductivity as

$$\sigma = \frac{4q\mu_0}{L^3}\left(\frac{L}{\Lambda}\right)^d\frac{\left(r+\frac{d}{2}\right)\Gamma(\frac{5}{2})F_{r+d/2-1}}{d\Gamma(\frac{d}{2})\Gamma(\frac{5}{2}+r)}. \tag{2.45}$$

From Eqs. (2.37) and (2.45), the thermoelectric power factor can be written as

$$\mathrm{PF} = S^2\sigma = \frac{4k_\mathrm{B}^2\mu_0}{qL^3}\left(\frac{L}{\Lambda}\right)^d\left(\eta-\frac{\frac{d}{2}+r+1}{\frac{d}{2}+r}\frac{F_{d/2+r}}{F_{d/2+r-1}}\right)^2\frac{\left(r+\frac{d}{2}\right)\Gamma(\frac{5}{2})F_{r+d/2-1}}{d\Gamma(\frac{d}{2})\Gamma(\frac{5}{2}+r)}. \tag{2.46}$$

Equation (2.46) is an analytic expression for the power factor within the one-band model. However, it contains some Fermi-Dirac integrals F_j which can be solved by further approximations. In the following, we consider the two typical cases: (1) nondegenerate semiconductor and (2) degenerate semiconductor.

2.1.2.1 Nondegenerate semiconductors

The *nondegenerate semiconductors* correspond to the case where $\eta \ll 0$, i.e., the Fermi level lies within the band gap. In this case, the Fermi level lies within the band gap, we can thus use an approximation

$$\begin{aligned} F_j &= \int f_0 \xi^j \mathrm{d}\xi = \int \frac{1}{e^{\xi-\eta}+1}\xi^j \mathrm{d}\xi \\ &\approx \int \frac{1}{e^{\xi-\eta}}\xi^j \mathrm{d}\xi = e^{\eta}\int e^{-\xi}\xi^j \mathrm{d}\xi = e^{\eta}\Gamma(j+1), \end{aligned} \tag{2.47}$$

where $\Gamma(j) = \int e^{-\xi}\xi^j \mathrm{d}\xi$ is the Gamma function. Then Eqs. (2.45) and (2.37) become

$$\sigma = \frac{4q\mu_0}{L^3}\left(\frac{L}{\Lambda}\right)^d \frac{\left(r+\frac{d}{2}\right)\Gamma(\frac{5}{2})\Gamma(r+\frac{d}{2})}{d\Gamma(\frac{d}{2})\Gamma(\frac{5}{2}+r)} e^{\eta}, \tag{2.48}$$

and

$$S = -\frac{k_\mathrm{B}}{q}\left(\eta - \frac{\frac{d}{2}+r+1}{\frac{d}{2}+r} \times \frac{\Gamma(\frac{d}{2}+r+1)}{\Gamma(\frac{d}{2}+r)}\right). \tag{2.49}$$

Using the recursion formula for $\Gamma(x)$, $\Gamma(j+1) = j\Gamma(j)$, Eq. (2.49) can be simply written as

$$S = -\frac{k_\mathrm{B}}{q}\left(\eta - \frac{d}{2} - r - 1\right). \tag{2.50}$$

From Eqs. (2.48) and (2.50), the power factor for nondegenerate semiconductors can be written as

$$\mathrm{PF} = S^2\sigma = \frac{4k_\mathrm{B}^2\mu_0}{qL^3}\left(\frac{L}{\Lambda}\right)^d \left(\eta - \frac{d}{2} - r - 1\right)^2 \frac{\left(r+\frac{d}{2}\right)\mathrm{B}(r,\frac{5}{2})}{d\mathrm{B}(r,\frac{d}{2})} e^{\eta}, \tag{2.51}$$

where $\mathrm{B}(x,y) = \Lambda(x)\Lambda(y)/\Lambda(x+y)$ is the Beta function.

It is conventional to describe κ_e in terms of the Lorenz number L_e, which defined as $L_\mathrm{e} = \kappa_\mathrm{e}/\sigma T$. Then, from Eqs. (2.23), (2.25), (2.35) and (2.47),

$$L_\mathrm{e} = \frac{1}{(qT)^2}\left(\frac{\mathcal{L}_2}{\mathcal{L}_0} - \frac{\mathcal{L}_1^2}{\mathcal{L}_0^2}\right) = \left(\frac{k_\mathrm{B}}{q}\right)^2 \left(r + \frac{d}{2} + 2\right). \tag{2.52}$$

It is noted that L_e is independent of the Fermi energy, but depends on the exponent r and the dimension d in Eq. (2.50) for the nondegenerate semiconductors.

2.1.2.2 Degenerate semiconductors

Now we turn to the *degenerate semiconductors* when $\eta \gg 0$. This means that the Fermi level lies above the conduction-band bottom for electrons or below the valence-band top for holes. In this case, the conductor is metallic. Thus, the Fermi-Dirac integral can be expressed in the form of a rapidly converging series

$$\begin{aligned} F_j &= \int f_0\xi^j \mathrm{d}\xi = -\frac{1}{j+1}\int \frac{\partial f_0}{\partial \xi}\xi^{j+1}\mathrm{d}\xi \\ &= -\frac{1}{j+1}\int \frac{\partial f_0}{\partial \xi}\left[\eta^{j+1} + \begin{pmatrix} j \\ 1 \end{pmatrix}\eta^j(\xi-\eta) + \begin{pmatrix} j \\ 2 \end{pmatrix}\eta^{j-1}(\xi-\eta)^2 + \ldots\right]\mathrm{d}\xi \\ &= \frac{\eta^{j+1}}{j+1} + j\eta^{j-1}\frac{\pi^2}{6} + j(j-1)(j-2)\eta^{j-3}\frac{7\pi^4}{360} + \ldots. \end{aligned} \tag{2.53}$$

The electrical conductivity of the degenerate semiconductor is found by inserting only the first term in Eq. (2.53) into Eq. (2.45),

$$\sigma = \frac{4q\mu_0}{L^3}\left(\frac{L}{\Lambda}\right)^d \frac{\Gamma(\frac{5}{2})}{d\Gamma(\frac{d}{2})\Gamma(\frac{5}{2}+r)}\eta^{r+\frac{d}{2}}, \tag{2.54}$$

On the other hand, if only the first term in Eq. (2.53) is used, the Seebeck coefficient in Eq. (2.37) would be zero, which is consistent with the fact that most metals have negligibly small values of the Seebeck coefficient. To obtain a nonzero value for the the Seebeck coefficient, the first two terms of Eq. (2.53) are used. Then we obtain

$$S = \frac{k_{\mathrm{B}}}{q}\frac{\pi^2}{3}\frac{\left(r+\frac{d}{2}\right)}{\eta}. \tag{2.55}$$

From Eqs. (2.54) and (2.55), the power factor for nondegenerate semiconductors can be written as

$$\mathrm{PF} = S^2\sigma = \frac{4\pi^4 k_{\mathrm{B}}^2\mu_0}{9qL^3}\left(\frac{L}{\Lambda}\right)^d \frac{\left(r+\frac{d}{2}\right)^2\Gamma(\frac{5}{2})}{d\Gamma(\frac{d}{2})\Gamma(\frac{5}{2}+r)}\eta^{r+\frac{d}{2}-2}. \tag{2.56}$$

The first two terms in Eq. (2.53) are also needed to obtain the Lorenz number, which is given by

$$L = \frac{\pi^2}{3}\left(\frac{k_{\mathrm{B}}}{q}\right)^2 = 2.44\times 10^{-8}\ \mathrm{W\Omega K^{-2}}. \tag{2.57}$$

This shows that the Lorenz number is constant for degenerate semiconductor (or metal) and, in particular, it should not depend on the scattering mechanisms or the dimensional materials. These features is called by the Wiedemann-Franz-Lorenz law which states that the ratio of the electronic contribution of the thermal conductivity to electrical conductivity of a metal is proportional only to the absolute temperature, and does not depend on materials.

In Fig. 2.3, we compare the PF of 3D system as a function of the dimensionless chemical potential η for three different cases, in which the PF for the exact, nondegenerate, and degenerate semiconductor cases are obtained from Eqs. (2.46), (2.51), and (2.56), respectively. For the exact case, we can determine the optimum PF from Eq. (2.46) by calculating the Fermi-Dirac integral in Eq. (2.46) *numerically.* The optimum PF is found at $\eta > 0$, i.e., the Fermi energy exists in the valence or conduction bands. For the nondegenerate semiconductor case, we can determine the optimum PF from Eq. (2.51) by solving $\mathrm{d(PF)/d}(\eta) = 0$ *analytically.* The optimum PF is found at $\eta = 0$, i.e., the Fermi energy touches the top (bottom) of the valence (conduction) energy band in a p-type (n-type) semiconductor, while the optimum PF does not appear for degenerate semiconductor case [see Eq. (2.56)]. As shown in Fig 2.3, the optimum PF value of the nondegenerate case is similar to that of the exact case. Therefore, Eq. (2.51) can be used directly to evaluate the optimum PF value, which will be discussed in Chapter 3.

Fig. 2.3: Fig/chapter2-fig4.pdf

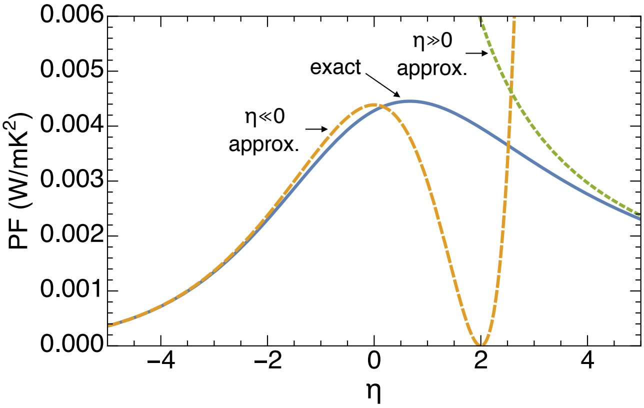

Figure 2.3 Power factor PF as functions of the dimensionless chemical potential η in the 3D system ($d = 3$). Theoretical results for the PF and their nondegenerate ($\eta \ll 0$) and degenerate ($\eta \gg 0$) approximations are represented by solid, dashed, and dotted lines, respectively. The thermal de Broglie wavelength is set to be $\Lambda = 4.5$ nm (for n-type Si) and the mobility $\mu_0 = 420$ cm^2/Vs.

2.1.3 Electron scattering

Now let us discuss the scattering of carrier. The thermoelectric properties of materials depend on the availability of carriers and on their scattering rates. In the previous sections 2.1.1 and 2.1.2, we focused on the carriers and their generation using the time-dependent scattering. In this section, we will derive and explain the key ideas behind a time-dependent formulation of quantum scattering theory.

2.1.3.1 Defining scattering coefficient from the Fermi golden rule

The Fermi golden rule gives the scattering rate of transitions for a given the perturbation potential V between discrete states $|\mathbf{k}\rangle$ and $|\mathbf{k}'\rangle$ as follows [41]

$$\frac{1}{\tau(\mathbf{k} \to \mathbf{k}')} \approx \frac{2\pi}{\hbar} |\langle \mathbf{k}'|V|\mathbf{k}\rangle|^2 \delta[E(\mathbf{k}) - E(\mathbf{k}')], \tag{2.58}$$

where $\hbar$ is the Planck constant, δ is the Dirac-delta function, and E is the energy dispersion. The general scattering rate is given by the product of a constant $2\pi/\hbar$, the square of transition matrix element and a Dirac-delta function. For the one-band model, the scattering rate is calculated between the states within the parabolic energy band (intraband scattering), where a *continuum* of states exists. In this case, the final scattering rate will be obtained by summation over all relevant unoccupied $\mathbf{k}'$ states,

$$\frac{1}{\tau(\mathbf{k})} = \sum_{\mathbf{k}'} \frac{1}{\tau(\mathbf{k} \to \mathbf{k}')} = \frac{2\pi}{\hbar} \sum_{\mathbf{k}'} |\langle \mathbf{k}'|V|\mathbf{k}\rangle|^2 \delta[E(\mathbf{k}) - E(\mathbf{k}')]. \tag{2.59}$$

As an example, let us consider the scattering rate between the electron states in the conduction band by a point scatterer in a 3D semiconductor, in which a perturbing potential is given by $V(\mathbf{r}) = V_0\delta(\mathbf{r})$ for short-range interactions, where the unit of the constant V_0 is Jm^3. The matrix element between electronic states $|\mathbf{k}\rangle$ and $|\mathbf{k}'\rangle$ can be obtained as [41]

$$|\langle\mathbf{k}'|V_0\delta(\mathbf{r})|\mathbf{k}\rangle| = \int \mathrm{d}^3\mathbf{r} \left(\frac{e^{-i\mathbf{k}'\cdot\mathbf{r}}}{\sqrt{\Omega}}\right) V_0\delta(\mathbf{r}) \left(\frac{e^{+i\mathbf{k}'\cdot\mathbf{r}}}{\sqrt{\Omega}}\right) = \frac{V_0}{\Omega}, \tag{2.60}$$

where Ω is the volume of the system. After substituting the matrix element of Eq. (2.60) into Eq. (2.59), the scattering rate can be written as

$$\frac{1}{\tau(\mathbf{k})} = \frac{2\pi}{\hbar}\left(\frac{V_0}{\Omega}\right)^2 \sum_{\mathbf{k}'} \delta[E(\mathbf{k}) - E(\mathbf{k}')]. \tag{2.61}$$

By using the carrier density of states (DOS), defined as

$$\mathcal{D}(E) = \frac{2}{\Omega}\sum_{\mathbf{k}} \delta[E - E(\mathbf{k})] \tag{2.62}$$

in units of $\mathrm{J}^{-1}\mathrm{m}^{-3}$, where the factor 2 accounts for the spin degeneracy, Eq. (2.61) is expressed as

$$\frac{1}{\tau(E)} = \frac{\pi V_0^2}{\hbar\Omega}\mathcal{D}(E). \tag{2.63}$$

This example shows an important result indicating that the scattering rate for the continuum of states is, in general, proportional to the DOS, while the strength of scattering increases with the square of the scattering potential. The carrier relaxation time $\tau(E)$ is thus inversely proportional to the carrier DOS:

$$\tau(E) = C\mathcal{D}^{-1}(E), \tag{2.64}$$

where $C = \hbar\Omega/(\pi V_0^2)$ is the scattering coefficient in units of $\mathrm{W}^{-1}\mathrm{m}^{-3}$. Note that according to the Fermi golden rule, the coefficient C can be a constant value when the matrix element is approximately constant.

2.1.3.2 Calculating scattering coefficient from experimental data

Here we derive a formula of the coefficient C in Eq. (2.64) considering a parabolic band for any semiconductor so that C can be calculated from experimental data. From Eqs. (2.28), (2.39), and (2.43), the carrier relaxation time $\tau(E)$ can be rewritten as

$$\tau(E) = \frac{\mu_0 m\Gamma\left(\frac{5}{2}\right)}{q\Gamma\left(\frac{5}{2}+r\right)}\left(\frac{E}{k_\mathrm{B}T}\right)^r. \tag{2.65}$$

We assume that the acoustic phonon scattering is the main carrier scattering mechanism at the room temperature, i.e., $\tau(E) \propto \mathcal{D}(E)^{-1}$ [41]. From Eqs. (2.29), (2.65) and $\tau(E) \propto \mathcal{D}(E)^{-1}$, we obtain $r = 1 - d/2$ for the system with the dimension d. By using $r = 1 - d/2$, from Eqs. (2.64), (2.29), and (2.65), the coefficient C can be written as

$$C = \tau(E)\mathcal{D}(E) = \frac{2\mu_0 m \Gamma\left(\frac{5}{2}\right)}{q k_{\mathrm{B}} T L^{3-d} \Gamma\left(\frac{7-d}{2}\right)\Gamma\left(\frac{d}{2}\right)} \left(\frac{m k_{\mathrm{B}} T}{2\pi\hbar^2}\right)^{d/2}. \tag{2.66}$$

After substituting the thermal de Broglie wavelength $\Lambda = (2\pi\hbar^2/m k_{\mathrm{B}} T)^{1/2}$ into Eq. (2.66), the coefficient C is given by

$$C = \frac{2\mu_0 m}{q k_{\mathrm{B}} T L^3} \left(\frac{L}{\Lambda}\right)^d \frac{\Gamma\left(\frac{5}{2}\right)}{\Gamma\left(\frac{7-d}{2}\right)\Gamma\left(\frac{d}{2}\right)}. \tag{2.67}$$

Equation (2.67) is useful to calculate the coefficient C from μ_0 and m, which can be obtained from experimental data. For example, in the 3D ($d = 3$) n-type $\mathrm{Bi_2Te_{2.7}Se_{0.3}}$ [42], at room temperature ($T = 298$ K) and doping concentration on the order of 10^{19} $\mathrm{cm^{-3}}$, the carrier mobility and the carrier effective mass are $\mu = 173$ $\mathrm{cm^2/Vs}$ and $m = 1.12 m_0$, respectively, where m_0 is the free electron mass. From Eq. (2.67), we obtain the C value of about 1.18×10^{33} $\mathrm{W^{-1}m^{-3}}$ and correspondingly the average relaxation time is about 0.1 ps.

2.1.4 Two-band model of semiconductor

Next we consider the two-band model of semiconductor. In 1D nanowire with large width or 2D layer with large thickness, there are many energy subbands that need to be taken into consideration due to the degeneracy of the multiple carrier pockets at the conduction band and valence band extrema for a given energy. For a low-dimensional system, besides the degeneracy effect, quantum confinement also introduces subband splitting, and results in a set of subbands that is given by zone-folding of a single band of the bulk materials. In such a case, the one-band model does not work well to describe the thermoelectricity of the low-dimensional systems. Therefore, contributions from all of the subbands with band extrema that fall within a few $k_{\mathrm{B}}T$ window around the Fermi energy need to be included for the calculation of S, σ, and κ_e. For a multi-band system, Eqs. (2.23)-(2.25) needs to be replaced by sum $\mathcal{L}_{i,\mathrm{total}} = \sum_b \mathcal{L}_i^b$ with $i = 0, 1, 2$ of contributions from each subband b, and the quantities of transports coefficients, we

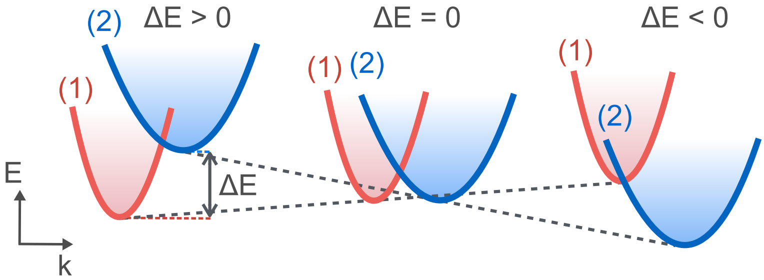

Figure 2.4 Schematics of convergence of multivalley bands in the case of two conduction valleys.

finally get

$$\sigma_{\text{total}} = \sum_b \mathcal{L}_0^b, \tag{2.68}$$

$$S_{\text{total}} = \frac{1}{qT} \frac{\sum\limits_b \mathcal{L}_1^b}{\sum\limits_b \mathcal{L}_0^b}, \tag{2.69}$$

$$\kappa_{e,\text{total}} = \frac{1}{q^2 T} \left(\sum_b \mathcal{L}_2^b - \frac{\left(\sum\limits_b \mathcal{L}_1^b \right)^2}{\sum\limits_b \mathcal{L}_0^b} \right). \tag{2.70}$$

An important example is to find the optimum power factor values of in which there are significant contributions from two energy bands. For that purpose, let us consider the *two-band model* to find the optimum power factor. We consider two conduction valleys (1) and (2) at different energies E_1 and E_2, respectively, as shown in Fig. 2.4. In the converged condition, the valley splitting energy $\Delta E = E_2 - E_1$, which is the energy difference between the two valleys, is going to be zero by changing some parameters [see the middle panel of Fig. 2.4].

Electrical conductivity of a two-band semiconductor is defined by [Eq. (2.68)]

$$\sigma = \sigma_1 + \sigma_2, \tag{2.71}$$

where $\sigma_{1,2}$ for the valleys (1) and (2) are expressed as [Eq. (2.48)]

$$\sigma_{1,2} = \frac{4q^2 \tau_{1,2} \left(r + \frac{d}{2}\right) (k_{\text{B}}T)^{d/2} \Gamma(\frac{d}{2} + r)}{d \; L^{3-d} (2\pi)^{d/2} \hbar^d \Gamma(\frac{d}{2})} m_{1,2}^{d/2-1} e^{\eta_{1,2}}, \tag{2.72}$$

where m_b and η_b $(b = 1, 2)$ are the effective mass and the reduced chemical potential of the valleys (b), respectively. We adopt the energy dependent relaxation time approximation for both valleys (1) and (2), i.e. $\tau(E) = \tau_{1,2}(E/k_{\text{B}}T)^{r_{1,2}}$, where $\tau_{1,2}$ and

---

Fig. 2.4: Fig/chapter2-fig5.pdf

$r_{1,2}$ are the relaxation time coefficients and the characteristic exponent determining the scattering mechanism of the valleys $b = 1, 2$, respectively. Assuming that the valleys (1) and (2) have the same scattering mechanism, we can adopt $r_1 = r_2 = r$ in Eq. (2.72).

By substituting Eq. (2.72) into Eq. (2.72), we obtain

$$\sigma = \frac{4q^2\left(r + \frac{d}{2}\right)(k_{\mathrm{B}}T)^{d/2}\Gamma(\frac{d}{2} + r)}{d\ L^{3-d}(2\pi)^{d/2}\hbar^d\Gamma(\frac{d}{2})}\left[\tau_1 m_1^{d/2-1} + \frac{\tau_2 m_2^{d/2-1}}{e^{\Delta E/k_BT}}\right]e^{-\eta}. \tag{2.73}$$

The Seebeck coefficient of the two-band semiconductors is defined by [5]

$$S = \frac{\sigma_1 S_1 + \sigma_2 S_2}{\sigma_1 + \sigma_2}, \tag{2.74}$$

where $S_{1,2}$ for the valleys $b = 1, 2$ are expressed as [Eq. (2.50)]

$$S_b = -\frac{k_B}{q}\left(\eta_b - \frac{d}{2} - r - 1\right), \quad (b = 1, 2), \tag{2.75}$$

Substituting Eqs. (2.72) and (2.75) into Eq. (2.74), and after doing some algebra, we can obtain

$$S = -\frac{k_B}{q}\frac{\left(\eta_1 - \frac{d}{2} - r - 1\right)\frac{\sigma_1}{\sigma_2} + \left(\eta_2 - \frac{d}{2} - r - 1\right)}{\frac{\sigma_1}{\sigma_2} + 1}. \tag{2.76}$$

where $\sigma_1/\sigma_2 = (\tau_1/\tau_2)(m_1/m_2)^{d/2-1}e^{\eta_1-\eta_2} = Ae^{\eta_1-\eta_2}$, with $A = (\tau_1/\tau_2)(m_1/m_2)^{d/2-1}$. Here we set $\eta_1 - \eta_2 = \Delta E/k_{\mathrm{B}}T$, and $\eta_1 = -\eta$. The Seebeck coefficient of nondegenerate semiconductors within the two-band model can be written in terms of η_1, $\Delta E/k_{\mathrm{B}}T$, r, d, and A as

$$S = \frac{k_{\mathrm{B}}}{q}\left(\eta + \frac{d}{2} + r + 1 + \frac{\Delta E/k_{\mathrm{B}}T}{Ae^{\Delta E/k_{\mathrm{B}}T} + 1}\right). \tag{2.77}$$

2.1.4.1 Two-band model for two-dimensional materials

For two-dimensional (2D) semiconductors, we set $d = 2$, so that S and σ are rewritten as

$$S = \frac{k_{\mathrm{B}}}{q}\left[\eta + r + 2 + \frac{\Delta E/k_{\mathrm{B}}T}{(\tau_1/\tau_2)e^{\Delta E/k_{\mathrm{B}}T} + 1}\right], \tag{2.78}$$

and

$$\sigma = \frac{q^2 k_{\mathrm{B}}T\Gamma(r + 2)}{L\pi\hbar^2}\left(\tau_1 + \frac{\tau_2}{e^{\Delta E/k_{\mathrm{B}}T}}\right)e^{-\eta}. \tag{2.79}$$

From Eqs. (2.78) and (2.79), the thermoelectric power factor can be written as

$$\mathrm{PF}^{2D} \equiv S^2\sigma = A(\eta + B)^2 e^{-\eta}, \tag{2.80}$$

where A (in units of W/mK^2) and B (dimensionless) are given by

$$A = \frac{k_{\mathrm{B}}^3 T\Gamma(r + 2)}{L\pi\hbar^2}\left(\tau_1 + \frac{\tau_2}{e^{\Delta E/k_{\mathrm{B}}T}}\right), \tag{2.81}$$

and

$$B = r + 2 + \frac{\Delta E/k_{\mathrm{B}}T}{(\tau_1/\tau_2)e^{\Delta E/k_{\mathrm{B}}T} + 1}, \tag{2.82}$$

respectively.

We can now determine the optimum power factor as a function of η from Eq. (2.80) by solving $\mathrm{d}(\mathrm{PF})/\mathrm{d}\eta = 0$. The optimum power factor, $\mathrm{PF}_{\mathrm{opt}}^{\mathrm{2D}}$, of the 2D semiconductor is analytically given by

$$\mathrm{PF}_{\mathrm{opt}}^{\mathrm{2D}} = \frac{4k_B^3 T\Gamma(r+2)}{L\pi\hbar^2}\left(\tau_1 + \frac{\tau_2}{e^{\Delta E/k_{\mathrm{B}}T}}\right) e^{\left(r + \frac{\Delta E/k_{\mathrm{B}}T}{(\tau_1/\tau_2)e^{\Delta E/k_{\mathrm{B}}T} + 1}\right)} \tag{2.83}$$

whereas the corresponding value for the reduced (dimensionless) chemical potential is $\eta_{\mathrm{opt}}^{\mathrm{2D}} = 2 - B$. We will discuss about multi-valley bands convergence using Eq.(2.83) in Chapters 4 and 5 in this thesis.

2.2 Phonon transport properties

Finally we briefly mention lattice thermal conductivity. Thermal conductivity in dielectric materials and most semiconductors is dominated by phonons. The purpose of this section is to describe how phonons carry heat through the material, i.e. to evaluate the lattice thermal conductivity κ_l. At high temperatures, the main factor limiting κ_l is the phonon-phonon scattering. However, at low temperature, the size effects are extremely important, even in macroscopic samples, because the phonon mean free path can be longer than the sample size [43]. Therefore, the ultimate scattering mechanism of κ_l at low temperatures is the boundary scattering [43]. The reduction of κ_l is very important for thermoelectricity since it can enhance $ZT = \mathrm{PF}/(\kappa_e + \kappa_l)$. Thus adopting the low-dimensional material is an efficient way to reduce κ_l due to the size effects. For example, the thermoelectric measurement for Si nanowires have observed that κ_l can be reduced below the theoretical limit of bulk Si (0.99 W/mK) because the phonon mean free path is limited by boundary scattering in nanostructures [3, 4]. This phenomenon can be understood by using the models for κ_l of semiconductors, which were developed by Callaway [44], Holland [45], and Guyer [46]. In these models, they observed that κ_l starts to decrease showing a T^3 behavior when temperature below $10 - 20$ K. Therefore, κ_l behaves in temperature like the specific heat since the scattering of the phonons by the boundaries is a constant. Such models are useful to understand the lattice thermal conductivity.

2.2.1 Boltzmann transport formalism for phonons

As discussion in Section 2.1, the Boltzmann equation describes the changes in the distribution function due to the drift to the changes in the distribution function due to scattering processes. The general form of this equation in the stationary state is, as in the case of electrons (see Section 2.1),

$$\frac{\partial n}{\partial t} = \left.\frac{\partial n}{\partial t}\right|_{\text{diffusion}} + \left.\frac{\partial n}{\partial t}\right|_{\text{collisions}}, \tag{2.84}$$

where n is the phonon distribution function. We note that, in the case of electrons, the equilibrium distribution function is Fermi-Dirac distribution function f. In the case of phonons, the equilibrium distribution function corresponds to a Bose-Einstein distribution function, which is given as

$$n_{0,\nu}(\mathbf{q}) = \frac{1}{e^{\frac{\hbar\omega_\nu}{k_\mathrm{B}T}} - 1}, \tag{2.85}$$

where ν is the phonon mode, ω is the phonon frequency, and $\mathbf{q}$ is the phonon wavevector. Different from the case of electrons that a term of external forces appears [see Eq. (2.3)], phonons do not experience any external forces. Therefore, only spacial variations of the distribution function must be taken into account, Eq. (2.85) can be written as

$$\frac{\partial n}{\partial t} = \mathbf{v}_{\nu\mathbf{q}}\frac{\partial n}{\partial \mathbf{r}} + \left.\frac{\partial n}{\partial t}\right|_{\text{collisions}}, \tag{2.86}$$

where $\mathbf{v}_{\nu\mathbf{q}} = \partial\omega_\nu/\partial\mathbf{q}$ is the phonon group velocity. The scattering integral depends on scattering processes due to electrons, impurities, boundaries, and other phonons. In the local equilibrium approaches, the collision term (or scattering term) in the Boltzmann equation is written within the relaxation time approximation, which is similar to the case of electron. The rate of change of the distribution function n depends on the difference of the distribution out of equilibrium with that of equilibrium n_0. In terms of the relaxation time $\tau_{\nu\mathbf{q}}$, Eq. (2.86) can be written as

$$\frac{\partial n}{\partial t} = \mathbf{v}_{\nu\mathbf{q}}\frac{\partial n}{\partial \mathbf{r}} + \frac{n - n_0}{\tau_{\nu\mathbf{q}}}. \tag{2.87}$$

Eq. (2.87) suggests that the distribution function decays exponentially to n_0 in a time decay $\tau_{\nu\mathbf{q}}$, which is similar to the case of electrons (see Eq. (2.8)). This approximation allows us to obtain a solution for κ_l in terms of an integral expression depending on the relaxation time. Since the distribution function can be linearized as $n = n_0 + n_1$, where $n_1(\mathbf{r}, \mathbf{q})$ is the perturbation term. Eq. (2.87) can be rewritten in term of n_1 as

$$\frac{\partial(n_1 + n_0)}{\partial t} = \mathbf{v}_{\nu\mathbf{q}}\frac{\partial(n_1 + n_0)}{\partial \mathbf{r}} + \frac{n_1}{\tau_{\nu\mathbf{q}}}. \tag{2.88}$$

When the distribution function reaches a steady state and considered uniform systems so that there is no gradient of n_1 with respect to $\mathbf{r}$ and t, then Eq. (2.88) can be rewritten as

$$\frac{n_1}{\tau_{\nu\mathbf{q}}} = -\mathbf{v}_{\nu\mathbf{q}}\frac{\partial n_0}{\partial \mathbf{r}} = -\mathbf{v}_{\nu\mathbf{q}}\frac{\partial n_0}{\partial T}\frac{\partial T}{\partial \mathbf{r}}. \tag{2.89}$$

The lattice thermal conductivity κ_l can be obtained from Eq. (2.89) by using the definition of the thermal current density (or heat flux), $\mathcal{J}_Q$, that is the integral over the phonon population of the energy times the group velocity:

$$\mathcal{J}_Q = \frac{1}{N_{\mathbf{q}}\Omega} \sum_{\nu\mathbf{q}} \hbar\omega_\nu n_1 \mathbf{v}_{\nu\mathbf{q}}, \tag{2.90}$$

where Ω is the volume, and $N_{\mathbf{q}}$ is the number of $\mathbf{q}$ points. According to the Fourier law, the heat flux resulting from thermal conduction is proportional to the magnitude of the temperature gradient ∇T and opposite to it in sign, that means

$$\mathcal{J}_Q = -\kappa_l \nabla T. \tag{2.91}$$

Substituting Eqs. (2.89) and (2.91) to Eq. (2.90), we obtain the following formula for the lattice thermal conductivity as

$$\kappa_l = -\frac{1}{N_{\mathbf{q}}\Omega} \sum_{\nu\mathbf{q}} \hbar\omega_\nu \tau_{\nu\mathbf{q}} \mathbf{v}_{\nu\mathbf{q}} \mathbf{v}_{\nu\mathbf{q}} \frac{\partial n_0}{\partial T}. \tag{2.92}$$

In general, κ_l is a second rank tensor and the direction of κ_l does not necessarily coincide with the thermal gradient. However, when $\tau_{\nu\mathbf{q}}$ and $\mathbf{v}_{\nu\mathbf{q}}$ are isotropic, we can transform Eq. (2.92) into an integration as

$$\kappa_l = \int_0^{\omega_{\max}} \tau \mathbf{v}\mathbf{v} C_\omega \mathrm{d}\omega, \tag{2.93}$$

where $\omega_{\max}$ represents the highest phonon frequency, such as the Debye frequency in the Debye model, and $C_\omega = \hbar\omega\mathcal{D}(\omega)(-\partial n_0/\partial T)$ is the specific heat per unit frequency at frequency ω and temperature T, where $\mathcal{D}(\omega) = \sum_{\nu\mathbf{q}} \delta(\omega - \omega_{\nu\mathbf{q}})$ is the phonon density of state. The phonon mode ν and wavevector $\mathbf{q}$ indexes have been omitted in Eq. (2.93) for clarity. In particular, for x direction, the phonon group velocity can explained as $v_x^2 = v^2/d$, where $d = 1, 2, 3$ denotes the dimension of the material (1D, 2D, or 3D systems). Eq. (2.93) can be rewritten as

$$\kappa_l = \frac{1}{d} \int_0^{\omega_{\max}} \tau v_x^2 C_\omega \mathrm{d}\omega. \tag{2.94}$$

In the case that both τ and v_x are independent of frequency, Eq. (2.94) can be rewritten as

$$\kappa_l = \frac{1}{d} C v_x L_{\mathrm{mfp}}, \tag{2.95}$$

where $L_{\mathrm{mfp}} = \tau v_x$ is the phonon mean free path.

2.2.2 Phonon scattering

Whereas electron scattering is important in electronic transport properties as discussed in Section 2.1.3, phonon scattering is important in thermal transport, particularly for the case of insulators and semiconductors where heat is carried mainly

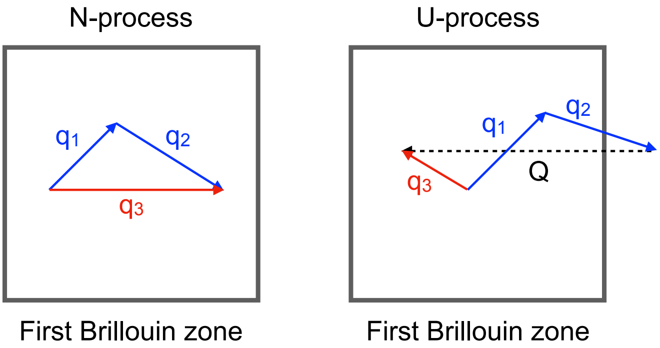

Figure 2.5 Phonon-phonon normal (N-process) and Umklapp processes (U-process) in a plane square lattice. In an N-process case, the wave number $\mathbf{q}_1+\mathbf{q}_2=\mathbf{q}_3$ is conserved, while in a U-process case, any additional vector of the reciprocal space is added in the conservation law as $\mathbf{q}_1+\mathbf{q}_2=\mathbf{q}_3+\mathbf{Q}$.

by phonons. The scattering mechanisms for phonons are phonon-phonon scattering, phonon-boundary scattering, defect-phonon scattering, and phonon-electron scattering. However, the dominant phonon scattering process in crystalline materials at high temperature is usually phonon-phonon scattering (also known as phonon anharmonicity). Phonons are scattered by other phonons because of anharmonic terms in the restoring potential. This scattering process permits:

1. Two phonons to combine to form a third phonon.
2. One phonons to break up into two phonons.

In these anharmonic processes, the quasi-momentum conservation law is:

$$\mathbf{q}_1+\mathbf{q}_2=\mathbf{q}_3+\mathbf{Q}, \tag{2.96}$$

where $\mathbf{Q}$ is any reciprocal lattice vector. If $\mathbf{Q}=0$, the process is called normal process (N-process), while in the general case, $\mathbf{Q}\neq 0$, and the process is called Umklapp process (U-process). In Fig. 2.5, we show the quasi-momentum conservation law for both N- and U-processes. U-process is important when $\mathbf{q}_1$ or $\mathbf{q}_2$ are large, i.e. comparable to a reciprocal lattice vector (see Fig. 2.5). When U-process is present in system, the scattered phonon wavevector $\mathbf{q}_3$ can be in a direction opposite to the energy flow, thereby giving rise to *thermal resistance*. At high temperature, U-process dominate the lattice thermal conductivity because the high momentum transfer and large phonon energies that are involved.

The phonon density is proportional to the Bose factor so that the scattering rate is proportional to

$$\frac{1}{\tau}\sim\frac{1}{e^{\hbar\omega/k_{\mathrm{B}}T}-1}. \tag{2.97}$$

Fig. 2.5: Fig/chapter2-fig6.pdf

At high temperatures $T \gg \Theta_D$, where $\Theta_D = \hbar\omega_D/k_\mathrm{B}$ is the Debye temperature, where ω_D is the the Debye cutoff frequency, the scattering time thus varies as T^{-1} since

$$\tau \sim \hbar\omega/k_\mathrm{B}T, \tag{2.98}$$

while at low temperatures $T \sim \Theta_D$, an exponential temperature dependence for τ is found

$$\tau \sim e^{\hbar\omega/k_\mathrm{B}T} - 1. \tag{2.99}$$

These temperature dependences are important in considering the lattice contribution to the thermal conductivity.

Chapter 3

Quantum effect in thermoelectricity of low-dimensional materials

The aim of this chapter is to draw a simple picture of quantum effect in thermoelectricity in a Fermi liquid. Recently, we have introduced a new concept in the thermoelectric field, in which the interplay between the confinement length L and the thermal de Broglie wavelength Λ can enhance the thermoelectric power factor of semiconducting materials [20]. In this chapter, we will discuss a physical picture of these lengths for the thermoelectric properties of low-dimensional materials. Then an analytical formula for the optimum PF is derived based on the one-band model assuming nondegenerate semiconductors as discussed in Section 2.1.2.1. The PF is enhanced for one- and two-dimensional semiconductors when L is smaller than Λ of the semiconductors. In this case, the low-dimensional semiconductors having L smaller than their Λ will give a better thermoelectric performance compared to their bulk counterpart. On the other hand, when L is larger than Λ, bulk semiconductors may give a higher PF compared to the lower dimensional ones.

3.1 Picture in physic of lengths

In the Section 2.1.2, we show that the PF depends on the thermal de Broglie wavelength Λ, which is defined as

$$\Lambda = \sqrt{\frac{2\pi\hbar^2}{mk_{\mathrm{B}}T}}. \tag{3.1}$$

In Fig. 3.1, we show Λ as function of the temperature T and the relative effective mass m. When the temperature T is sufficiently low, for Λ to become longer than the average distance between two fermions, the system becomes so-called *degenerate* system [47]. Thus, at the Fermi temperature $T_{\mathrm{F}} = E_{\mathrm{F}}/k_{\mathrm{B}}$, where E_{F} is the Fermi energy and k_{B} is the Boltzmann constant, $\Lambda = \sqrt{\frac{2\pi\hbar^2}{mE_{\mathrm{F}}}}$ for each particle become almost

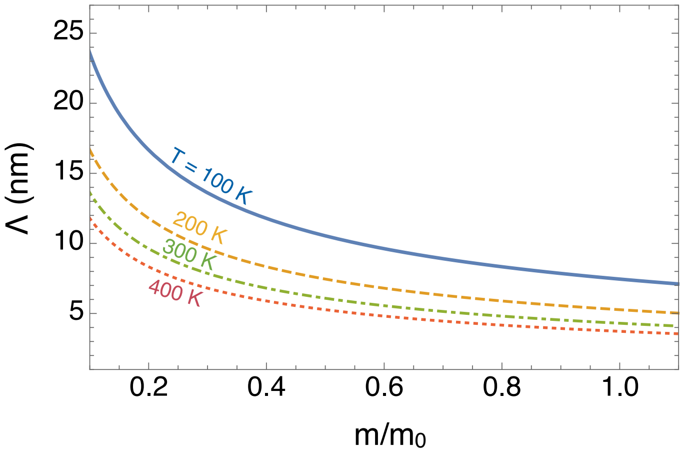

Figure 3.1 Thermal de Broglie wavelength as a function of effective mass m/m_0 (m_0 is the mass of a free electron) for several different temperature values.

equal to the average inter-particle distance $\left(\frac{V}{N}\right)^{1/3}$, where N is the number of particles and V is the volume of the system. Note that $\left(\frac{V}{N}\right)^{1/3}$ for three-dimensional system is given by $\left(\frac{V}{N}\right)^{1/3} = \sqrt{\frac{(3\pi^2)^{2/3}\hbar^2}{2mE_\mathrm{F}}}$ [47]. This is one definition of the thermal de Broglie wavelength. Another definition for Λ is based on the thermodynamic uncertainty principle (see Appendix A). The thermal de Broglie wavelength is a measure of the thermodynamic uncertainty in the localization of a particle whose momentum is set by thermal energy $k_\mathrm{B}T$. Note that the heavier the quasi-particles leads to the shorter Λ and the Λ diverges at the zero temperature.

When we consider the carriers in the reciprocal space, it is useful to define the counterparts of Λ in the reciprocal space. The Fermi wavelength Λ_F is inversely proportional to the Fermi wavevector $\mathbf{k}_\mathrm{F}$ as

$$\Lambda_\mathrm{F} = \frac{2\pi}{\mathbf{k}_\mathrm{F}}, \tag{3.2}$$

where $\mathbf{k}_\mathrm{F}$ is the radius of the Fermi sphere in the reciprocal space of a (1D, 2D, and 3D) gas systems. Similarly, we can define a thermal de Broglie wavevector as

$$\mathbf{k}_\mathrm{dB} = \frac{2\pi}{\Lambda}. \tag{3.3}$$

What is the physical meaning of $\mathbf{k}_\mathrm{dB}$ in the reciprocal space? To answer this question we will use the Fermi-Dirac distribution function, which is given by [Eq. (2.1)]

$$f_0(E) = \frac{1}{1 + e^{\frac{E-E_\mathrm{F}}{k_\mathrm{B}T}}}. \tag{3.4}$$

Fig. 3.1: Fig/chapter3-fig1.pdf

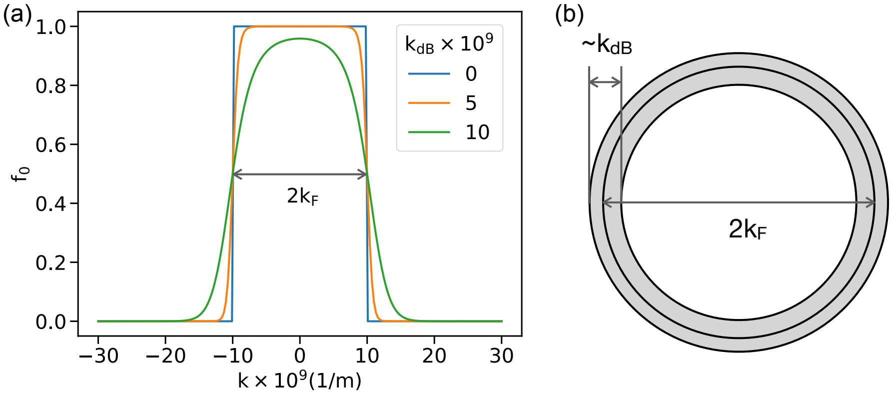

Figure 3.2 (a) The Fermi-Dirac distribution function for the 3D system is plotted as function of the wavevector $\mathbf{k}$ for several values of the thermal de Broglie wavevector $\mathbf{k}_{\mathrm{dB}}$. The Fermi wavevector $\mathbf{k}_{\mathrm{F}}$ is set at 10×10^9 m^{-1}. (b) $\mathbf{k}_{\mathrm{dB}}$ in the reciprocal space. $2\mathbf{k}_{\mathrm{F}}$ is the diameter of the Fermi sphere, and $\mathbf{k}_{\mathrm{dB}}$ is its thermal thickness, set by temperature and the effective mass.

Substituting Eqs. (3.1), (3.2), and $E_{\mathrm{F}} = \hbar^2\mathbf{k}_{\mathrm{F}}^2/2m$ into Eq. (3.4), the Fermi-Dirac distribution function can be rewritten as

$$f_0(\mathbf{k}) = \frac{1}{1 + e^{\frac{\mathbf{k}^2-\mathbf{k}_{\mathrm{F}}^2}{\mathbf{k}_{\mathrm{dB}}^2}\pi}}. \tag{3.5}$$

In Fig. 3.2(a), we show the Fermi-Dirac distribution function f_0 for the 3D system as function of the wavevector $\mathbf{k}$ and the thermal de Broglie wavevector $\mathbf{k}_{\mathrm{dB}}$, in which $\mathbf{k}_{\mathrm{F}}$ is set at 10×10^9 m^{-1}. We note that, giving a Fermi energy $E_{\mathrm{F}} \sim 4$ eV and using the effective mass $m = m_0$, where m_0 is the mass of a free electron, then we have $\mathbf{k}_{\mathrm{F}} = 10.2 \times 10^9$ m^{-1} and $\Lambda_{\mathrm{F}} = 0.6$ nm, while $\mathbf{k}_{\mathrm{dB}} = 1.5 \times 10^9$ m^{-1} and $\Lambda = 4.3$ nm. As show in Fig. 3.2(a), the Fermi-Dirac distribution function for several values of $\mathbf{k}_{\mathrm{dB}}$ present a transition from the occupied to the unoccupied states will become broader as $\mathbf{k}_{\mathrm{dB}}$ increases (or Λ decreases). In the case $\mathbf{k}_{\mathrm{dB}} = 0$ (or $\Lambda = \infty$), the distribution becomes $f_0(E)$ in Eq. (3.4) at $T = 0$. Interestingly, when the system is warmed to T_{F}/π, the $\mathbf{k}_{\mathrm{dB}}$ and $\mathbf{k}_{\mathrm{F}}$ become equal. Above this temperature, the system becomes *non-degenerate* system. Since the Fermi temperature T_{F} has an extremely large magnitude, typically on the order of $\sim$ 10000 K, the system is a *degenerate* system in the normal case. Thus in the normal case, $\mathbf{k}_{\mathrm{dB}}$ is smaller than $\mathbf{k}_{\mathrm{F}}$ and quantifies the thermal thickness ($\sim \mathbf{k}_{\mathrm{dB}}$) of the Fermi surface in the $\mathbf{k}$-space as shown in Fig. 3.2(b). It is noted that the definition of $\mathbf{k}_{\mathrm{dB}}$ for the 1D and 2D systems are the same as the case of the 3D system, which will be discussed as below.

Fig. 3.2: Fig/chapter3-fig2.pdf
Fig. 3.3: Fig/chapter3-fig3.pdf

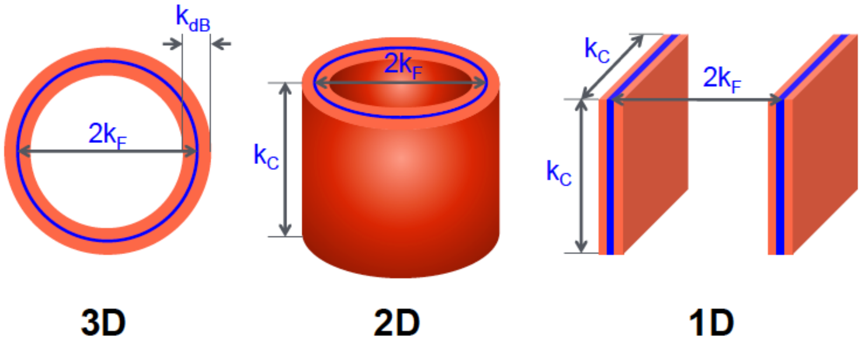

Figure 3.3 Hollow sphere, hollow cylinder and flat sheets Fermi surfaces for 3D, 2D, and 1D systems, respectively. The volume of carriers, which will contribute to the transport properties, are characterized by three wavevectors $\mathbf{k}_\mathrm{F}$, $\mathbf{k}_\mathrm{C}$, and $\mathbf{k}_\mathrm{dB}$.

Now we will discuss the confinement length L in the reciprocal space. We also introduce a wavevector for the confinement length as

$$\mathbf{k}_\mathrm{C} = \frac{2\pi}{L}. \tag{3.6}$$

In Fig. 3.3, we show the hollow sphere, hollow cylinder and flat sheets Fermi surfaces for 3D, 2D, and 1D systems, respectively. As discussed above, there are only the carriers around the Fermi surfaces with a thermal thickness $\sim \mathbf{k}_\mathrm{dB}$ which contribute to the transport properties. For low-dimensional systems (1D and 2D), these carriers are also confined by a confinement length wavevector $\mathbf{k}_\mathrm{C}$, which corresponds the thickness (2D) or edge lengths of the cross section (1D). Therefore, it is clear that the transport properties depend on not only $\sim \mathbf{k}_\mathrm{dB}$ (or Λ) but also $\mathbf{k}_\mathrm{C}$ (or L) in the low-dimensional materials.

3.2 Optimum power factor of low-dimensional materials

From Eq. (2.51), the thermoelectric power factor can be written as

$$\mathrm{PF} = A(\eta - C)^2 e^\eta, \tag{3.7}$$

where A (in units of W/mK^2) and C (dimensionless) are given by

$$A = \frac{4\mu_0 k_\mathrm{B}^2}{qL^3}\left(\frac{L}{\Lambda}\right)^d \frac{\left(r+\frac{d}{2}\right)\left(r,\frac{5}{2}\right)}{d\,\mathrm{B}\left(r,\frac{d}{2}\right)}, \tag{3.8}$$

and

$$C = r + \frac{d}{2} + 1. \tag{3.9}$$

We can now determine the optimum power factor as a function of the dimensionless chemical potential $\eta = \mu/k_\mathrm{B}T$ from Eq. (3.7) by solving $\mathrm{d(PF)/d}\eta = 0$. The optimum

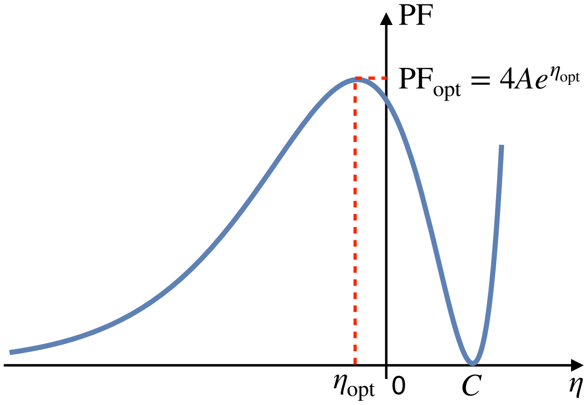

Figure 3.4 The power factor as a function of the reduced chemical potential η for the non-degenerate semiconductors.

power factor, $\mathrm{PF}_{\mathrm{opt}}$, and the corresponding value for the reduced (or dimensionless) chemical potential, η_{opt}, are given, respectively, by

$$\mathrm{PF}_{\mathrm{opt}} = \frac{16\mu_0 k_{\mathrm{B}}^2}{qL^3}\left(\frac{L}{\Lambda}\right)^d \frac{\left(r+\frac{d}{2}\right)\mathrm{B}\left(r,\frac{5}{2}\right)}{d\,\mathrm{B}\left(r,\frac{d}{2}\right)} e^{r+d/2-1}, \tag{3.10}$$

and

$$\eta_{\mathrm{opt}} = r + \frac{d}{2} - 1. \tag{3.11}$$

In Fig. 3.4, we shows the PF as a function of η. Since η is measured from the top of the valence band, $\eta_{\mathrm{opt}} < 0$ ($\eta_{\mathrm{opt}} > 0$) corresponds to a condition in which the Fermi energy is located inside (outside) the energy gap. Here we assume that the energy gap is much larger than $k_{\mathrm{B}}T$ for the non-degenerate semiconductors. For example, in the 1D system, if r and d are taken to be 0 and 1 [41], respectively, Eq. (3.11) gives $\eta_{\mathrm{opt}} = -\frac{1}{2}$ which means that η_{opt} is located around $\frac{1}{2}k_{\mathrm{B}}T$ ($\sim$ 0.013 eV at 300 K) below the top of the valence band. Since the values of the characteristic exponent r in the description of $\tau(E)$ [Eq. (2.28)] are ranging from -0.5 to 1.5 for various scattering processes [41, 48, 49, 50], we find that the range of the η_{opt} values would be $(-1, 1)$, $(-\frac{1}{2}, \frac{3}{2})$, and $(0, 2)$ for the 1D, 2D, and 3D systems, respectively. Therefore, the small η_{opt} value will make position of the Fermi energy below (within a few $k_{\mathrm{B}}T$) the valence band edge for the p-type semiconductor [51]. It is noted that for an n-type semiconductor, we can redefine η to be measured from the bottom of the conduction band. We also note that the PF in Eq. (3.10) is derived by using the one-band model. Therefore, if we consider 1D and 2D systems having quite large confinement length L such that many subbands contribute to the transport properties at the same time, the electronic density of states would resemble the 3D system [52]. In such a case, the

---

Fig. 3.4: Fig/chapter3-fig4.pdf

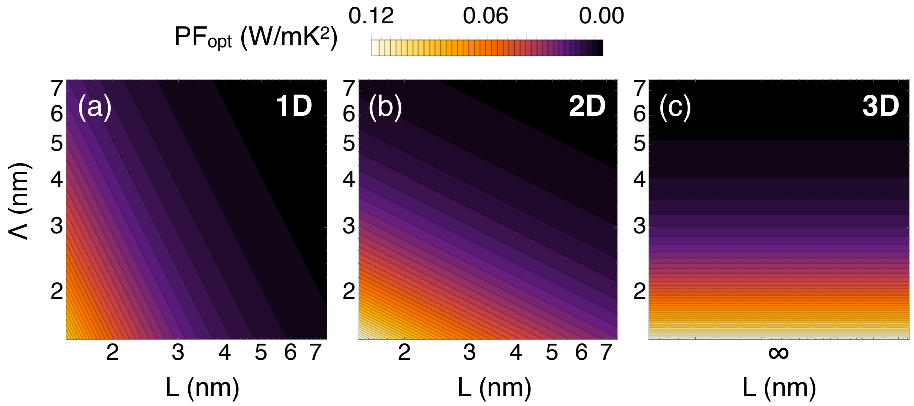

Figure 3.5 Optimum power factor PF$_{\text{opt}}$ as a function of confinement length L and thermal de Broglie wavelength Λ for (a) 1D, (b) 2D, and (c) 3D systems.

one-band model does not work well to describe the thermoelectricity because several subband energies fall within a few $k_{\text{B}}T$ window around the Fermi energy, which is beyond the scope of this model. We will discuss in Chapter 4 for the case of multi-band.

3.3 Quantum and classical size effects on power factor

In Fig. 3.5, we shows PF$_{\text{opt}}$ Eq. (3.10) as a function of confinement length L and thermal de Broglie wavelength Λ for the 1D, 2D, and 3D systems. The mobility is set to be $\mu_0 = 420$ cm^2/Vs for all systems and the scattering rate is proportional to be the density of states (DOS) (see Section 2.1.3). The assumption of proportionality of the scattering rate with respect to the DOS, the scattering rate corresponds to $r = +0.5$, $r = 0$ and $r = -0.5$ for 1D, 2D, and 3D systems, respectively [48]. The curves in the left and middle panel of Fig. 3.5 particularly show a L^{-2} and L^{-1} dependence of the power factor for 1D and 2D systems, respectively [Eq. (3.10)]. These results are in good agreement with the model by Hicks and Dresselhaus [1, 2]. It is important to point out that the dependence of PF$_{\text{opt}}$ on Λ also needs to be considered. For an ideal electron with dimensionless d gas under the trapping potential, the thermodynamic uncertainty principle may roughly be expressed as $\Delta P/P \times \Delta V/V \geq (d^{3/2}/\sqrt{2\pi})\Lambda/L$, where P and V are the pressure and volume of the system, respectively (see in Appendix A). The uncertainty principle ensures that when the confinement length is comparable with the thermal de Broglie wavelength, i.e., $L \leq (d^{3/2}/\sqrt{2\pi})\Lambda$, the P and V cannot be treated as commuting observables. In this case, the quantum effects play an important role in increasing PF$_{\text{opt}}$ for nanostructures. For the 1D system [Fig. 3.5 (a)] PF$_{\text{opt}}$ starts to increase significantly when L is much smaller than Λ, while for the 2D system

---

Fig. 3.5: Fig/chapter3-fig5.pdf

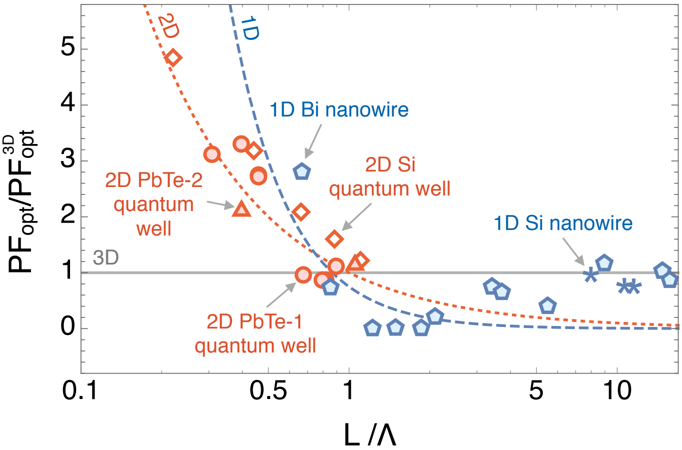

Figure 3.6 Enhancement factor $\mathrm{PF_{opt}}/\mathrm{PF_{opt}^{3D}}$ as a function of L/Λ for different dimensions. The L/Λ axis is given using a logarithmic scale. Theoretical results for 1D, 2D, and 3D systems are represented by dashed, dotted, and solid lines, respectively. Asterisks, pentagons, diamonds, circles, and triangles denote experimental results for 1D Si nanowires [4], 1D Bi nanowires [16], 2D Si quantum wells [53], 2D PbTe-1 quantum wells [54], and 2D PbTe-2 quantum wells [55], respectively. For the experimental results, we set the thermal de Broglie wavelength of each material as: $\Lambda_{\mathrm{Bi}} = 32$ nm, $\Lambda_{\mathrm{Si}} = 4.5$ nm, and $\Lambda_{\mathrm{PbTe}} = 5$ nm. We also have the following PF values for 3D systems: $\mathrm{PF_{Bi}^{3D}} = 0.002$ W/mK^2 [16], $\mathrm{PF_{Si}^{3D}} = 0.004$ W/mK^2 [56], $\mathrm{PF_{PbTe-1}^{3D}} = 0.002$ W/mK^2 [54], and $\mathrm{PF_{PbTe-2}^{3D}} = 0.003$ W/mK^2 [55].

[Fig. 3.5 (b)] $\mathrm{PF_{opt}}$ starts to increase significantly when L is comparable to Λ. As for the 3D system [Fig. 3.5 (c)], $\mathrm{PF_{opt}}$ increases with decreasing Λ for any L values. Therefore, a nanostructure having both small L and Λ (while L is also much smaller than its Λ) will be the most optimized condition to enhance the PF.

Now we can compare our model with various experimental data. In Fig. 3.6, we show $\mathrm{PF_{opt}}$ [Eq. (3.10)] as a function of L/Λ for the 1D, 2D, and 3D systems. The $\mathrm{PF_{opt}}$ values are scaled by the optimum power factor of a 3D system, $\mathrm{PF_{opt}^{3D}}$. From Eq. (3.10), the enhancement factor is given by the ratio $\mathrm{PF_{opt}}/\mathrm{PF_{opt}^{3D}} \sim (L/\Lambda)^{d-3}$ for $d = 1, 2$ (1D and 2D). Hence, the enhancement factor from various materials can be compared directly with the theoretical curves shown in Fig. 3.6. The experimental data in Fig. 3.6 are obtained from the PF values of 1D Bi nanowires [16], 1D Si nanowires [4], 2D Si quantum wells [53], and two different experiments of 2D PbTe quantum wells labeled by PbTe-1 and PbTe-2 [54, 55]. Here we use fixed parameters for the thermal de Broglie wavelength of each material: $\Lambda_{\mathrm{Bi}} = 32$ nm, $\Lambda_{\mathrm{Si}} = 4.5$ nm, and $\Lambda_{\mathrm{PbTe}} = 5$ nm. We also set some PF values for 3D systems: $\mathrm{PF_{Bi}^{3D}} = 0.002$ W/mK^2 [16], $\mathrm{PF_{Si}^{3D}} = 0.004$ W/mK^2 [56], $\mathrm{PF_{PbTe-1}^{3D}} = 0.002$ W/mK^2 [54], and $\mathrm{PF_{PbTe-2}^{3D}} = 0.003$ W/mK^2 [55], which are necessary to put all the experimental results into Fig. 3.6.

We find that the curves in Fig. 3.6 demonstrate a strong enhancement of $\mathrm{PF_{opt}}$

Fig. 3.6: Fig/chapter3-fig6.pdf

in 1D and 2D systems when the ratio L/Λ is smaller than the unity (or $L < \Lambda$). In contrast, if L is larger than Λ, the bulk 3D semiconductors may give a larger $\mathrm{PF}_{\mathrm{opt}}$ value than the lower dimensional semiconductors, as shown in Fig. 3.6 up to a limit of $L/\Lambda \approx 2$. We argue that such a condition is the main reason why an enhanced PF is not always observed in some low-dimensional materials although experimentalists have reduced the size of material. For example, in the case of 1D Si nanowires, where we have $\Lambda_{\mathrm{Si}} \sim 4.5$ nm, we can see that the experimental PF values in Fig. 3.6 are almost the same as the $\mathrm{PF}_{\mathrm{opt}}^{\mathrm{3D}}$. The reason is that the diameters (supposed to represent L) of the 1D Si nanowires, which were about 36-52 nm in the previous experiments [3, 4], are still too large compared with Λ_{Si}. It might be difficult for experimentalists to obtain a condition of $L < \Lambda$ for the 1D Si nanowires. In the case of materials having larger Λ, e.g., Bi with $\Lambda_{\mathrm{Bi}} \sim 32$ nm, the PF values of the 1D Bi nanowires can be enhanced at $L < \Lambda$, which is already possible to achieve experimentally [16]. Furthermore, when $L \gg \Lambda$, it is natural to expect that $\mathrm{PF}_{\mathrm{opt}}$ of 1D and 2D semiconductors resemble $\mathrm{PF}_{\mathrm{opt}}^{\mathrm{3D}}$ as shown by some experimental data in Fig. 3.6. It should be noted that, within the one-band model, we do not obtain a smooth transition of $\mathrm{PF}_{\mathrm{opt}}$ in Fig. 3.6 from the lower dimensional to the 3D characteristics for large L because we neglect contributions coming from many other subbands responsible for the appearance of the 3D DOS [52]. Very recently, Ohta et al. [57, 58], who is motivated by this model, have shown the observation of high PF (~ 9 mWm^{-1}K^{-2}) in 2D GaN at room temperature, which is an order magnitude higher than that of 3D GaN, when the confinement length (~ 2 nm) is smaller than the thermal de Broglie wavelength (~ 10 nm).

So far, we have used the confinement length L as an independent parameter in Eq. (2.46). However, for extremely thin films or nanowires, L is expressed by two components as $L = L_0 + \Delta L$, where L_0 is the thickness of the material and ΔL is the size of the evanescent electron wavefunction beyond the surface boundary. Within the box of L_0 the electron wavefunction is delocalized, approximated by the linear combination of plane waves, while within ΔL the electron wavefunction is approximated by evanescent waves. For a single-layered material, e.g., a hexagonal boron nitride (h-BN) sheet, $L_0 \approx 0$ so that $L \approx \Delta L = 0.333$ nm [59]. As for ultra-thick 1D nanowires or 2D thin films, we have $L \gg \Delta L$, and thus the confinement length is mostly determined by the size of the material such as $L \approx L_0$. Creating a 1D channel from a 2D material by applying negative gate voltages on two sides of the 2D material can be an example to engineer the confinement length [60]. However, unlike L, which can be controlled by engineering techniques within the same material, the thermal de Broglie wavelength Λ is temperature-dependent and intrinsic for each material. As shown in Fig. 3.1, we can see that Λ decreases ($\propto T^{-1/2}$ or $m^{-1/2}$) with increasing temperature T or with increasing effective mass m, which indicates that the $\mathrm{PF}_{\mathrm{opt}}$ [$\propto (L/\Lambda)^d$] of nondegenerate semiconductors would be enhanced at higher T or at larger m (smaller Λ). This result is consistent with the experimental observations for the PF values of Si and PbTe, which are monotonically increasing as a function of temperature [4, 56, 61]. It should be noted that Λ is not necessarily independent of L and d because the term m may be altered by varying L or by changing d. This fact might contribute to the small discrepancy between the PF values from our theory and those from experiments since we set Λ as a fixed quantity upon variation of L in 1D and 2D systems (see Fig. 3.5). For the 3D system, the theoretical values ($\mathrm{PF}_{\mathrm{Bi}}^{\mathrm{3D}} = 0.0019$ W/mK^2 and $\mathrm{PF}_{\mathrm{Si}}^{\mathrm{3D}} = 0.0044$ W/mK^2) are in good agreement with the experimental data ($\mathrm{PF}_{\mathrm{Bi}}^{\mathrm{3D}} = 0.002$ W/mK^2 [16] and $\mathrm{PF}_{\mathrm{Si}}^{\mathrm{3D}} = 0.004$ W/mK^2 [56]).

Chapter 4

Thermoelectric properties of two-dimensional InSe

In this Chapter, we show the thermoelectric properties of two-dimensional (2D) InSe by using the Boltzmann transport formalism combined with the density functional theory (DFT) as a function of Fermi energy and crystal orientation. In Section 4.3, we show that the maximum power factor of p-type (n-type) monolayer InSe can be as large as 0.049 (0.043) W/K^{2}m at 300K in the armchair direction. The excellent thermoelectric performance of monolayer InSe is attributed to both its Seebeck coefficient and electrical conductivity. In Section 4.4, we also investigate a possibility of improving thermoelectric performance of monolayer InSe through convergence of multivalley energy bands (CMB), in which some distinct valleys become almost degenerate. The CMB is achieved by applying mechanical strain. We show that the thermoelectric power factor of monolayer InSe can be significantly enhanced by nearly a factor of 3 through the CMB in both valence (p-type) and conduction (n-type) bands under a biaxial compressive stress of about 1.16 GPa. However, the maximum enhancement of the figure of merit ZT in the p-type and n-type InSe are different from each other depending on how the valleys converge in each case. The optimal scenario is that the heavy valleys approach the light valleys in the band convergence, which leads to an increase in the power factor and, at the same time, a decrease in the thermal conductivity of electron. This optimal condition can be obtained in the strained n-type InSe that gives the largest enhancement of ZT as high as 230% ZT of unstrained InSe. In contrast, the enhancement of ZT in the strained p-type InSe, which exhibits the opposite valley convergence (light valleys joining heavy ones) to the n-type InSe, gives only 26% ZT of unstrained InSe.

4.1 Method and computational details for InSe

In this section, we evaluate the thermoelectric properties of monolayer InSe by the Boltzmann transport theory and first-principles calculations. To calculate the transport coefficients, i.e., Seebeck coefficient S, electrical conductivity σ, and electronic thermal conductivity κ_e we need the electronic energy dispersion $E_{n\mathbf{k}}$ and the carrier relaxation time $\tau_{n\mathbf{k}}$ for each band n and for each wave vector $\mathbf{k}$ (see Section 2.1). The electronic structure are performed by using `Quantum ESPRESSO` [62]. The ground-state electronic structure is calculated within the norm-conserving pseudopotential with the Perdew-Zunger [63] local density approximation (LDA) [64] for the exchange-correlation functional and a plane-wave basis set with kinetic energy cutoff of 160 Ry. Note that the LDA without spin-orbit interaction is adopted in this work because the band gap is not really affected by the spin-orbit interaction. [65] The system is modeled by adopting a hexagonal supercell geometry where the vacuum distance is set to 12 Å to eliminate the interactions between the InSe layer and focus on the monolayer in the simulation. To obtain the the optimized geometry, the atomic positions and supercell vectors are fully relaxed by using the Broyden-Fretcher-Goldfarb-Shanno minimization method. [66, 67, 68, 69] This system is considered to be optimized when all the Hellmann-Feynman forces and all components of the stress are less than 5.0×10^{-4} Ry/a.u. and 5.0×10^{-2} GPa, respectively, which are adequate for the present purpose.

We employ the electron-phonon Wannier (EPW) package [70] to calculate the electron-phonon relaxation time, $\tau_{n\mathbf{k}} = \hbar(\mathrm{Im}\sum_{n\mathbf{k}})^{-1}/2$, where $\hbar$ is the Planck constant and $\mathrm{Im}\sum_{n\mathbf{k}}$ is the imaginary part of the electron self-energy of the n^{th} band at a given $\mathbf{k}$ point. We use Gaussian broadening of 10 meV to approximate the Dirac delta function in the electron self-energy. The electron energy and phonon dispersions are initially calculated on $24 \times 24 \times 1$ $\mathbf{k}$-point and $6 \times 6 \times 1$ $\mathbf{q}$-point grids for the first Brillouin zone using DFT and density functional perpetuation theory (DFPT) [71], respectively. Since a finer grid is required to evaluate the transport coefficients, we interpolate the electronic energy and phonon dispersions on a dense mesh of both $\mathbf{k}$ and $\mathbf{q}$ points of $200 \times 200 \times 1$, which is sufficient to obtain convergence of the transport coefficients [72]. In this calculation, all electron-phonon scattering processes due to acoustic, optical, and polar-optical phonons are considered.

Using the output data from first-principles calculations, we can obtain the Seebeck coefficient S, electrical conductivity σ, and electronic thermal conductivity κ_e along a certain direction (zigzag or armchair) of monolayer InSe by employing the relaxation-time approximation of the Boltzmann equation in our own computer code. For one particular direction, the formulas for S, σ, and κ_e can be expressed by the transport integral $\mathcal{L}_i$ [see Eqs. (2.23)-(2.25)]:

$$\sigma = q^2\mathcal{L}_0, \quad S = \frac{1}{qT}\frac{\mathcal{L}_1}{\mathcal{L}_0}, \quad \kappa_{\rm el} = \frac{1}{T}\left(\mathcal{L}_2 - \frac{\mathcal{L}_1^2}{\mathcal{L}_0}\right), \tag{4.1}$$

where q is the charge of carrier (electron or hole). $\mathcal{L}_i$ is defined by [see Eq. (2.21)]

$$\mathcal{L}_i = -\frac{2}{NV}\sum_{n\mathbf{k}} v_{n\mathbf{k}}^2 \tau_{n\mathbf{k}} \frac{\partial f_0}{\partial E}(E_{n\mathbf{k}} - E_{\rm F})^i, \ i = 0, 1, 2, \tag{4.2}$$

where N is the number of $\mathbf{k}$ points, V is the volume of the unit cell using a constant thickness of 0.8 nm for the monolayer InSe, $E_{\rm F}$ is the Fermi energy, $f_{n\mathbf{k}}$ is the Fermi-Dirac distribution function, $v_{n\mathbf{k}} = \nabla_{\mathbf{k}} E_{n\mathbf{k}}/\hbar$ is the component of the group velocity in zigzag or armchair direction, and the factor 2 accounts for the spin degeneracy [5]. Eventually, the power factor PF and the figure of merit ZT can be calculated by using the following formulas:

$$\mathrm{PF} = S^2\sigma, \tag{4.3}$$

and

$$ZT = \frac{S^2\sigma T}{\kappa_{\rm el} + \kappa_{\rm ph}}, \tag{4.4}$$

where $\kappa_{\rm ph}$ is the lattice thermal conductivity. Here we simply adopted $\kappa_{\rm ph}$ for monolayer InSe of about 27 W/mK [73] for the calculations of PF and ZT.

4.2 Structure and electronic properties

In Fig. 4.1(a), we show the top view and side view of the unit cell of monolayer InSe with the lattice constant $a = 3.902$ Å. Two sublayers exists in a monolayer InSe, in which the first and second sublayers are separated by $d_{\rm In} = 2.662$ Å and $d_{\rm Se} = 5.147$ Å from the optimized geometry calculation. In Fig. 4.1(b), we give the calculated electronic structure of the monolayer InSe from the LDA calculation. The minimum point of the first conduction band appears at the Γ point, while the maximum of the first valence band appears at a point along the Γ-M direction. The indirect band gap of monolayer InSe within the LDA is about 2.06 eV. Here $E_{\rm F} = 0$ is set to be in the center of the energy gap. Since the Seebeck coefficients are sensitive to the shape of the band gap, we also check the band gaps obtained by using the Perdew-Burke-Ernzerhof (PBE) [74] and the Heyd-Scuseria-Ernzerhof (HSE) [28] hybrid functionals, which result in band gaps of about 1.55 eV and 2.24 eV, respectively. The HSE approach is the closest to the band gap of monolayer InSe observed in the experiment [30]. However, the EPW package does not support the HSE pseudopotential [70]. Therefore, the LDA with 2.06 eV band gap is a reasonable approximation in this study. Figure 4.1(c) shows the DOS of the monolayer InSe, in which we can see a very sharp DOS at the

---

Fig. 4.1: Fig/chapter4-fig1.pdf

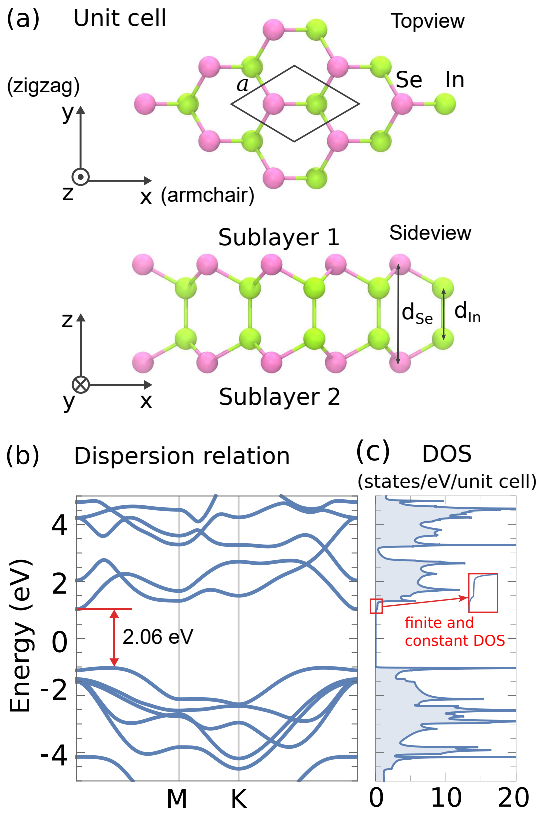

Figure 4.1 Lattice structure and electronic properties of monolayer InSe. (a) Top view and side view of the unit cell. There are two sublayers in a monolayer InSe. The x- and y-axes correspond to the armchair and zigzag directions, respectively. (b) Electronic energy dispersion of monolayer InSe. (c) Density of states (DOS). Relatively constant DOS in the conduction band is enclosed by a red box.

top of the valence band due to the quartic energy dispersion. In the conduction band, a finite and almost constant 2D DOS appears for a limited range within 1.0-1.3 eV due to the parabolic energy dispersion as shown in red box. We argue that the existence of such a characteristic for DOS should be relevant to the excellent thermoelectric properties of the 2D monolayer InSe that we will discuss below.

4.3 Power factor of two-dimensional InSe

In Figs. 4.2(a-d), we show the transport and thermoelectric properties of monolayer InSe. Firstly, in Fig. 4.1(a), we plot the scattering rate $(1/\tau_{n\mathbf{k}})$ for all $\mathbf{k}$ states in the electron energy range $[-2.0, 2.0]$ eV for three different temperatures at 300 K, 500 K, and 700 K with $E_F = 0$ eV. Carrier densities for $E_F = -2$ eV and $E_F = 2$ eV are

---

Fig. 4.2: Fig/chapter4-fig2.pdf

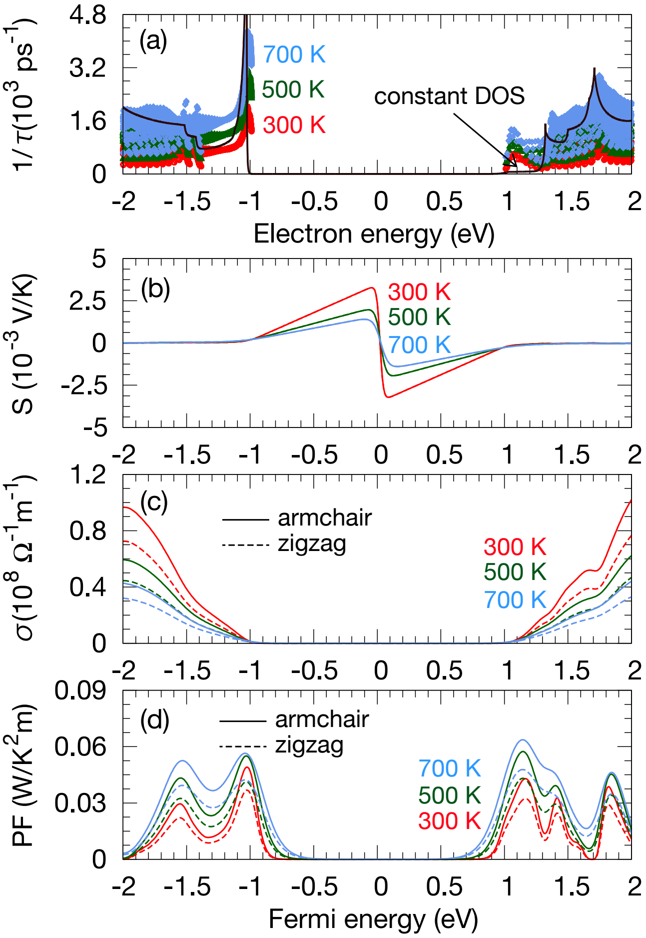

Figure 4.2 Transport and thermoelectric properties of monolayer InSe. (a) Carrier scattering rate (inverse of relaxation time) as a function of electron energy in a logarithmic scale. Solid line is the DOS of monolayer InSe. (b) Seebeck coefficient, (c) electrical conductivity, and (d) power factor as a function of Fermi energy for three different temperatures at 300 K, 500 K, and 700 K. Solid and dashed lines in (b-d) for each temperature denote the quantities along the armchair and zigzag directions, respectively. Note that the different directions give negligible difference of the Seebeck coefficients so that two curves for each temperature in (b) overlap each other.

respectively 2.75×10^{13} cm^{-2} and 1.875×10^{13} cm^{-2} for hole doping and electron doping. Since $1/\tau \propto DOS$ [see Section 2.1.3], the shape of the $1/\tau$ curve resembles that of the DOS that is plotted by solid line. When we increase temperature, the relaxation time $\tau_{n\mathbf{k}}$ decreases. We find a relatively small value of scattering rate at the conduction band of monolayer InSe, which means a larger relaxation time at energy around 1.0-1.3 eV where a constant small DOS appears. We thus expect that the conductivity σ and power factor $\mathrm{PF} = S^2\sigma$ are enhanced in this conducting regime for the n-type InSe. On the other hand, within the valence band, the scattering rate is relatively large (the relaxation time is small) but there is a very sharp DOS at energy around top of the valence band which, according to the Mahan-Sofo theory, [38] is also a good region to obtain an enhancement of the PF from the enhancement of S in the PF.

In Fig. 4.2(b), we show the calculated Seebeck coefficient S as a function of the Fermi energy E_{F}. For the calculation the thermoelectric properties, we adopt the rigid band approximation, which assumes that the band structure remains unchanged as we shift the Fermi level up and down to simulate the electron and hole doping, respectively. It is a good approximation as long as the doping levels used are not high enough to change the bonding properties of the material [5]. We found the larger S at lower temperature since $S \propto 1/T$ as given in Eq. (1.19). The maximum value of S for monolayer InSe at room temperature can be more than 3000 µV/K, which is also a very large S among the 2D materials. This value of S is mainly determined by the band gap of the monolayer InSe, in which for band gaps much larger than the thermal energy we can approximate the Seebeck coefficient to be proportional to the band gap [75]. It is important to note, however, that the peak S at the energy gap region can not be used since there is no conductivity.

The transport coefficients such as S and σ are often measured in a particular direction [8]. In the case of monolayer InSe, we have defined the armchair and zigzag direction from the x- and y-axes as shown in Fig. 4.1(a). Therefore, besides the temperature dependence, there is also an orientation dependence of the transport coefficients. However, as for the Seebeck coefficient in Fig. 4.2(b), we find that the S values for the two orientations almost overlap to each other. The origin of S can be traced back to the contribution of the group velocity in both the numerator and the denominator parts of Eq. (2.19) for S, where the contribution from group velocity might be canceled by the division. On the other hand, we show in Fig. 4.2(c) that the electrical conductivity σ depends on the crystal orientation because only one group velocity term appears in the expression of σ in Eq. (2.17) and the band structure (thus group velocity) of monolayer InSe is slightly anisotropic. We find that the armchair direction of monolayer InSe gives a larger σ than the zigzag direction.

By combining S with σ, we can calculate $\mathrm{PF} = S^2\sigma$ as a function of the Fermi energy, as shown in Fig. 4.2(d). We obtain the largest PF for the armchair direction at the high temperature of *both* p-type and n-type monolayer InSe. This result is different from the previous work by Wickramaratne et al., [32], in which they stated that the p-type monolayer InSe has a much larger PF than the n-type. The discrepancy between the previous and the current results should come from the fact that they treated the relaxation time τ as a constant, [32] while in this work we consider τ to be energy-dependent as a result of taking the electron-phonon scattering into account. Nevertheless, we note that the PF of p-type monolayer InSe is still on the same order of magnitude with that of the n-type. Therefore, experimentalists could have flexibility to dope monolayer InSe by p-type or n-type dopings and to obtain the most optimized PF depending on the device setup. From our calculation, the optimized carrier density to obtain the maximum PF 0.049 W/K^2m (0.043 W/K^2m) in the p-type (n-type) monolayer InSe is 3.0×10^{12} (0.14×10^{12}) cm^{-3} by hole (electron) doping. The high PF in monolayer InSe (PF = 0.049 W/K^2m for p-type) originates from both the large S and σ, corresponding to the unique band structure of monolayer InSe with semiconducting and unusual shape of DOS, respectively. Furthermore, we have shown in Chapter 3 that one way to obtain large PF is by using a low-dimensional semiconductor with high intrinsic carrier mobility and small confinement length L (the thickness of the 2D material in this case). [20] The confinement length L of monolayer InSe is found to be very small, about 0.8 nm, compared with thermal de Broglie wavelength $\Lambda \sim 10$ nm at room temperature [30] and thus improving the PF of the monolayer InSe compared to its bulk form. Wickramaratne et al., [32] reported PF = 0.006 (0.001) W/K^2m for bulk p-type (n-type) InSe, which is much smaller than that of 2D InSe with PF = 0.049 (0.043) W/K^2m for monolayer p-type (or n-type) InSe. It should be noted that, not only the dimensionality, but the scattering mechanisms and DOS could also be important to enhance the PF of the 2D InSe [76].

4.4 Convergence of multivalley bands

Now, we further improving the thermoelectric properties by applying the strain, which makes two energy bands degenerate. This concept is called by convergence of multivalley bands (CMB). Recently, Pei et al., Tang et al., and Liu et al. [77, 78, 79] showed that the conduction or valence energy band extrema can be tuned to be almost degenerate by doping, modification of composition, or temperature, which can enhance both the PF and ZT in PbTe [77], $CoSb_3$ [78], and $Mg_2(Sn,Si)$ [79]. Thus, we expect that thermoelectric performance of the 2D InSe can be also improved by the CMB. Jin et al. [80] reported that the electronic energy band of the monolayer InSe can be tuned by the in-plane strain. This fact inspired us to study the CMB in monolayer InSe by applying strain, which will be disscued below.

In Fig. 4.3, we show the energy band structures of monolayer InSe for several in-plane biaxial compressive strains ε, which is defined by $\varepsilon = (a - a_0)/a_0$, where a and a_0 are the in-plane lattice constants with strain and unstrain, respectively. In the case of $\varepsilon = 0$, the calculated monolayer InSe has an indirect band gap of 2.06 eV as shown in Fig. 4.3. In the p-type InSe, there exist four "light valleys" (LVs) at the Γ point and one "heavy valley" (HV) along Γ–$M(K)$ line in the valence bands as shown in Fig. 4.3, where the LV and HV denote the valleys having lighter and heavier effective

---

Fig. 4.3: Fig/chapter4-fig3.pdf
Fig. 4.4: Fig/chapter4-fig4.pdf

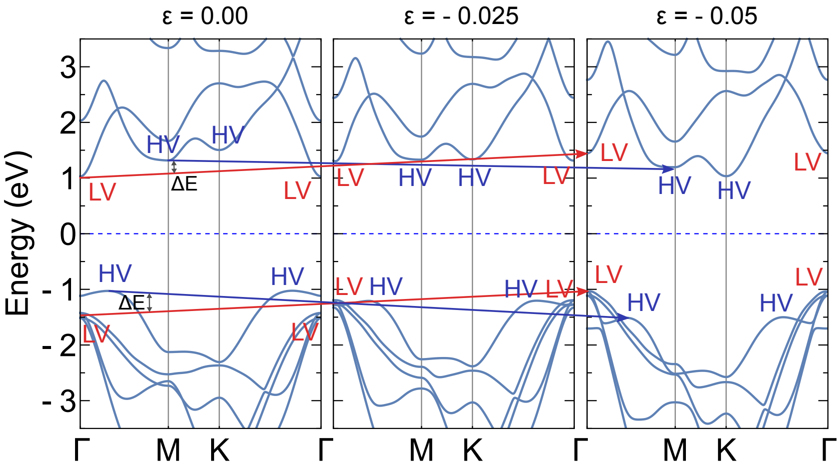

Figure 4.3 Electronic energy dispersion of monolayer InSe under biaxial compressive strains $\varepsilon = (a - a_0)/a_0$.

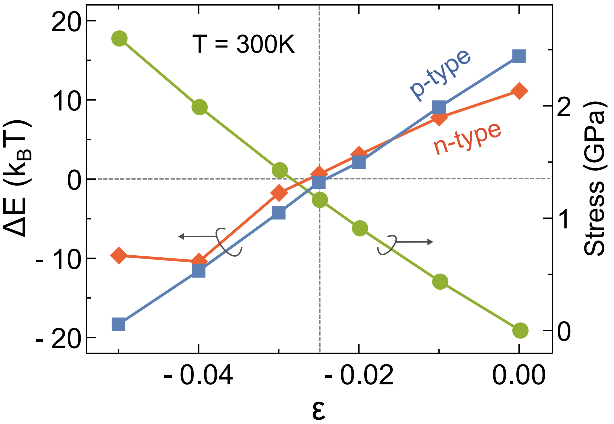

Figure 4.4 Valley splitting energy ΔE and in-plane stress as a function of compressive strains ε. Here ΔE is in the units of $k_B T$ with $T = 300$ K.

masses of electrons, respectively. Similarly, in the case of n-type InSe, there is one LV at the Γ point and two HVs at the M and K points in the conduction bands as shown in Fig. 4.3. The valley splitting energy ΔE between HV and LV for the both cases of conduction and valence bands is indicated in the case of $\varepsilon = 0$ of Fig. 4.3. It is noted that $\Delta E = 0$ represents the case of CMB, in which some distinct valleys become degenerate at $\varepsilon = -0.025$. When *compressive* strain ($\varepsilon < 0$) is applied, the energy extrema (both minima and maxima) of the LVs at the Γ point increase monotonically (see red lines in Fig. 4.3), while the energy extrema of the HVs along the $\Gamma - M(K)$ and at the M and K points decrease (see blue lines in Fig. 4.3). As a result, the value of ΔE at $T = 300$ K decreases approximately linearly with deceasing ε [see Fig. 4.4]. In Fig. 4.4, we plot ΔE for the n-type and p-type as a function of ε, in which we can see that both ΔE values for the p-type and n-type InSe becomes zero at the same compressive strain $\varepsilon = -0.025$, which corresponds to the stress of about 1.16 GPa.

We notice that there are two different behaviors of the CMB in the monolayer InSe depending on the doping. In the p-type InSe, the energy up shift of the LV is larger than that of the HV so that the LV looks like "approaching" the HV (LV → HV). This behavior is opposite in the n-type InSe, in which the HV approaches the LV (HV → LV). Here, we will show in Section 4.4.1 that the case of HV → LV gives much larger enhancement of ZT than the LV → HV, while changes of PF in the two cases are quite similar.

4.4.1 Thermoelectric power factor

In order to discuss the PF in the monolayer InSe, in Fig. 4.5(a), we firstly plot the electrical conductivity σ at 300 K as a function of carrier concentration for the three values of strain ε for both p-type (left figure) and n-type (right figure) InSe along armchair (solid line) and zigzag (dashed line) directions. Note that with our investigated strain range, the monolayer InSe is always a semiconductor with band gap around 2 eV (see Fig. 4.3). For obtaining a large σ, the semiconductor is generally doped. In this present study, doping is treated within the rigid-band model as mention before, in which the corresponding carrier concentration of the 2D materials in units of cm^{-2} can be calculated as $n = \frac{2}{NA}\sum_{n\mathbf{k}} f_{n\mathbf{k}}$, where N is number of k point, A is the area of the unit cell, $f_{n\mathbf{k}}$ is the Fermi-Dirac distribution function, and the factor 2 accounts for the spin degeneracy. The summation for n is taken by the n-th band and all $\mathbf{k}$ in the first Brillouin zone. When no strain is applied ($\varepsilon = 0$), σ shows anisotropy for armchair and zigzag directions at high carrier concentration as shown in Figs. 4.5(a), with the value along the armchair direction larger than that along the zigzag direction. An origin of the anisotropy is due to the different velocities along the armchair and zigzag directions, which has also been confirmed by our previous works [72]. For compressive strain $\varepsilon < 0$, σ of the p-type InSe increases with increasing $|\varepsilon|$ due to the LV → HV, while σ of the n-type InSe decreases with increasing $|\varepsilon|$ due to the HV → LV.

In Fig. 4.5(b), we plot the Seebeck coefficient S at 300 K as a function of the carrier concentration for both p-type and n-type InSe with the three different ε values. The absolute value of S is proportional to $N_v^{2/3}m$ [79], where m is the carrier effective mass and N_v is number of degenerate band valleys. Therefore, the HV with larger effective mass enhances $|S|$, while the LV with lighter effective masses reduces $|S|$. For the p-type InSe (left figure of Fig. 4.5b), the $|S|$ has a maximum at $\varepsilon = -0.025$ due to the CMB. When we increase $|\varepsilon|$ further from $|\varepsilon| = 0.025$, $|S|$ then decreases at $\varepsilon = -0.05$ due to the LV → HV convergence because only the LV contributes to S. On the other hand, for the n-type InSe (right figure of Fig. 4.5b), $|S|$ increases

---

Fig. 4.5: Fig/chapter4-fig5.pdf

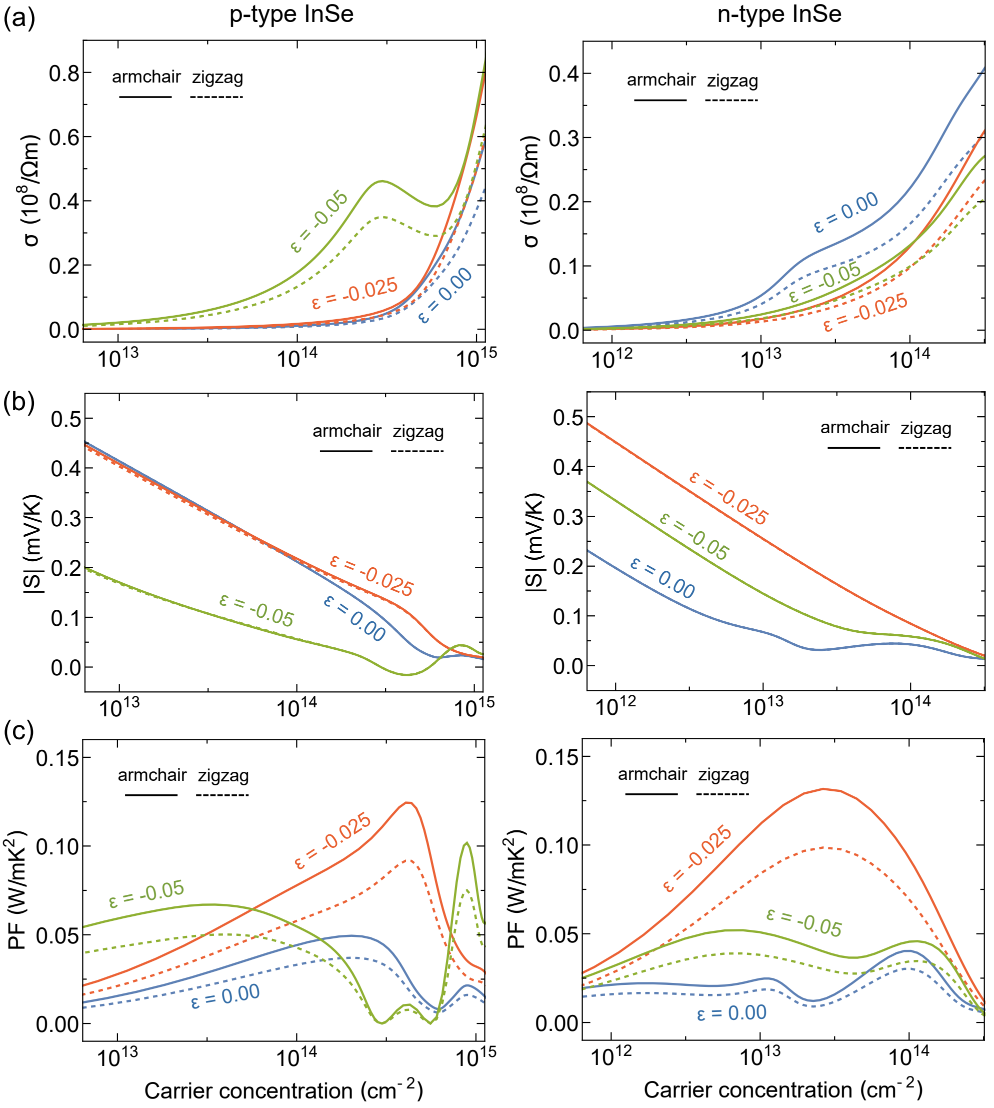

Figure 4.5 (a) Electrical conductivity σ, (b) Seebeck coefficient S, and (c) power factor PF of p-type and n-type monolayer InSe as a function of strain ε and carrier concentration at 300 K. Solid and dashed lines denote armchair and zigzag directions, respectively.

significantly at the optimum at $\varepsilon = -0.025$, and decreases with increasing $|\varepsilon|$ due to the HV $\rightarrow$ LV convergence.

In Fig. 4.5(c), we plot the power factor PF as a function of the carrier concentration in the zigzag and armchair directions with the three strain ε for the p-type and n-type InSe at 300 K. For $\varepsilon = 0$, the maximum PF of the p-type (n-type) is 0.049 (0.041) W/K^{2}m at 300K in the armchair direction, which is consistent with the results of Section 4.3 [72]. For compressive strain, the PF of both the p- and n-type InSe has a maximum at $\varepsilon = -0.025$ because of the CMB effect. Although the LV → HV (in the p-type) and HV → LV (in the n-type) show different σ and S behaviors as shown in Fig. 4.5(a) and (b), respectively, both these types of the CMB give rise to a significant enhancement of the PF. We note that the PF of the n-type InSe reaches the maximum at the carrier concentration of about 4×10^{13} cm^{-2}, which can be experimentally accessible [30]. On the other hand, the maximum PF of p-type is difficult to achieve by experiment because of a relatively higher carrier concentration of 6×10^{14} cm^{-2}. Therefore, the selection of n-type InSe might be better than that of the p-type InSe to enhance the PF by the CMB. At $\varepsilon = -0.05$, the splitting of the degenerate LV and HV in p-type InSe leads to new energy band with the maximum energy of -1.7 eV at the Γ point as shown in Fig. 4.3. Since this energy band is almost flat at the Γ point (in other words, having heavy effective mass), S and the PF significantly increase at high carrier concentration of $\sim 10^{15}$ cm^{-2} (corresponding to the Fermi energy of -1.7 eV) for the p-type InSe as shown in Figs. 4.5(b) and 4.5(c), respectively. Although this concentration is even harder to dope.

4.4.2 Thermoelectric figure of merit

In Figs. 4.6(a)-(b), we plot the electronic thermal conductivity κ_{el} and the figure of merit ZT at 300 K as a function of strain ε and carrier concentration for both p-type and n-type InSe along zigzag and armchair directions, respectively. Here, we estimate ZT values by using a constant κ_{ph} of 27 W/mK [73]. In the case of $\varepsilon = 0$, the maximum ZT of the n-type (p-type) is 0.13 (0.21) at 300K in the armchair direction, which is better than other some other 2D materials, for example, monolayer $\mathrm{MoS_2}$ with $ZT \sim 0.1$ [81, 82]. Then, we further obtain an increased ZT by the CMB at the critical strain $\varepsilon = -0.025$. The optimum ZT value for the n-type InSe ($ZT = 0.41$) is enhanced by nearly 230 % of ZT at $\varepsilon = 0$, while the ZT is slightly enhanced by about 26 % of ZT at $\varepsilon = 0$ for the p-type InSe ($ZT = 0.25$), as shown in Fig. 4.6(b). At first sight, this result looks inconsistent with the optimum PF which shares a similar magnitude at $\varepsilon = -0.025$ for both p-type and n-type InSe [see Fig. 4.5(c)]. However, the different features for enhancement of the PF and ZT actually exist because there is an additional effect of the electronic thermal conductivity κ_{el} in ZT. The κ_{el} increases (or decreases) toward the CMB in the p-type (or n-type) InSe, as shown in Fig. 4.6(a). This behavior that κ_{el} is relevant to σ is known as the Wiedemann-Franz law $\kappa_{\mathrm{el}} = L\sigma T$, where L is the Lorentz number [41]. The ZT value of the n-type InSe is thus more improved than that of p-type InSe. Since the HV → LV gives rise not only to an enhanced PF, but also to a reduced κ_{el}, the HV → LV should be better than LV → HV to enhance ZT. It is important to note that the HV → LV often appears in many bulk thermoelectric materials such as PbTe, SnSe, and $\mathrm{Mg_2(Sn,Si)}$ due to the CMB [77, 78], which should be investigated in the future.

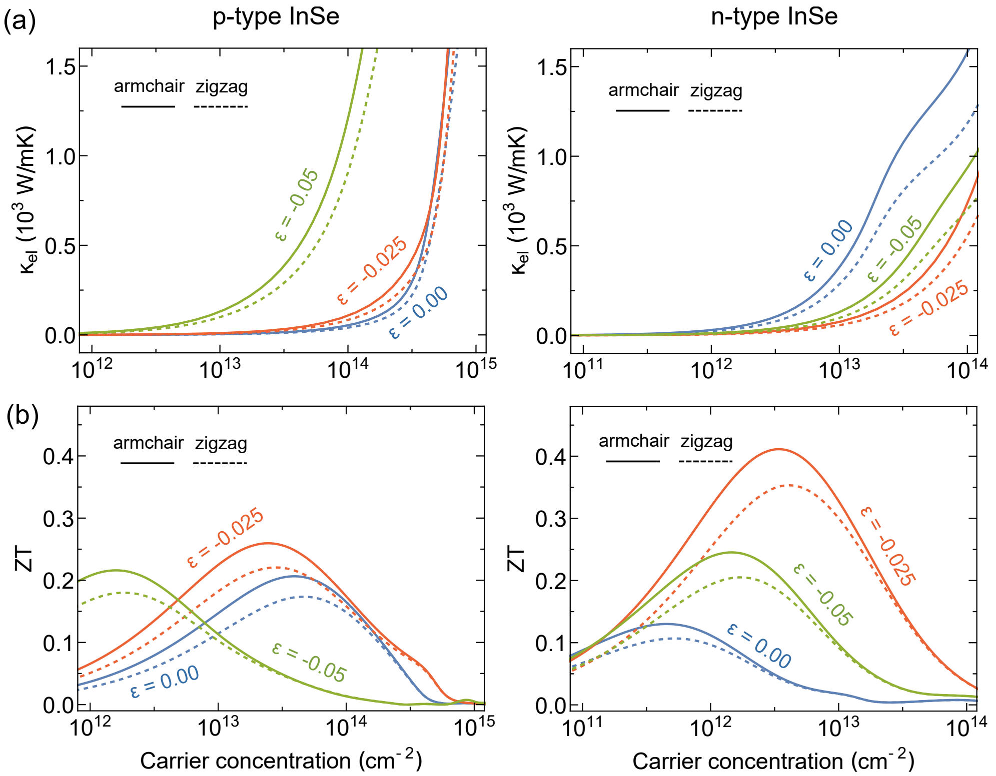

Figure 4.6 Electronic thermal conductivity κ_{el} and thermoelectric figure-of-merit ZT of p-type (a) and n-type (b) monolayer InSe as a function of strain ε and carrier concentration at 300 K. Solid and dashed lines denote armchair and zigzag directions, respectively.

In Figs. 4.7(a) and (b), we show the corresponding plots of optimum PF and ZT as function of ε at room temperature. Both the PF and ZT are enhanced with the compressive strain in the region from -0.02 to -0.03, which corresponds to the valley splitting energy ΔE from $4k_BT$ to $-4k_BT$ for $T = 300$ K (see Fig. 4.4). In addition, the maximum PF and ZT are found at the critical strain $\varepsilon = -0.025$ with $\Delta E \sim 0$ for both the p-and n-type InSe.

4.4.3 Additional analysis based on two-band model

Finally let us discuss the enhancement of PF for $|\Delta E| < 4k_BT$ by so-called two-band model [83]. In order to explain how the PF is enhanced with $|\Delta E| < 4k_BT$ and obtain the maximum value at $\Delta E \sim 0$, we use the analytical formula for the optimum PF

Fig. 4.6: Fig/chapter4-fig6.pdf
Fig. 4.7: Fig/chapter4-fig7.pdf

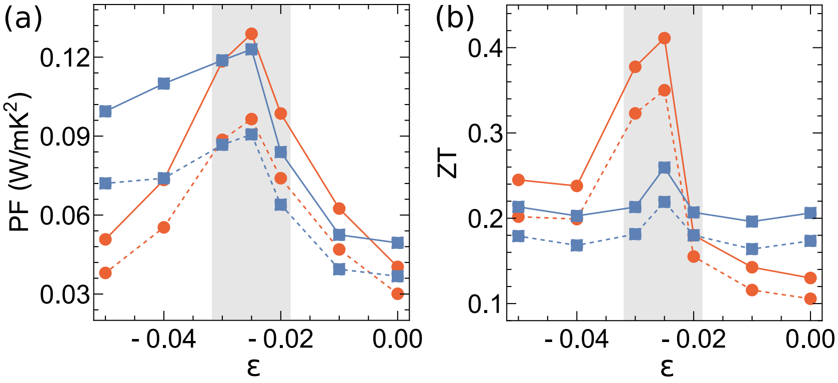

Figure 4.7 (a) Optimum PF and (b) optimum ZT are plotted as a function of strain ε at 300 K. In each panel, solid (dashed) lines denote the quantities along the armchair (zigzag) direction, while squares (circles) denote the p-type (n-type) InSe.

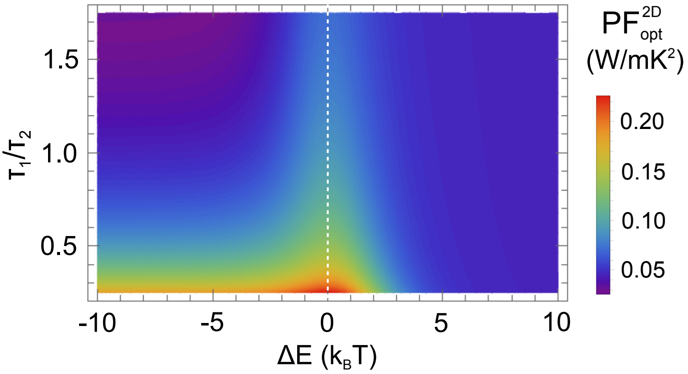

Figure 4.8 The dependence of optimum power factor $\mathrm{PF}_{\mathrm{opt}}^{\mathrm{2D}}$ on valley splitting energy ΔE, and on ratio of relaxation time coefficients between the two valleys τ_1/τ_2.

based on the two-band model (see Eq. (2.83) in Section 2.1.4.1) as

$$\mathrm{PF}_{\mathrm{opt}}^{\mathrm{2D}} = \frac{4k_B^3 T\Gamma(r+2)}{L\pi\hbar^2}\left(\tau_1 + \frac{\tau_2}{e^{\Delta E/k_\mathrm{B}T}}\right) e^{\left(r+\dfrac{\Delta E/k_\mathrm{B}T}{(\tau_1/\tau_2)e^{\Delta E/k_\mathrm{B}T}+1}\right)}, \tag{4.5}$$

where $\hbar$ is Planck's constant, L is the confinement length, $\Gamma(x)$ is the Gamma function, r is the characteristic exponent that determines the scattering mechanism, and τ_1 and τ_2 are the relaxation time coefficients of the valleys (1) and (2) (see Fig. 2.4 in Section 2.1.4), respectively.

In Fig. 4.8, we show a color plot of the $\mathrm{PF}_{\mathrm{opt}}^{\mathrm{2D}}$ as a function of ΔE and the ratio of τ_1/τ_2. In Fig. 4.8, we consider an arbitrary monolayer semiconductor with $L = 0.8$ nm, a fix value of $\tau_1 = 0.4$ ps at room temperature ($T = 300$ K), and $r = 0$ for the both valleys. Since the 2D DOS is constant as a function of energy for the quadratic

---

Fig. 4.8: Fig/chapter4-fig8.pdf

energy dispersion, we use $r = 0$ [Eq. (4.5)] for the scattering rate for both the valleys. For $\Delta E > 4k_{\mathrm{B}}T$, the $\mathrm{PF}^{\mathrm{2D}}_{\mathrm{opt}}$ is independent of both ΔE and τ_1/τ_2, in which the $\mathrm{PF}^{\mathrm{2D}}_{\mathrm{opt}}$ value is given by the valley (1), while for $\Delta E < -4k_{\mathrm{B}}T$, the $\mathrm{PF}^{\mathrm{2D}}_{\mathrm{opt}}$ is dominated by the valley (2). In the case of $\Delta E < -4k_{\mathrm{B}}T$, on the other hand, the $\mathrm{PF}^{\mathrm{2D}}_{\mathrm{opt}}$ increases with the decreasing τ_1/τ_2 because τ_1 is fixed. An interesting behavior of $\mathrm{PF}^{\mathrm{2D}}_{\mathrm{opt}}$ can be observed for $|\Delta E| < 4k_{\mathrm{B}}T$. Firstly, the $\mathrm{PF}^{\mathrm{2D}}_{\mathrm{opt}}$ increases with decreasing $|\Delta E|$ and shows a maximum value when ΔE approaches zero. Secondly, at the multivalley convergence point ($\Delta E = 0$), the $\mathrm{PF}^{\mathrm{2D}}_{\mathrm{opt}}$ increases with the decreasing τ_1/τ_2. It should also be noted that $1/\tau_i \propto \mathrm{DOS} = m_i/\pi\hbar^2$ $(i = 1, 2)$ [Eq. (4.5)], where m_i is the effective mass of the i-th valleys. Therefore, $m_1 \neq m_2$ when $\tau_1 \neq \tau_2$, which leads to an asymmetric PF in terms of ΔE when $\tau_1/\tau_2 \neq 1$ in Fig. 4.8. It is also clear from Eq. (4.5) and Fig. 4.8 that we need to obtain $\Delta E = 0$ to optimize the power factor, which could be tuned by the mechanical strain as shown in Fig. 4.4. This general behavior in the two-band model is thus consistent with the case of monolayer InSe as discussed in Section 4.4.2.

Chapter 5

Thermoelectric properties of two-dimensional tetradymites

In this Chapter, we show the thermoelectric properties of 2D tetradymites M_2X_3, in which M is the group V metal (Bi or Sb) and X is the group VI anion (Te, Se, or S), by using the Boltzmann transport formalism combined with the density functional theory (DFT) as a function of Fermi energy and crystal orientation. We find that their energy bands are characterized by small energy gaps, high group velocities, small effective masses, nonparabolic the Kane bands and multi-valleys convergences at near the center of the Brillouin zone, which are favorable for high power factor with the optimum power factor values can up to $0.20 - 0.25$ W/mK^2 at room temperature. Moreover, the 2D M_2X_3 are based on the heavy atomic masses and high polarizability of some chemical bonds, which lead to low phonon group velocities and anharmonic phonon behaviour that produce a very low intrinsic lattice thermal conductivity $\sim 1.5 - 2.0$ W/mK at room temperature. We show that by mixtures of M and X atoms, such as Bi_2Te_2Se, the power factor increases whereas the lattice thermal conductivity decreases. This approach leads to a high figure of merit of the p-type 2D Bi_2Te_2Se from 1.4 to 2.0 at operating temperature range of $300 - 500$ K. Our results thus offer significant applications for thermoelectric in next-generation vehicles.

5.1 Method and computational details

5.1.1 Transport properties of electron

In this work, the Seebeck coefficient S, electrical conductivity σ, and the electronic thermal conductivity κ_e along a certain direction are calculated from the linearized Boltzmann equation (BTE) for an electron with the relaxation time approximation

(RTA) as,

$$\sigma = q^2\mathcal{L}_0, \quad S = \frac{1}{qT}\frac{\mathcal{L}_1}{\mathcal{L}_0}, \quad \kappa_{\mathrm{e}} = \frac{1}{T}\left(\mathcal{L}_2 - \frac{\mathcal{L}_1^2}{\mathcal{L}_0}\right), \tag{5.1}$$

where q is the unit carrier charge, T is the temperature, and $\mathcal{L}_i$ is the transport integral that is defined by [38]

$$\mathcal{L}_i = -\frac{2}{N_{\mathbf{k}}V}\sum_{n\mathbf{k}} v_{n\mathbf{k}}^2 \tau_{n\mathbf{k}}^{\mathrm{e-ph}} \frac{\partial f_0}{\partial E}(E_{n\mathbf{k}} - E_F)^i, \ (i = 0, 1, 2), \tag{5.2}$$

where the factor 2 accounts for the spin degeneracy, $N_{\mathbf{k}}$ is the number of $\mathbf{k}$ points, V is the volume of system, E_F is the Fermi energy, $E_{n\mathbf{k}}$ is the electron energy at n-th band and the wavevector $\mathbf{k}$, $f_{n\mathbf{k}}$ is the Fermi-Dirac distribution function, $v_{n\mathbf{k}} = \nabla_{\mathbf{k}}E_{n\mathbf{k}}/\hbar$, where $\hbar$ is the Planck's constant, is the group velocity, and $\tau_{n\mathbf{k}}^{\mathrm{e-ph}}$ is the relaxation time due to the electron-phonon interaction. The relaxation time is given by the inverse of the scattering rate $\Gamma_{n\mathbf{k}}^{\mathrm{e-ph}}$ as $\tau_{n\mathbf{k}}^{\mathrm{e-ph}} = 1/\Gamma_{n\mathbf{k}}^{\mathrm{e-ph}}$. According to the Fermi golden rule, the scattering rate due to the e-ph interaction is given by [85]

$$\begin{aligned} \Gamma_{n\mathbf{k}}^{\mathrm{e-ph}} =& \frac{2\pi}{\hbar}\sum_{m\nu}\int \frac{d\mathbf{q}}{\Omega_{\mathrm{BZ}}} |g_{mn,\nu}(\mathbf{k},\mathbf{q})|^2 [(f_{m\mathbf{k}+\mathbf{q}} + n_{\nu\mathbf{q}})\delta(E_{n\mathbf{k}} - E_{m\mathbf{k}+\mathbf{q}} + \hbar\omega_{\nu\mathbf{q}}) \\ &+ (1 - f_{m\mathbf{k}+\mathbf{q}} + n_{\nu\mathbf{q}})\delta(E_{n\mathbf{k}} - E_{m\mathbf{k}+\mathbf{q}} - \hbar\omega_{\nu\mathbf{q}})], \end{aligned} \tag{5.3}$$

where $g_{mn,\nu}(\mathbf{k},\mathbf{q})$ is the electron-phonon matrix element, which is the transition of an electron from the n-th band and the wavevector $\mathbf{k}$ to the m-th band and the wavevector $\mathbf{k}+\mathbf{q}$ participated by a phonon with the ν-th mode and wave vector $-\mathbf{q}$, and $\omega_{p\mathbf{q}}$ and $n_{p\mathbf{q}}$ are the phonon frequency and the Bose-Einstein distribution function. The integral is taken over the Brillouin Zone (BZ) of volume Ω_{BZ}. The first and second terms in the brackets in Eq. (5.3) are related to the phonon-absorption and phonon-emission processes, respectively. We can evaluate the scattering rates in terms of the imaginary part of the self-energy by $\Gamma_{n\mathbf{k}}^{\mathrm{e-ph}} = (1/\hbar)\ \mathrm{Im}\sum_{n\mathbf{k}}^{\mathrm{e-ph}}$, because the occupation probability at the state $n\mathbf{k}$ will decay by the factor of $(\Delta t/\hbar)\mathrm{Im}\sum_{n\mathbf{k}}^{\mathrm{e-ph}}$ when an electron is added into a system after a time period Δt [84].

5.1.2 Transport properties of phonon

By using the Fourier law for the heat flux by phonons J, $J = -\kappa_{ph}\nabla T$, the phonon thermal conductivity along the direction of $\mathbf{q}$ is given by the linearized BTE for phonons with the RTA as follows

$$\kappa_{\mathrm{ph}} = \frac{1}{N_{\mathbf{q}}V}\sum_{\nu\mathbf{q}} \hbar\omega_{\nu\mathbf{q}} v_{\nu\mathbf{q}}^2 \tau_{\nu\mathbf{q}}^{\mathrm{ph-ph}} \frac{\partial n_{\nu\mathbf{q}}}{\partial T}, \tag{5.4}$$

where $N_{\mathbf{q}}$ is the number of $\mathbf{q}$ points, $v_{\nu\mathbf{q}}$ is the phonon group velocity for $\mathbf{q}$, and $\tau_{\nu\mathbf{q}}^{\mathrm{ph-ph}}$ is the relaxation time due to the ph-ph interaction. The phonon scattering rate (or spectral linewith), $\Gamma^{\mathrm{ph-ph}}_{\nu\mathbf{q}} = 1/\tau^{\mathrm{ph-ph}}_{\nu\mathbf{q}}$, is given by [85]

$$
\begin{aligned}
\Gamma^{\mathrm{ph-ph}}_{\nu\mathbf{q}} =& \frac{\hbar\pi}{4} \sum_{\nu'\nu''} \int \frac{d\mathbf{q}'}{\Omega_{\mathrm{BZ}}} [|V^{\nu\nu'\nu''}_{\mathbf{q}\mathbf{q}'_+\mathbf{q}''}|^2 (n_{\nu'\mathbf{q}'_+} - n_{\nu''\mathbf{q}''}) \delta(\hbar\omega_{\nu\mathbf{q}} - \hbar\omega_{\nu''\mathbf{q}''} + \hbar\omega_{\nu'\mathbf{q}'_+}) \\
&+ \frac{1}{2} |V^{\nu\nu'\nu''}_{\mathbf{q}\mathbf{q}'_-\mathbf{q}''}|^2 (n_{\nu'\mathbf{q}'_-} + n_{\nu''\mathbf{q}''} + 1) \delta(\hbar\omega_{\nu\mathbf{q}} - \hbar\omega_{\nu''\mathbf{q}''} + \hbar\omega_{\nu'\mathbf{q}'_-})], \qquad (5.5)
\end{aligned}
$$

where $V^{\nu\nu'\nu''}_{\mathbf{q}\mathbf{q}'_\pm\mathbf{q}''}$ are the phonon-phonon matrices for a three-phonon process satisfying the momentum conservation relation of $\mathbf{q} \pm \mathbf{q}' = \mathbf{q}'' + \mathbf{G}$, where $\mathbf{G}$ represents a reciprocal lattice vector. The three-phonon processes is called either the normal process when $\mathbf{G} = 0$ or the Umklapp process when $\mathbf{G} \neq 0$. The first term in the brackets in Eq. (5.5) is the transition possibility of the process that two phonons merge to create another phonon and the second term is vice versa.

5.1.3 Calculation details

In order to obtain the electron and phonon scattering rates of the e-ph and ph-ph interaction as shown by Eqs. (5.3) and (5.5), we used the Quantum ESPRESSO (QE) [62], EPW [86] and ShengBTE [87] packages. In which the EPW and the ShengBTE are used to calculate the electron-phonon and phonon-phonon interactions, respectively. A fully relativistic with norm-conserving pseudopotential using Perdew-Zunger parameterization [63] of exchange-correlation functional including local density approximation (LDA) is employed in QE. Anharmonic, interatomic force-constants (IFCs) are calculated by using $4 \times 4 \times 1$ supercells with only the Γ-point. The phonon-phonon interactions are considered up to the 6th nearest neighbors of the unit cell atoms for the anharmonic IFCs calculations.

5.2 Structural properties

Tetradymites have the formula M_2X_3, in which M is the group V metal (Bi or Sb) and X is the group VI anion (Te, Se or S). While Bi_2Se_3, Bi_2Te_3 and Sb_2Te_3 are common tetradymites, recently other stoichiometry of M and X atoms such as Bi_2Te_2Se and Bi_2Te_2S are synthesized as 2D materials [88]. In Fig. 5.1(a), we show the top and side views of a single quintuple-layers (QL) Bi_2Te_2Se as a example structure of 2D tetradymites. The 2D structure of the single-QL tetradymites is X1−M−X2−M−X1 stacked in the z direction of the unit cell. The X1 and X2 are two distinct types of the X sites, in which the X1 sites are located at the top or bottom of the layers and the X2 sites are in the middle. It is noted that the high-quality 2D tetradymites are recently obtained by a layer-by-layer growth in molecular beam epitaxy [89, 90]. The single-QL tetradymite is of great interest compared with a bulk (3D) tetradymites for thermoelectric applications when we consider the confinement effect [20]. Since the atomic mass of Bi is heavier than that of Sb, the thermal conductivity of Bi_2X_3

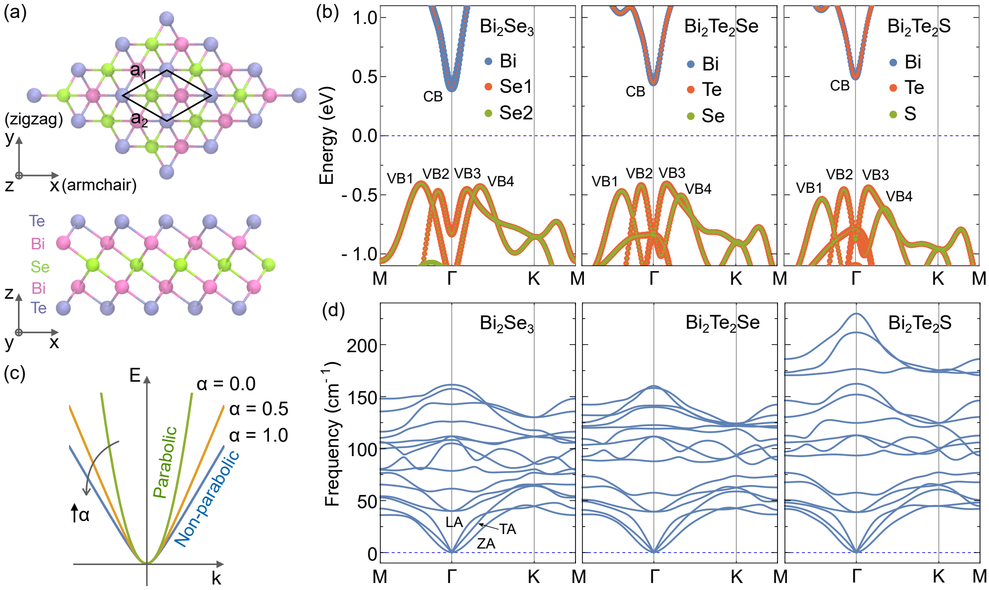

Figure 5.1 (a) Top and side views of single quintuple-layers (single-QL) Bi_2Te_2Se. Bi and Te, and Se atoms are represented by pink and green balls, respectively. The unit cell with the in-plane basis vectors a_1 and a_2 contains five atoms in five sublayers. The $x-$ and $y-$axes correspond to armchair and zigzag directions, respectively. (b) Electronic energy dispersions of single-QL Bi_2Te_2Se, Bi_2Te_2S, and Bi_2Se_3. The blue, red, and green dots represent the contributions of atomic orbital from the Bi, X1 (Te, Se), and X2 (Se, S) atoms, respectively. (c) Electronic dispersion of the Kane band due for $\alpha = 0.0, 0.5, 1.0$ and $m = m_e$. (d) Phonon dispersions of single-QL Bi_2Te_2Se, Bi_2Te_2S, and Bi_2Se_3.

Table 5.1: Calculated effective mass (m/m_e), band nonparabolicity (α), different energy (ΔE), and group velocities for LA (v_{LA}), TA (v_{TA}), and ZA (v_{ZA}) phonon modes.

Single-QL	m/m_e (kg)	α eV^{-1}	ΔE (eV)	v_{LA} (m/s)	v_{TA} (m/s)	v_{ZA} (m/s)
Bi_2Se_3	0.10	1.2	0.065	444	268	78
Bi_2Te_2Se	0.09	1.4	0.098	454	267	94
Bi_2Te_2S	0.09	1.5	0.173	480	281	89

is generally lower than that of Sb_2X_3 [91]. In this work, we consider the three 2D tetradymites based on Bi atom such as Bi_2Se_3, Bi_2Te_2Se, and Bi_2Te_2S.

5.3 Electronic and phonon properties

In Fig. 5.1(b), we show the energy dispersion of the single-QL Bi_2Se_3, Bi_2Te_2Se, and Bi_2Te_2S which have indirect band gaps are 0.81, 0.85, and 0.93 eV, respectively. As shown in Fig. 5.1(b), the conduction band (CB) of the single-QL M_2X_3 shows a non-

---

Fig. 5.1: Fig/chapter5-fig1.pdf

parabolic dispersion. The nonparabolic dispersion is modeled by the Kane band [41], in which the energy dispersion is given by $E(1+\alpha E) = \hbar^2\mathbf{k}^2/2m$, where m is the effective mass, and α is a parameter for describing the band nonparabolicity ($\alpha = 0$ corresponds to the parabolic band). In Fig. 5.1(c), we plot energy dispersion of the Kane band for $\alpha = 0.0, 0.5, 1.0$ and $m = m_{\mathrm{e}}$, where m_{e} is the mass of electron. For $\alpha E \gg 1$, we get a linear energy dispersion $E \sim \hbar|\mathbf{k}|/\sqrt{2m\alpha}$ while we have a parabolic band for smaller E such that $\alpha E < 1$ with the same α. The calculated m and α for the CBs of the single-QL $\mathrm{Bi_2Se_3}$, $\mathrm{Bi_2Te_2Se}$, and $\mathrm{Bi_2Te_2S}$ are listed in Table 5.1. For the common semiconductors such as Si and Ge, $\alpha = 0.50$ eV^{-1} and 0.65 eV^{-1} [41], respectively, are smaller than that of the single-QL $\mathrm{M_2X_3}$ ($\alpha = 1.2 - 1.5$ eV^{-1}).

The Kane band appears in many kinds of good thermoelectric materials such as PbTe, GeTe, and SnTe [92]. Recently, Liu et al. showed that nonparabolic band with the large α value is the cornerstone of the filtering effect of electron mean free path which improves thermoelectric properties [93]. Therefore, the n-type single-QL $\mathrm{M_2X_3}$ that have the large α ($1.2 - 1.5$ eV^{-1}) is expected to show a good thermoelectric properties. On the other hand, the valence bands (VBs) of the single-QL $\mathrm{M_2X_3}$ exhibit a convergence-of-multivalley energy bands, in which some distinct valleys become almost degenerate in energy. Accoding to the two-band model, we showed that the thermoelectric power factor can described as PF $\propto e^{-\Delta E/k_{\mathrm{B}}T}$ [83], where k_{B} is the Boltzmann constant ($k_{\mathrm{B}}T \sim 0.026$ eV at $T = 300$ K) and ΔE is the energy difference between the two energy extrema of valleys. In present study, ΔE is defined by the energy difference between the highest energy maxima and lowest energy maxima of the four valleys of the $\mathrm{M_2X_3}$ along $\Gamma - M$ and $\Gamma - K$ lines, which are denoted by VB1, VB2, VB3, and VB4 as shown in Fig. 5.1(b). The calculated ΔE for the VBs of the single-QL $\mathrm{Bi_2Se_3}$, $\mathrm{Bi_2Te_2Se}$, and $\mathrm{Bi_2Te_2S}$ are listed in Table 5.1. Since the VBs show a small ΔE within a few $k_{\mathrm{B}}T$, the p-type single-QL $\mathrm{M_2X_3}$ is also expected to have a large power factor.

It is important to note that the PF is very sensitive to ΔE value due to the exponential function $e^{-\Delta E/k_{\mathrm{B}}T}$, in which we get an optimize value at $\Delta E = 0$. Therefore, tuning the multi-valleys converging effect ($\Delta E = 0$) is an effective approach for increasing the PF, which is usually accomplished by chemical doping or strain engineering [77, 83]. Interestingly, in the single-QL $\mathrm{M_2X_3}$, the CB has the Bi character, whereas the VBs consist of the hybridized orbitals of X1 (Te, Se) and X2 (Se, S) atoms, as shown by colors in Fig. 5.1(b). Therefore, by mixing X1 with X2 atoms, we can tune the multi-valleys convergence for improving the PF in the 2D tetradymites. Since at least 10 $\mathrm{M_2X_3}$ compounds are either easily or potentially exfoliable in 2D tetradymite structures [94], we need to investigate all possible compounds for obtaining high thermoelectric performance 2D $\mathrm{M_2X_3}$ tetradymites. In the present study, for simplicity we focus on only the three 2D $\mathrm{Bi_2X_3}$ compounds. As show in Fig. 5.1(b), in $\mathrm{Bi_2Se_3}$ case, the energies of VB1 and VB4 are higher than those of VB2 and VB3.

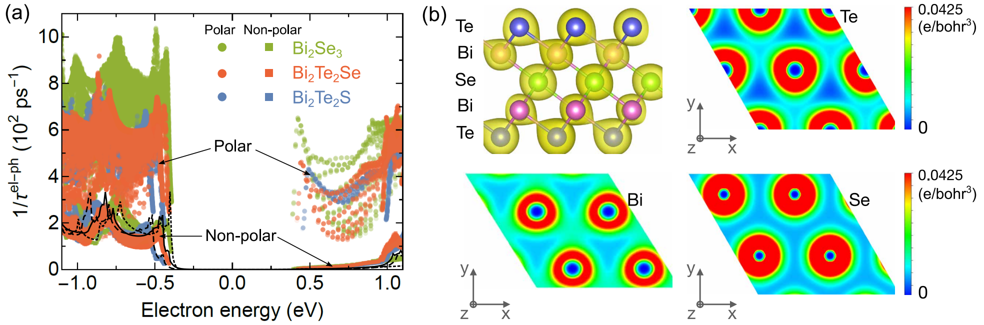

Figure 5.2 (a) Carrier scattering rate (inverse of relaxation time) of the single-QL M_2X_3 as a function of electron energy at 300K, for electrons and holes with energies within 1.5 eV of the band edges. Both the polar and non-polar cases due to all phonon modes are shown. The dot, solid, and dashed lines are the density of states of the single-QL Bi_2Se_3, Bi_2Te_2Se, and Bi_2Te_2S, respectively. (b) Electron charge density of the single-QL Bi_2Te_2Se in Bi, Te, and Se planes. The color scale is linear from blue to red as charge density increases in unit e/bohr^3.

When we change X1 from Se to Te atoms (Bi_2Te_2Se), the VB1 and VB4 decreases in energy, while the energies of VB2 and VB3 increases. In the case, we change X2 from Se to S atoms (Bi_2Te_2S), the VB1 and VB4 decrease further. In Fig. 5.1(d), we plot the phonon dispersion of single-QL Bi_2Se_3, Bi_2Te_2Se, and Bi_2Te_2S. No negative frequencies are observed in the first Brillouin zone, which confirms that all single-QL M_2X_3 structures are dynamically stable.

In Table 5.1, we list the group velocities of the acoustic branches near the Γ points including longitudinal (LA), in-plane transversal (TA), and out-of-plane (ZA) phonons. Since the group velocities of the acoustic phonon of 2D M_2X_3 are much smaller than that of other 2D material such as graphene and MoS_2. The single-QL M_2X_3 are thus expected to show a small thermal conductivity of lattice κ_{ph}, which leads to high ZT.

5.4 Electron transport

Let us characterize the transport coefficients quantitatively. In Fig. 5.2(a), we plot the calculated scattering rates of the single-QL M_2X_3 as a function of the energy for electrons and holes with energies within 1.5 eV of the band edges. For the case of non-polar materials, the scattering mechanisms include the electron-acoustic and the electron-optical-phonons. Further, the Fröhlich coupling due to the polar optical phonons is added to the plot by using Matthiessen's rule for the case of polar materials. In the case of non-polar materials, the scattering rate near the band edge follows the shape of the density of states (DOS) [41]. It is known that acoustic phonons give a dominant contribution to the scattering rate at room temperature. The electron-

---

Fig. 5.2: Fig/chapter5-fig2.pdf

phonon (el-ph) coupling matrix element for the acoustic phonon can be assumed as a constant, and thus we get $\tau^{-1} \propto$ DOS based on the Fermi golden rule for non-polar case [95]. However, in the case of polar materials, the electron-polar-optical-phonon coupling has a factor of $\epsilon_\infty^{-1} - \epsilon_0^{-1}$ that measures the strength of the phonon-induced dipole field in terms of the magnitude of dielectric constants [41], in which ϵ_∞ and ϵ_0 are dielectric constants of the high- and low-frequency, respectively. Since the best thermoelectric material is achieved for the heavily doped region where the polar scattering is sufficiently screened, that is ϵ_0 is usually larger than ϵ_∞ [96], in particular for the case of 2D material [72]. Therefore, the scattering rate no longer follow the DOS shape in the case of polar materials as shown in Fig. 5.2(a).

According to the Lyddane-Sachs-Teller relation $\sqrt{\epsilon_0/\epsilon_\infty} = \omega_\mathrm{L}/\omega_\mathrm{T}$ [97], where ω_L and ω_T are the frequencies of the longitudinal (LO) and transversal optical (TO) phonon modes, respectively, a large contribution to the factor $\epsilon_\infty^{-1} - \epsilon_0^{-1}$ comes from phonons near the energy separation about 50 cm^{-1} between LO and TO phonons [see Fig. 5.1(d)]. Since the Te atoms have a large charge density compared with the Bi atoms [see Fig. 5.2(b)], resulting in a motion of Te atoms in longitudinal and/or transverse modes which is the origin of the large polar scattering. By considering the polar scattering, the magnitude of the scattering rates increases 8 times and 4 times for the electrons and holes, respectivety, compared with the case of non-polar materials as shown in Fig. 5.2(a). Although the polar scattering will reduce the electrical conductivity due to the Matthiessen's rule, the polarizability of surface bonds will reduce the lattice thermal conductivity because of the high anharmonicity [98].

5.5 Thermoelectric power factor

With the energy-dependent scattering rates, we obtain the Seebeck coefficient S, electrical conductivity σ, and thermoelectric power factor PF by solving the Boltzmann transport equation. In Figs. 5.3a and 5.3b we plot these thermoelectric properties as function of carrier concentration at 300 K and 500 K for both n-type and p-type single-QL $\mathrm{M_2X_3}$, respectively. σ increases monotonically with increasing the carrier concentration, while S is approximately linear to the carrier concentration in the range $10^{11} - 10^{13}$ cm^{-2} and $10^{13} - 10^{15}$ cm^{-2} for the n-type and p-type single-QL $\mathrm{M_2X_3}$, respectively. Let us consider the carrier concentration at 10^{13} cm^{-2}, σ of the n-type $\mathrm{M_2X_3}$ is higher than that of the p-type $\mathrm{M_2X_3}$. This because the n-type $\mathrm{M_2X_3}$ have the Kane band ($\alpha \sim 1.2 - 1.5$) and thus a extremely small effective mass $\sim 0.1 m_e$ (m_e is the mass of electron), which implies a high electrical conductivity if we adopt the Drude model as $\sigma \propto ne^2\tau/m$, where n is the carrier concentration. However, due to the multi-valleys convergence $|S| \propto N_v^{2/3} m$, where N_v is number of the degenerate band valleys, the absolute value of S of the n-type $\mathrm{M_2X_3}$ is smaller than that of the p-type $\mathrm{M_2X_3}$. Since PF $= S^2\sigma$, increasing $|S|$ value is more contributing to improve

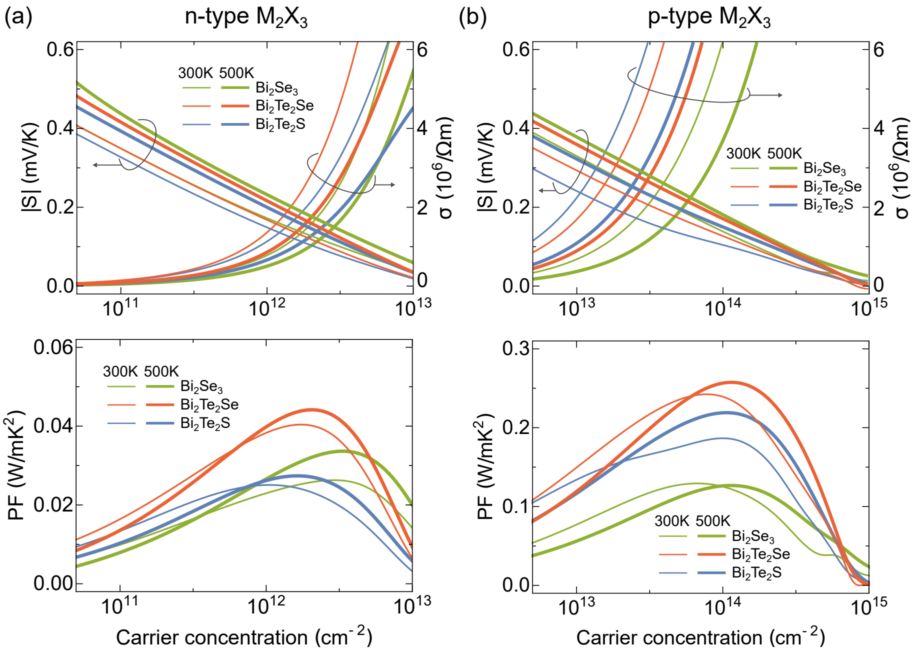

Figure 5.3 Seebeck coefficient S, electrical conductivity σ (top), and thermoelectric power factor PF (bottom) of the n-type (a) and p-type (b) single-QL M_2X_3 as a function of carrier concentration at 300 K (thin lines) and 500 K (thick lines).

the PF compared with increasing σ. Therefore, the PF of the p-type M_2X_3 is much higher than that of the n-type M_2X_3, as shown in Fig. 5.3. The maximum PF values for the n-type (0.045 W/mK^2) and p-type (0.26 W/mK^2) are found in the single-QL Bi_2Te_2Se at 500 K. The PF of the p-type 2D Bi_2Se_3 at 300 K (0.125 W/mK^2) is much higher than that of the p-type bulk Bi_2Se_3 (0.0018 W/mK^2 [99]) due to the quantum confinement effect [1, 20]. We note that the optimum carrier concentration at 5×10^{12} cm^{-2} and 10^{14} cm^{-2} for the n-type and p-type M_2X_3, respectively, can be accessible experimentally by doping [100].

5.6 Lattice thermal conductivity

Finally let us discuss thermal conductivity. The total thermal conductivity is defined $\kappa = \kappa_{\mathrm{e}} + \kappa_{\mathrm{ph}}$, where κ_{e} is the electronic thermal conductivity and κ_{e} is obtained from Eqs. 5.1 and 5.2 as shown in Fig. 5.5, while κ_{ph} is the lattice (or phonon) thermal conductivity. In Fig. 5.4(a) and (b), we plot κ_{ph} [Eq. (5.4)] and $1/\tau_{\mathrm{ph-ph}}$ [Eq. (5.5)] as a function of temperature and the phonon frequency. As expected for the heavy M and X atoms in the M_2X_3, the intrinsic phonon properties of the single-QL M_2X_3 produce a very low κ_{ph} as shown in Fig. 5.4a. At room temperature, $\kappa_{\mathrm{ph}} = 1.4$, 1.3,

---

Fig. 5.3: Fig/chapter5-fig3.pdf

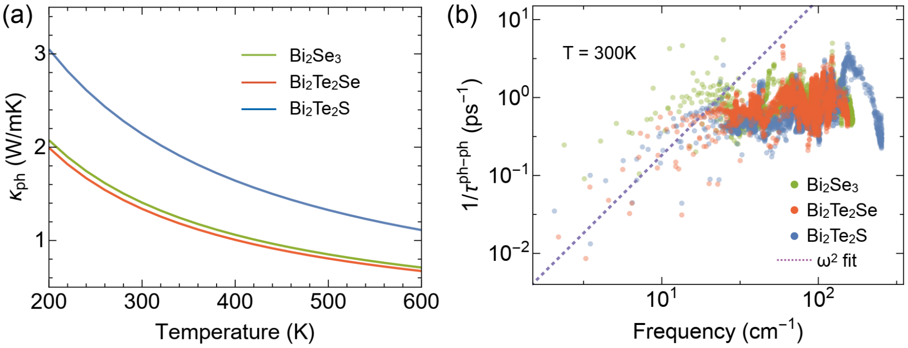

Figure 5.4 (a) Lattice thermal conductivity of the single-QL M_2X_3 as function of temperature. (b) Phonon-phonon scattering rate of the single-QL M_2X_3 as function of frequency of the phonon dispersion relations on a logarithmic scale. Dashed purple line is the fits to the scattering rates describing the ω^2 behaviors of the anharmonic in the low-frequency regime.

and 2.1 W/mK for the single-QL Bi_2Se_3, Bi_2Te_3Se, and Bi_2Te_3S, respectively. The in-plane thermal conductivity of the single-QL Bi_2Se_3 in this calculation is in a good agreement with the experimental data for Bi_2Se_3 (~ 1 W/mK) [101]. There are two main reasons for the intrinsic low value of $\kappa_{\text{ph}} \propto v^2\tau^{\text{ph-ph}}$. First, since Bi, Sb, Te and Se are one of the heaviest atoms in the periodic table, their chemical bonds are relatively weak (see Fig. 5.2b), resulting in low sound velocities v_{LA}, v_{TA}, and v_{ZA} (see Table 1). Second reason is that the strong effect of anharmonic scattering of phonon is seen in Fig. 5.4b by the calculation of $1/\tau^{\text{ph-ph}}$. Hellman et al. [101] showed that the phonons with low-frequency $\omega < 50$ cm^{-1} carry 60% of the total heat at room temperature in Bi_2Te_3, which are extremely affected by the anharmonic scattering. As seen in the log-log plot of Fig. 5.4(b), the acoustic scattering rates exhibit inversely proportional to the square of frequency ($1/\tau^{\text{ph-ph}} \propto \omega^2$) in the low-frequency region, which is in a good agreement with Klemens's prediction [102].

5.7 Thermoelectric figure of merit

In Fig. 5.6(a) and (b), we plot the thermoelectric figure of merit ZT for the n-type and p-type single-QL M_2X_3, respectively, as a function of carrier concentration at 300 K and 500 K for each figure. ZT is obtained by using S, σ, κ_e, and κ_{ph} that are calculated by the DFT calculations, in which the electron-phonon and phonon-phonon interactions are considered for σ and κ_{ph}. Since the p-type single-QL M_2X_3 have a high power factor due to the multi-valleys convergence and a intrinsic low thermal conductivity, ZT of the p-type single-QL M_2X_3 is much higher than that of the n-type single-QL M_2X_3 as shown in Fig. 5.6. The maximum ZT is found in the p-type single-QL Bi_2Te_2Se from 1.4 to 2.0 at operating temperature range from 300 K to 500

Fig. 5.4: Fig/chapter5-fig4.pdf

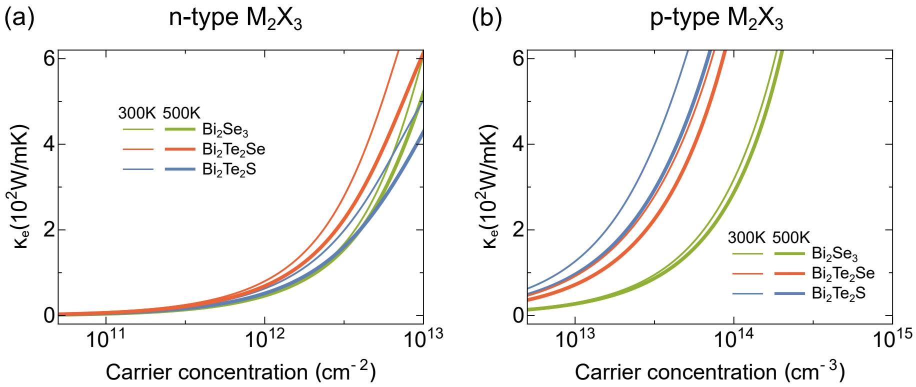

Figure 5.5 Electronic thermal conductivity of the n-type (a) and p-type (b) single-QL M_2X_3 as a function of carrier concentration at 300 K (thin lines) and 500 K (thick lines).

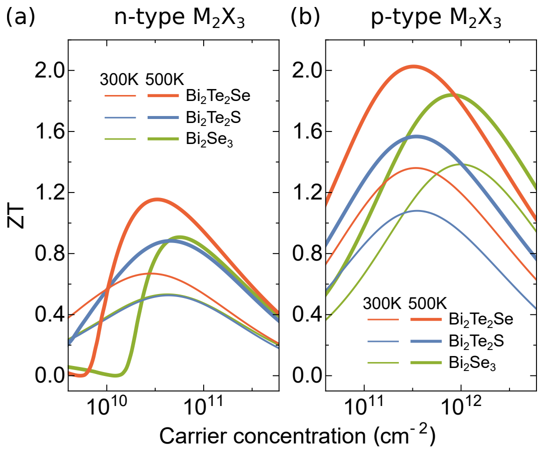

Figure 5.6 Figure of merits *ZT* of the n-type (a) and p-type (b) single-QL M_2X_3 as a function of carrier concentration at 300 K (thin lines) and 500 K (thick lines).

K, which implies that Bi_2Te_2Se is a best TE material design for the 2D tetradymite materials. The optimized carrier concentrations for the maximum ZT at 500 K are 5×10^{10} and 5×10^{11} cm^{-2} for the n-type and p-type single-QL Bi_2Te_2Se, respectively, which are two order of magnitude lower than those for the PF and are much easier to achieve. We note that the single-QL Bi_2Te_2Se also shows a high ZT value for hole doping case (n-type) with $ZT = 1.2$ at 500 K. The material with the high ZT values for both hole (n-type) and electron (p-type) doping is very important for fabricating TE devices. Therefore, the 2D Bi_2Te_2Se is very promising low-dimensional materials of TE device operating at room temperature.

Fig. 5.5: Fig/chapter5-fig6.pdf
Fig. 5.6: Fig/chapter5-fig6.pdf

Chapter 6

ZT Universal curve of thermoelectric ZT for semiconductors

In this chaper, we will discuss a *new* parameter α, which provides a way to optimize thermoelectric performance, that is independent of shape and dimension of the materials. First in Section 6.1 we obtain an analytical formula for thermoelectric figures of merit (ZT) and power factor (PF) are derived based on the one-band model. We find that there is a direct relationship between the optimum ZT and the optimum PF of semiconductors, even though the two optimum quantities are generally given at different values of chemical potentials. In Section 6.2, we show example for the optimum ZT and optimum PF as a function of the chemical potential. In Section 6.3, by introducing the dimensionless parameter α consisting of the optimum PF and lattice thermal conductivity (without electronic thermal conductivity), it is possible to unify optimum ZT of both bulk and low-dimensional semiconductors into a single universal curve as a function of α that covers many materials with different dimensionalities.

6.1 Power factor and figure of merit for semiconductor

We will start already derived formulas of thermoelectric properties by the conventional Boltzmann transport theory. From Eqs. (2.23)-(2.25), the PF and ZT can be written as

$$\mathrm{PF} = S^2\sigma = \frac{1}{T^2}\frac{\mathcal{L}_1^2}{\mathcal{L}_0}, \tag{6.1}$$

$$ZT = \frac{S^2\sigma}{\kappa_\mathrm{e} + \kappa_\mathrm{l}}T = \beta\frac{\mathcal{L}_1^2}{\mathcal{L}_0\mathcal{L}_2 - \mathcal{L}_1^2}, \tag{6.2}$$

where κ_l is the lattice thermal conductivity and $\beta = 1/(\kappa_\mathrm{l}/\kappa_\mathrm{e}+1) \leq 1$ and $\mathcal{L}_i$ $i = 0, 1, 2$ is the transport integral that is defined by [Eq. (2.21)]

$$\mathcal{L}_i = \int \mathcal{T}(E)(E - E_\mathrm{F})^i \left(-\frac{\partial f_0}{\partial E}\right) \mathrm{d}E,\ i = 0, 1, 2, \tag{6.3}$$

where ther Fermi energy E_F is defined as the chemical potential measured from the bottom (top) of the conduction (valence) energy band in an n-type (p-type) semiconductor, and $\mathcal{T}(E)$ is the transport distribute function that is defined as [Eqs. (2.22)]

$$\mathcal{T}(E) = v_x^2(E)\tau(E)\mathcal{D}(E), \tag{6.4}$$

where $v_x(E)$, $\tau(E)$, and $\mathcal{D}(E)$ are the group velocity in the x direction, the relaxation time, and the density of states (DOS) of the carrier, respectively. It is clear from Eqs. (6.1) and (6.2) that the PF and ZT have different dependence on E_F.

For the sake of simplicity, we consider a single parabolic band, in which the energy band structure and the group velocity can be given as $E(\mathbf{k}) = \hbar^2\mathbf{k}^2/2m$ and $v(\mathbf{k}) = \frac{1}{\hbar}[\partial E(\mathbf{k})/\partial\mathbf{k}] = \hbar\mathbf{k}/m$, respectively, where $\mathbf{k}$ is the wave vector of the carrier, m is effective mass of the carrier, and $\hbar$ is the Planck constant. We assumed that the material is isotropic with a dimension $d = 1, 2, 3$, the group velocity in the direction of x, $v_x^2(E) = v^2(\mathbf{k})/d = \hbar^2\mathbf{k}^2/m^2 d = 2E/md$, and the relaxation time of the carrier is inversely proportional to the DOS, $\tau(E) = C\mathcal{D}^{-1}(E)$, where C is the scattering coefficient in units of $\mathrm{W}^{-1}\mathrm{m}^{-3}$ [see Eq. (2.67)]. The DOS is defined as $\mathcal{D}(E) = \frac{2}{\Omega}\sum_\mathbf{k}\delta[E - E(\mathbf{k})]$ in units of $\mathrm{J}^{-1}\mathrm{m}^{-3}$, where the factor 2 accounts for the spin degeneracy and Ω is the volume of the system. The calculation of C for a typical material are given in Section 2.1.3.2. After substituting $v_x^2(E)$ and $\tau(E)$ into $\mathcal{T}(E)$ in Eq. (6.4), the integrals $\mathcal{L}_i$ in Eq. (6.3) can be written as

$$\mathcal{L}_0 = \frac{2C}{md}(k_\mathrm{B}T)F_0, \tag{6.5}$$

$$\mathcal{L}_1 = \frac{2C}{md}(k_\mathrm{B}T)^2(2F_1 - \eta F_0), \tag{6.6}$$

$$\mathcal{L}_2 = \frac{2C}{md}(k_\mathrm{B}T)^3(3F_2 - 4\eta F_1 + \eta^2 F_0), \tag{6.7}$$

where $\eta = E_\mathrm{F}/k_\mathrm{B}T$ is the reduced (or dimensionless) chemical potential and $F_j(\eta) = \int \eta^j f_0 \mathrm{d}\eta$ is the Fermi-Dirac integral. By substituting $\mathcal{L}_i$ in Eqs. (6.5), (6.6), and (6.7) into Eqs. (6.1) and (6.2), we obtain the formulas of the PF and ZT as follows:

$$\mathrm{PF} = \frac{2Ck_\mathrm{B}^3 T}{md}\frac{(2F_1 - \eta F_0)^2}{F_0}, \tag{6.8}$$

$$ZT = \beta\frac{(2F_1 - \eta F_0)^2}{F_0(3F_2 - 4\eta F_1 + \eta^2 F_0) - (2F_1 - \eta F_0)^2}, \tag{6.9}$$

where the integrals F_0, F_1, and F_2 are calculated numerically.

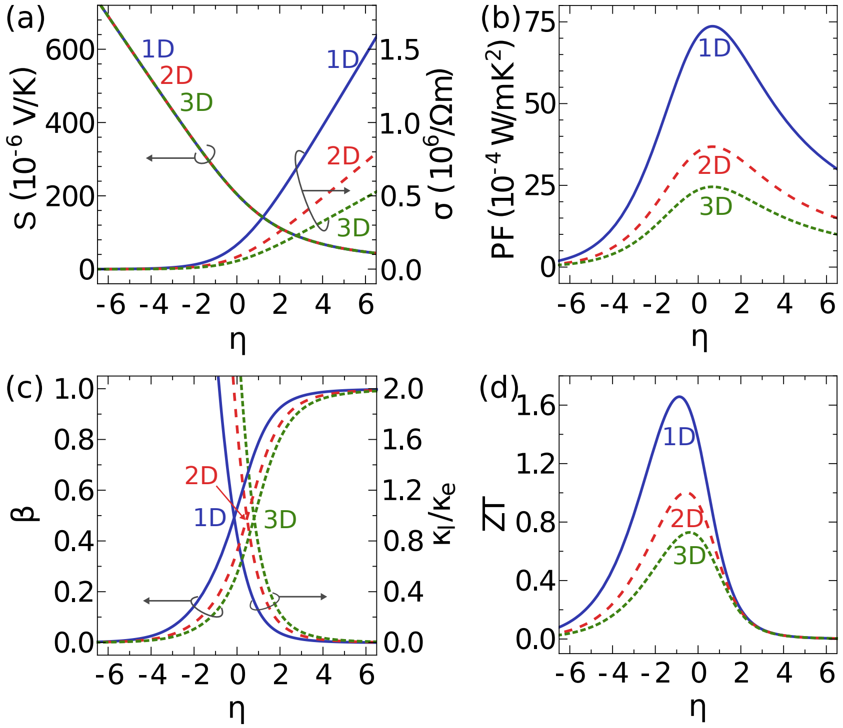

Figure 6.1 (a) S and σ, (b) PF, (c) β and κ_l/κ_e, and (d) ZT as a function of the reduced chemical potential η for the 1D, 2D, and 3D systems, respectively. The carrier effective mass, the carrier mobility, and the lattice thermal conductivity are set to be $m = 1.12m_0$, $\mu = 173$ cm^2/Vs, and $\kappa_l = 0.728$ W/mK, respectively, for n-type $\mathrm{Bi_2Te_{2.7}Se_{0.3}}$ at room temperature ($T = 298$ K) [42].

6.2 Example of a typical material

Using the definition if Eqs. (6.8) and (6.9) in Section 6.1, let us will discuss an example of calculating the PF and ZT as a function of η for one semiconducting material. In Fig. 6.1, we plot the dependence of (a) S and σ, (b) the PF [Eq. (6.8)], (c) β and κ_l/κ_e, and (d) ZT [Eq. (6.9)] on the reduced chemical potential η for $d = 1, 2, 3$. When plotting Figs 6.1(a)-(d), we consider a typical semiconductor, n-type $\mathrm{Bi_2Te_{2.7}Se_{0.3}}$, at $T = 298$ K with the doping concentration of 0.92×10^{19} cm^{-3}. The effective mass, and mobility of carrier, lattice thermal conductivity are taken to be $m = 1.12m_0$, $\mu = 173$ cm^2/Vs, and $\kappa_l = 0.728$ W/mK, respectively, for the 3D ($d = 3$) bulk n-type $\mathrm{Bi_2Te_{2.7}Se_{0.3}}$ [42]. The scattering coefficient $C = 1.18 \times 10^{33}$ W^{-1}m^{-3} is obtained from m and μ by using Eq. (2.67) in Section 2.1.3.2, which leads to an average relaxation time of about 0.1 ps. We simply adopted the same parameter values of m, κ_{l}, and C for the 1D ($d = 1$) and 2D ($d = 2$) systems as the 3D's. However, these parameters

---

Fig. 6.1: Fig/chapter6-fig1.pdf

are generally different for different d, as we adopt later in Section 6.3. As shown in Figure 6.1(a), S is independent of d and S increases with decreasing η, while σ depends on d and σ decreases with decreasing η. This behavior can be understood in terms of their units since the units [V/K] of S show no dependence of length scale, while the unit [$1/\Omega$m] of σ show dependence of length scale. In Figure 6.1(b), we can see a strong enhancement of the maximum PF around $\eta \approx 0$ in the low-dimensional systems (1D and 2D). For the bulk (3D) system, the theoretical maximum PF value is about 0.0025 W/mK^2, which is in a good agreement with the experimental data of about 0.0021 W/mK^2 [42]. In the case of $\eta \gg 0$, we can see that S decreases to zero because the system becomes metallic at high doping concentrations, while σ is close to zero when $\eta \ll 0$ as shown in Fig. 6.1(a). Therefore, the PF$_{opt}$ occurs at $\eta \approx 0$, in which E_{F} lies at the bottom (top) of conduction (valence) energy band of the p-type (n-type) semiconductor, for all the 1D, 2D, and 3D systems, as shown in Fig. 6.1(b). In Figure 6.1(d), we also obtain a strong enhancement of the maximum ZT values in the 1D and 2D systems, which is known to be the confinement effect or the Hicks-Dresselhaus theory [1, 2]. For the 3D system, the theoretical maximum ZT value is about 0.72, which is in a good agreement with the experimental data of about 0.73 [42]. In the case of $\eta \gg 0$, the coefficient $\beta = 1/(\kappa_{\mathrm{l}}/\kappa_{\mathrm{e}} + 1) \approx 1$ since κ_{e} is much larger than κ_{l} when the system is metallic, as shown in Fig. 6.1(c). In contrast, $\beta \approx 0$ when $\eta \ll 0$ because k_e is near zero (few free electron carriers in the insulators) [see Fig. 6.1(c)]. Therefore, ZT_{opt} is found at $\eta < 0$, in which E_{F} lies in the energy gap, as shown in Fig. 6.1(d). Important information in Figs. 6.1(b) and (d) is that the PF and ZT are optimized at not the same point but of $\eta \approx 0$ and $\eta < 0$, respectively, for all 1D, 2D, and 3D systems.

6.3 Nondegenerate semiconductor approximation

Next, we would like to obtain the analytical formulas for both the PF$_{\mathrm{opt}}$ and ZT_{opt}. In Eqs. (6.8) and (6.9), that we use to plot Figs. 6.1(b) and 6.1(d), we calculate the Fermi-Dirac integrals F_0, F_1, and F_2 numerically. The problem is how we can get analytical formulas for PF$_{\mathrm{opt}}$ and ZT_{opt}. Since the PF$_{\mathrm{opt}}$ (ZT_{opt}) is optimized at $\eta \approx 0$ ($\eta < 0$), we can use the approximation for nondegenerate semiconductor that is especially valid for $\eta \leq 0$ [75]. In this approximation, the Fermi-Dirac integral can be approximated as $F_j(\eta) \approx e^{\eta}\Gamma(j+1)$ [75], where $\Gamma(j)$ is the Gamma function. By substituting $F_0 = e^{\eta}$, $F_1 = e^{\eta}$, and $F_2 = 2e^{\eta}$ into Eq. (6.8), we get the PF formula as

$$\mathrm{PF} = \frac{2Ck_{\mathrm{B}}^3 T}{md}(2-\eta)^2 e^{\eta}. \tag{6.10}$$

Since $\kappa_{\mathrm{e}} = \frac{1}{T}(\mathcal{L}_2 - \mathcal{L}_1^2/\mathcal{L}_0) = 4Ck_{\mathrm{B}}^3 T^2 e^{\eta}/(md)$ [see Eq. (2.25)], β in Eq. (6.2) can be written as

$$\beta = \frac{1}{[2/(\alpha e^{\eta})] + 1}, \tag{6.11}$$

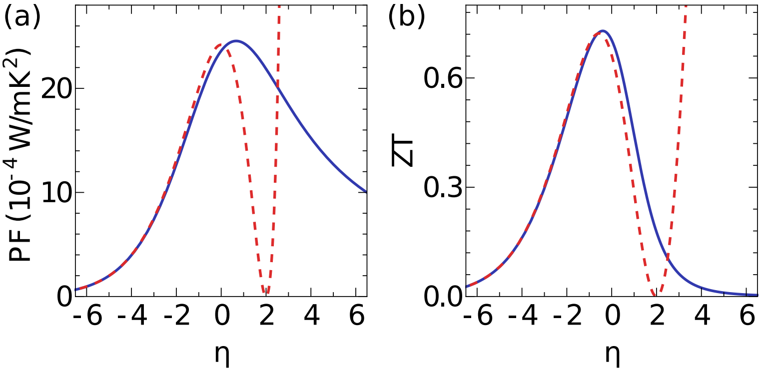

Figure 6.2 (a) PF and (b) ZT as functions of the reduced chemical potential η. Results from the formulas involving numerical integrations and those from analytical calculation (the approximation for nondegenerate semiconductor) are represented by solid and dashed lines, respectively. The carrier effective mass, the carrier mobility, and the lattice thermal conductivity are set to be $m = 1.12m_0$, $\mu = 173$ cm^2/Vs, and $\kappa_{\rm l} = 0.728$ W/mK, respectively, for 3D n-type $\rm Bi_2Te_{2.7}Se_{0.3}$ at room temperature [42].

where α is a dimensionless parameter as follows

$$\alpha = \frac{8Ck_{\rm B}^3T^2}{md\kappa_{\rm l}}. \tag{6.12}$$

Substituting β of Eq. (6.11) into Eq. (6.9) and applying the approximation of F_j, we obtain for ZT as

$$ZT = \frac{(2-\eta)^2}{[4/(\alpha e^{\eta})] + 2}. \tag{6.13}$$

In Figs. 6.2(a) and 6.2(b), we respectively show $\rm PF_{opt}$ and $ZT_{\rm opt}$ that are calculated by numerical calculation of the Fermi-Dirac integrals (solid lines) [Eqs. (6.8) and (6.9)] and the approximation for nondegenerate semiconductor (dashed lines) [Eqs. (6.10) and (6.13)]. If we see the *values* of $\rm PF_{opt}$ and $ZT_{\rm opt}$ (local maxima of PF and ZT) at $\eta \leq 0$ in Fig. 6.2, we can see that the analytical formulas based on the approximation for nondegenerate semiconductor can nicely reproduce the $\rm PF_{opt}$ and $ZT_{\rm opt}$ by numerical calculation. In particular, we can see that the both results have almost the same maximum value at the same η for both PF and ZT. Therefore, we can determine the $\rm PF_{opt}$ and $ZT_{\rm opt}$ from Eqs. (6.10) and (6.13) by analytically solving d(PF)/d$\eta = 0$ and d(ZT)/d$\eta = 0$, respectively. By solving this we obtain $\rm PF_{opt}$ and $ZT_{\rm opt}$ as follows

$$\mathrm{PF}_{\rm opt} = \frac{8Ck_{\rm B}^3T}{md}, \quad ZT_{\rm opt} = \frac{W_0^2(\alpha)}{2} + W_0(\alpha), \tag{6.14}$$

where $W_0(\alpha)$ is the principal branch of so-called the Lambert W function (see Appendix B). By substituting the $\rm PF_{opt}$ in Eq. (6.14) into Eq. (6.12), the α parameter is

---

Fig. 6.2: Fig/chapter6-fig2.pdf

now expressed in terms of the $\mathrm{PF}_{\mathrm{opt}}$ and κ_{l},

$$\alpha = \frac{\mathrm{PF}_{\mathrm{opt}}}{\kappa_{\mathrm{l}}} T. \tag{6.15}$$

The corresponding reduced chemical potentials for the $\mathrm{PF}_{\mathrm{opt}}$ and ZT_{opt} are $\eta_{\mathrm{opt}}^{\mathrm{PF}} = 0$ and $\eta_{\mathrm{opt}}^{ZT} = -W_0(\alpha)$, respectively [see Fig. 6.2]. Based on the simple analytical formulas in Eq. (6.14), the values of the $\mathrm{PF}_{\mathrm{opt}}$ and ZT_{opt} can be calculated directly from C, d, m, κ_{l}, and T, which could be measured in experiments. For example, in the case of 3D n-type $\mathrm{Bi_2Te_{2.7}Se_{0.3}}$ at room temperature, taken from Ref. [42], we have $C = 1.18 \times 10^{33}\ \mathrm{W^{-1}m^{-3}}$ (see also Section 2.1.3.2), $d = 3$, $m = 1.12 m_0$, $\kappa_{\mathrm{l}} = 0.728$ W/mK, and hence $\mathrm{PF}_{\mathrm{opt}} = 0.0024\ \mathrm{W/mK^2}$ and $ZT_{\mathrm{opt}} = 0.72$. This analytical result agrees well with both fully numerical calculation ($\mathrm{PF}_{\mathrm{opt}} = 0.0025\ \mathrm{W/mK^2}$ and $ZT_{\mathrm{opt}} = 0.72$) [see Fig. 6.2] and experimental data ($\mathrm{PF}_{\mathrm{opt}} = 0.0021\ \mathrm{W/mK^2}$ and $ZT_{\mathrm{opt}} = 0.73$) [42].

To gain insight into the $\mathrm{PF}_{\mathrm{opt}}$, we can substitute the coefficient C in Eq. (2.67) from Section 2.1.3.2 to the $\mathrm{PF}_{\mathrm{opt}}$ formula in Eq. (6.14), so that the $\mathrm{PF}_{\mathrm{opt}}$ is given by

$$\mathrm{PF}_{\mathrm{opt}} = \frac{16 \mu k_{\mathrm{B}}^2}{q L^3} \left(\frac{L}{\Lambda}\right)^d \frac{\Gamma\left(\frac{5}{2}\right)}{\Gamma\left(\frac{7-d}{2}\right) \Gamma\left(\frac{d}{2}\right)}, \tag{6.16}$$

where L is the confinement length for a particular material dimension, and $\Lambda = [2\pi\hbar^2/(m k_{\mathrm{B}} T)]^{1/2}$ is the thermal de Broglie wavelength (see Chapter 3). Equation (6.16) shows the dependence of the $\mathrm{PF}_{\mathrm{opt}}$ on μ, d, L, and Λ. By scaling the $\mathrm{PF}_{\mathrm{opt}}$ with the optimum PF of a 3D system, i.e. $\mathrm{PF}_{\mathrm{opt}}^{\mathrm{3D}}$, we find that the ratio $\mathrm{PF}_{\mathrm{opt}}/\mathrm{PF}_{\mathrm{opt}}^{\mathrm{3D}}$ merely depends on the factor $(L/\Lambda)^{d-3}$, consistent with our results in Chapter 3. It is clear that the $\mathrm{PF}_{\mathrm{opt}}$ is enhanced for 1D and 2D semiconductors only when L is smaller than Λ. Interestingly, in this present study, we find that by defining $\alpha = (\mathrm{PF}_{\mathrm{opt}}/\kappa_{\mathrm{l}})T$, we can obtain ZT_{opt} from PF_{opt} through Eq. (6.14). Note that $W_0(\alpha)$ monotonically increases with α but a slightly saturated behavior with increasing α, as shown in Fig. B.1 in Appendix B. Now we understand that the factor $(L/\Lambda)^{d-3}$ is not only the enhancement factor of the $\mathrm{PF}_{\mathrm{opt}}$, but also of ZT_{opt} for the low-dimensional semiconductors.

6.4 The universal curve for ZT

Let us now compare the ZT_{opt} formula as a function of α with various experimental data. In Fig. 6.3, we plot theoretical ZT_{opt} (solid curve) as a function of α [Eq. (6.14)]. Here ZT_{opt} merely depends on $\mathrm{PF}_{\mathrm{opt}}$, κ_{l}, and T, even though the PF and ZT are optimized at different chemical potentials, i.e., $\eta_{\mathrm{opt}}^{\mathrm{PF}} = 0$ and $\eta_{\mathrm{opt}}^{ZT} = -W_0(\alpha)$, respectively. Hence, ZT_{opt} for various materials with different dimensions can be compared directly with the universal theoretical curve. The experimental data (symbols) in Fig. 6.3 are extracted from plots of ZT_{opt}, $\mathrm{PF}_{\mathrm{opt}}$, and κ_{l} in Refs. [16, 54, 104, 103, 105] by

---

Fig. 6.3: Fig/chapter6-fig3.pdf

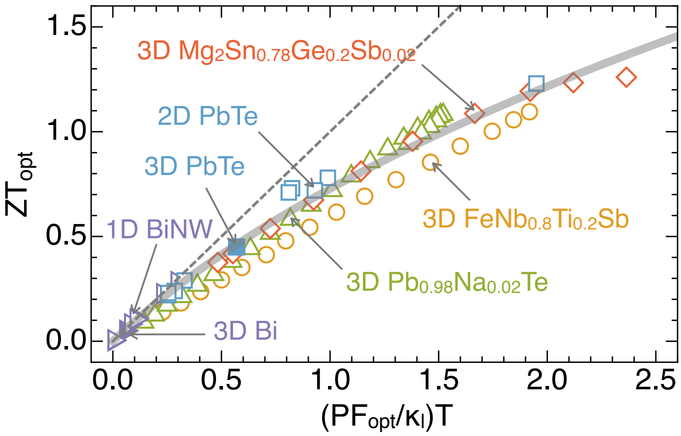

Figure 6.3 $ZT_{\rm opt}$ as a function of $\alpha = ({\rm PF}_{\rm opt}/\kappa_{\rm l})T$. The solid line denotes the theoretical curve from Eq. (6.14), while the dashed line is the plot of $ZT_{\rm opt} = \alpha$ as a guide for eyes. The symbols represent experimental results of 1D Bi nanowires (▷) and 3D Bi (▶) [16], 2D PbTe quantum wells (□) and 3D PbTe (■) [54], 3D $\rm Pb_{0.98}Na_{0.02}Te$ (△) [103], 3D $\rm FeNb_{0.8}Ti_{0.2}Sb$ (○) [104], and 3D $\rm Mg_2Sn_{0.78}Ge_{0.2}Sb_{0.02}$ (◇) [105], respectively.

using digitizer software. These data include 1D Bi nanowires of different diameters ($\sim 38 - 290$ nm) along with bulk 3D Bi at room temperature [16], 2D PbTe quantum wells of different thicknesses ($\sim 1.9 - 4.0$ nm) along with 3D PbTe at room temperature [54], also 3D $\rm Pb_{0.98}Na_{0.02}Te$ [103], 3D $\rm FeNb_{0.8}Ti_{0.2}Sb$ [104], and 3D $\rm Mg_2Sn_{0.78}Ge_{0.2}Sb_{0.02}$ [105] at different temperatures ($\sim 300 - 1100$ K).

As is seen in Fig. 6.3, all experimental data for 1D, 2D, and 3D materials fit the universal theoretical curve from Eq. (6.14). The values of $ZT_{\rm opt}$ monotonically increase as a function of α and thus we can say that any semiconductor should have $\alpha > 4.5$ to obtain $ZT_{\rm opt} > 2$ thought it is not shown in Fig. 6.3. For $\alpha < 0.3$ (high T or high ${\rm PF}_{\rm opt}$), we have $\eta_{\rm opt}^{ZT} \sim \eta_{\rm opt}^{\rm PF}$. In this case, $ZT_{\rm opt} \sim ({\rm PF}_{\rm opt}/\kappa_{\rm l})T$ [see the dotted line in Fig. 6.3]. On the other hand, for $\alpha > 0.3$, we have $\eta_{\rm opt}^{ZT} < \eta_{\rm opt}^{\rm PF}$ that eventually results in a nonlinear function of $ZT_{\rm opt}$ versus $({\rm PF}_{\rm opt}/\kappa_{\rm l})T$. The main benefit of using the universal curve of Fig. 6.3 is that it provides a new way to directly calculate $ZT_{\rm opt}$ from ${\rm PF}_{\rm opt}$ and $\kappa_{\rm l}$ without any necessity to check the electron thermal conductivity κ_e nor the optimum chemical potential $\eta_{\rm opt}^{ZT}$. This should be useful for researchers of thermoelectric field.

Chapter 7

Conclusions

In this thesis, we have discussed theoretical calculation for the thermoelectric (TE) properties (power factor PF and figure of merit ZT) of two-dimensional materials. Calculations have been performed for the PF of the low-dimensiona materials (1D and 2D) based on the one-band model. Then the PF and ZT of the 2D materials, in particular, InSe and tetradymites (Bi_2Se_3, Bi_2Te_2Se, and Bi_2Te_2S), are calculated by using the Boltzmann transport theory and density functional theory (DFT) calculations. Using the analytical approach based on the one-band model, we also derive a directly relationship between the PF and ZT despite of the fact that the two quantities are generally given by different values for a given value of chemical potential. Our finding can then be divided into four parts as follows.

1 - Quantum effects on thermoelectric power factor of low-dimensional semiconductors (Chapter 3)

We have shown that the largest PF values is obtained for low-dimensional materials by decreasing both the confinement length L and the thermal de Broglie wavelength Λ while keeping $L < \Lambda$. Depending on the dimension of materials, there is a different interplay between L and Λ to enhance the power factor. A simple analytical formula [Eq. (3.10)] based on the one-band model has been derived to describe the quantum effects on the PF in 1D, 2D, and 3D materials. We would suggest to experimentalists to check $L < \Lambda$ in order to enhance PF for different dimensions of their semiconductors. Recently, our theory has attracted experimentalists. For example, Prof. Ohta group (Hokkaido University) has shown that the PF of two-dimensional (2D) GaN are enhanced by $L < \Lambda$ [58].

2 - Thermoelectric properties of two-dimensional InSe (Chapter 4)

The 2D monolayer InSe has been shown to be a potential thermoelectric material with high PF (0.049 W/K^{2}m at 300K). The high PF of the monolayer InSe is attributed to both its Seebeck coefficient S and electrical conductivity σ. The large S originates from the moderate (about 2 eV) bandgap of the monolayer InSe as an indirect gap semiconductor, while its large σ is due to its unique two-dimensional density of states (DOS), which consists of an almost constant DOS near the conduction band bottom and a sharp peak near the valence band top. We also show that the convergence of multivalley bands (CMB) can be a good strategy to improve the TE performance of the monolayer InSe. From the analytical formula within the two-band model [Eq. (4.5)], we find that the PF can be greatly enhanced by tuning the valley splitting energy ΔE within a few $k_{\mathrm{B}}T$, and the peak values of PF can be achieved at $\Delta E = 0$. Using first-principles calculations combined with the Boltzmann transport theory, we demonstrate that the PF and ZT of the monolayer InSe can be significantly enhanced by both valence (p-type) and conduction (n-type) valley convergence under a biaxial compressive stress (1.16 GPa) that should be experimentally accessible. The PF is enhanced by nearly a factor of 3 by the CMB in both the n-type and p-type InSe.

3 - Thermoelectric properties of two-dimensional tetradymites (Chapter 5)

We have performed ab initio calculations of the full thermoelectric transport properties for the 2D single quintuple-layers (QL) $\mathrm{M_2X_3}$ tetradymites, considering the electron-phonon and phonon-phonon interactions, as well as the polar interaction. We show that the unique electronic structure in the single-QL $\mathrm{M_2X_3}$, represented by its highly non-parabolic band in the conduction bands and a multi-valleys convergence (CMB) in the valance bands, lead to high PF of about $0.20 - 0.25$ W/mK^2 at room temperature. In addition, the single-QL $\mathrm{M_2X_3}$ has a very low intrinsic lattice thermal conductivity $\sim 1.5 - 2.0$ W/mK because of the heavy atomic (Bi, Te, Se, and S) masses and high polarizability of bonds, which produce a low phonon group velocities and strong anharmonic scattering. The high ZT values are thus achieved for the single-QL $\mathrm{M_2X_3}$. The maximum ZT is found in the p-type single-QL $\mathrm{Bi_2Te_2Se}$ from 1.4 to 2.0 at operating temperature of $300 - 500$ K with the optimized carrier concentrations about 5×10^{11} cm^{-2}. Our results present not only the high ZT materials at near room-temperature and highlight the importance of the CMB to improve the PF, but also provide a new approach to designing high TE performance 2D tetradymites.

4 - Universal curve of thermoelectric figure of merit for semiconductors (Chapter 6)

We have shown that the simple analytical formulas [Eq. (6.14)] based on the one-band model can directly relate the optimum figures of merit ZT_{opt} with the optimum power factors $\mathrm{PF}_{\mathrm{opt}}$ of semiconductors. By introducing the material parameter $\alpha = \mathrm{PF}_{\mathrm{opt}} T/\kappa_{\mathrm{l}}$, where κ_{l} is the lattice thermal conductivity, we can obtain the universal curve of ZT_{opt} as a function of α combining both bulk and low-dimensional semiconductors, in which ZT_{opt} monotonically increases in a slightly saturating way with increasing α. Since this approach reduces parameters such as electron thermal conductivity κ_{e} and optimized chemical potential η_{opt} in the calculation of ZT_{opt}, we think that it will help researchers to better identify new thermoelectric materials in the future.

Appendix A

Thermodynamic uncertainty principle

Let us consider an ideal gas moving randomly in a trapping potential. We assume that the space of the potential has the volume $V \sim L^d$, where L is the confinement length (or potential size) and $d = 1, 2, 3$ denotes the dimension of the system. In the classical system, the position of the wall in the container is well defined: at the wall, the particle is reflected back into the container, also known as the classical turning point. On the other hand, in a quantum system, the particle is reflected before reaching the classical turning point or the particle tunnels over the turning point by the uncertainty principle. That means that L has an uncertainty ΔL due to the uncertainty principle that results in uncertainty of volume ΔV. We can use the law of ideal gas to define the pressure (i.e., impulse of gas atoms per unit area by the reflection) as

$$P = 2p\rho v, \tag{A.1}$$

where p is the component of momentum normal to the wall, ρ is the gas density, v is the averaged velocity of gas, and ρv is the number of collisions per a unit time. In quantum mechanics, the Heisenberg's uncertainty principle tell us,

$$\Delta p \Delta L \geq \frac{\hbar}{2}, \tag{A.2}$$

where $\hbar$ is the Planck constant. After substituting Eq. (A.1), the Eq. (A.2) can be rewritten as

$$\Delta P \Delta L \geq \hbar \rho v. \tag{A.3}$$

Since the equations of state for the ideal gas is expressed as $PV = Nk_{\mathrm{B}}T$, where $N = pV$ is the total number of particles, T is the temperature of the gas, and k_{B} is the Boltzmann constant, the gas density can take the form $\rho = P/k_{\mathrm{B}}T$. In addition, the averaged velocity of the particle in the Boltzmann distribution can be given as

$$v^2 = \frac{d\, k_{\mathrm{B}}T}{m}, \tag{A.4}$$

where m is the effective mass of the particle. Inserting these quantities into Eq. (A.3) gives

$$\frac{\Delta P}{P}\frac{\Delta L}{L} \geq \sqrt{\frac{d}{2\pi}}\frac{\Lambda}{L}, \tag{A.5}$$

where $\Lambda = (2\pi\hbar^2/k_{\mathrm{B}}Tm)^{1/2}$ is defined by the thermal de Broglie wavelength of a particle. Since the volume V is proportional to L^d, then we get

$$\frac{\Delta P}{P}\frac{\Delta V}{V} \geq \frac{d^{3/2}}{\sqrt{2\pi}}\frac{\Lambda}{L}, \tag{A.6}$$

This is the generalized thermodynamic uncertainty principle for an ideal gas. This means that when L is comparable with Λ, such as $L \leq (d^{3/2}/\sqrt{2\pi})\Lambda$, the pressure and the volume cannot be treated as commuting observable. In other words, the system becomes the quantum system.

Appendix B

The Lambert W function

The Lambert W function is defined as a multivalued complex function that satisfy the following equation:

$$W(\alpha) = \alpha e^{-W(\alpha)}, \quad \alpha \in \mathbb{C}. \tag{B.1}$$

Since Eq. (B.1) always has an infinite number of solution in the complex Liemann plane, we expect the multivaluedness of the W function. The solutions of Eq. (B.1) are indexed by the integer variable j and are called the branches of the W function, W_j, for $j \in \mathbb{Z}$. In particular, the solutions of Eq. (B.1) in the calculation of ZT_{opt} correspond to real $\alpha \in [0, \infty)$. In this case there can be a real solution, corresponding to the principal branch of the W function, i.e. $W_0(\alpha) \in [0, \infty)$.

The W_0 function can be written in terms of series expansion as follows [106],

$$\begin{aligned} W_0(\alpha) =& \sum_{n=1}^{\infty} \frac{(-n)^{n-1}}{n!} \alpha^n \\ =& \ \alpha - \alpha^2 + \frac{3}{2}\alpha^3 - \frac{8}{3}\alpha^4 + \frac{125}{24}\alpha^5 \\ & - \frac{54}{5}\alpha^6 + \frac{16807}{720}\alpha^7 + \cdots . \end{aligned} \tag{B.2}$$

Figure B.1 shows $W_0(\alpha)$ as a function of α when $\alpha \in [0, \infty)$.

Fig. B.1: Fig/appendix-fig2.pdf

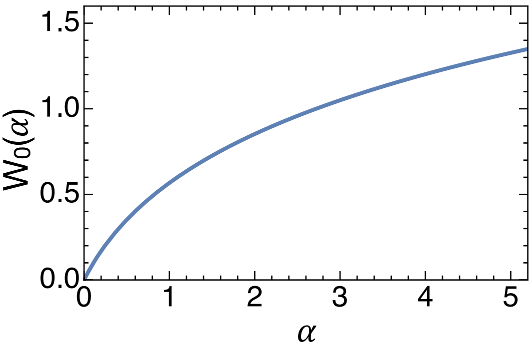

Figure B.1 The real principal branch of the W function in the case of $a \in [0, \infty)$.

Publication list

Journals

(1) D. V. Truong, N. T. Hung, T. Shimada and T. Kitamura, Ab initio study of shear strain effects on ferroelectricity at $PbTiO_3$ thin films, *Surf. Sci.* **606**, 1131-1339 (2012).

(2) N. T. Hung and D. V. Truong, Ab initio study of structural transition and pseudoelasticity in Cu nanowires, *Surf. Sci.* **641**, 1-5 (2015).

(3) N. T. Hung, A. R. T. Nugraha, E. H. Hasdeo, M. S. Dresselhaus and R. Saito, Diameter dependence of thermopower of semiconducting carbon nanotubes, *Phys. Rev. B* **92**, 165426 (2015).

(4) N. T. Hung, D. V. Truong, V. V. Thanh and R. Saito, Intrinsic strength and failure behaviors of ultra-small single-walled carbon nanotubes, *Comput. Mater. Sci.* **114**, 167-171 (2016).

(5) N. T. Hung, E. H. Hasdeo, A. R. T. Nugraha, M. S. Dresselhaus and R. Saito, Quantum effect in the thermoelectric power factor of low-dimensional semiconductors, *Phys. Rev. Lett.* **117**, 036602 (2016).

(6) N. T. Hung, A. R. T. Nugraha and R. Saito, Charge-induced electrochemical actuation of armchair carbon nanotube bundles, *Carbon* **118**, 278-284 (2017).

(7) N. T. Hung, A. R. T. Nugraha and R. Saito, High-performance three-dimensional carbon Archimedean lattices electromechanical actuators, *Carbon* **125**, 472-479 (2017).

(8) N. T. Hung, A. R. T. Nugraha and R. Saito, Size effect in thermoelectric power factor of nondegenerate and degenerate low-dimensional semiconductors, *Mater. Today: Proc.* **4**, 12368-12373 (2017).

(9) N. T. Hung, A. R. T. Nugraha and R. Saito, Two-dimensional InSe as a potential thermoelectric material, *Appl. Phys. Lett.* **111**, 092107 (2017).

(10) N. T. Hung, A. R. T. Nugraha and R. Saito, Two-dimensional MoS_2 electrochemical actuator, *J. Phys. D: Appl. Phys.* **51**, 075306 (2018).

(11) N. T. Hung, A. R. T. Nugraha and R. Saito, Universal curve of optimum thermoelectric figure of merit for bulk and low-dimensional semiconductors, *Phys. Rev. Appl.* **9**, 024019 (2018).

(12) Q. D. Truong*, N. T. Hung*, Y. Nakayasu, K. Nayuki, Y. Sasaki, M. K. Devaraju, L. C. Yin, T. Tomai, R. Saito and I. Honma, Inversion domain boundaries in in $MoSe_2$ layers, *RSC Adv.* **8**, 33391–33397 (2018) (*Equal contribution).

(13) V. V. Thanh, N. T. Hung, D. V. Truong, Charge-induced electromechanical actuation of Mo- and W-dichalcogenide monolayers, *RSC Adv.* **8**, 38667-38672 (2018).

(14) N. T. Hung, A. R. T. Nugraha, T. Yang, Z. Zhang and R. Saito, Thermoelectric performance of monolayer InSe improved by convergence of multivalley bands, *J. Phys. Appl.* **125**, 082502-1-8 (2019).

(15) B. Dong, Z. Wang, N. T. Hung, A. R. Oganov, T. Yang, R. Saito and Z. Zhang, New two-dimensional phase of tin chalcogenides: candidates for high-performance thermoelectric materials, *Phys. Rev. Mater.* **3**, 013405-1-9 (2019).

(16) N. T. Hung, A. R. T. Nugraha and R. Saito, Designing high-performance thermoelectrics in two-dimensional tetradymites, *Nano Energy* **58**, 743-749 (2019).

Book chapters

(1) R. Saito, A. R. T. Nugraha, E. H. Hasdeo, N. T. Hung and W. Izumida, Electronic and optical properties of single wall carbon nanotubes, *in Single-Walled Carbon Nanotubes: Preparation, Property and Application*, Ed. Y. Li and S. Maruyama, Springer, Beijing, *Top. Curr. Chem.* **375**, 1-24 (2017).

Invited talks

- N. T. Hung, Thermoelectric properties of low-dimensional materials, *The 7th Fullerenes-Nanotubes-Graphene Young Researcher Meeting*, 12/9/2017, Kyoto, Japan.

- N. T. Hung, Enhancing the thermoelectric properties of low-dimensional materials, *Invited Seminar at Institute of Metal Research, Chinese Academy of Sciences*, 6/12/2017, Shenyang, China.

Contributed talks

- N. T. Hung, A. R. T. Nugraha, and R. Saito, Thermoelectricity of low-dimensional semiconductors, *ATI 2018 Nano Carbon*, 19-20/7/2016, Sendai, Japan.

- N. T. Hung, A. R. T. Nugraha, and R. Saito, Size effect in thermoelectric performance of carbon nanotubes and other low-dimensional semiconductors, *The*

18th International Conference on the Science and Application of Nanotubes and Low-dimensional Materials, 25-30/6/2017, Belo Horizonte, Brazil.

- N. T. Hung, A. R. T. Nugraha, and R. Saito, Is there an upper limit of thermoelectric figure-of-merit?, *ATI 2018 Nano Carbon*, 9-10/8/2017, Sendai, Japan.
- N. T. Hung, Quantum effects in thermoelectric performance of 1d and 2d semiconductors, *The 10th Vietnam - Japan Scientific Exchange Meeting*, 9/9/2017, Tokyo, Japan.
- N. T. Hung and R. Saito, Mo_3S_{11} polymer as high capacity anion redox electrodes for sodium-ion battery, *ATI 2018 Nano Carbon*, 1-2/8/2018, Sendai, Japan.

Posters

- N. T. Hung and R. Saito, Thermoelectricpowerof carbon nanotubes from first principles, *The 48th Fullerenes-Nanotubes-Graphene General Symposium*, 21-23/2/2015, Tokyo, Japan.
- N. T. Hung, A. R. T. Nugraha, and R. Saito, An atlas of thermoelectric power of semiconducting carbon nanotubes, *The 49th Fullerenes-Nanotubes-Graphene General Symposium*, 7-9/12/2015, Kyushu, Japan.
- N. T. Hung, A. R. T. Nugraha, and R. Saito, Theory of optimized power factor of low-dimensional semiconductors and application to semiconducting carbon nanotubes, *The 51th Fullerenes-Nanotubes-Graphene General Symposium*, 7-9/9/2016, Hokkaido, Japan.
- N. T. Hung, A. R. T. Nugraha, and R. Saito, Theory of optimized power factor of low-dimensional semiconductors and applicationto semiconducting carbon nanotubes, *7th A3 Symposium on Emerging Materials: Nanomaterials for Electronics, Energy and Environment*, 30/10-3/11/2016, Buyeo, Korea.
- N. T. Hung, A. R. T. Nugraha, and R. Saito, Artificial muscle using single wall carbon nanotube bundles, *The 52th Fullerenes-Nanotubes-Graphene General Symposium*, 1-3/3/2017, Tokyo, Japan.
- N. T. Hung, A. R. T. Nugraha, and R. Saito, Size effects in thermoelectric power factor of nondegenerate and degenerate low-dimensional semiconductors, *The 2017 E-MRS Spring Meeting*, 22-26/5/2017, Strasbourg, France.
- N. T. Hung, A. R. T. Nugraha, and R. Saito, Designing three-dimensional carbon Archimedean lattices for artificial muscle, *The 53th Fullerenes-Nanotubes-Graphene General Symposium*, 13-15/9/2017, Kyoto, Japan.

- N. T. Hung, A. R. T. Nugraha, and R. Saito, Improving thermoelectric performance of monolayer semiconductors beyond the confinement effect, *19th International Conference on the Science and Application of Nanotubes and Low-dimensional Materials*, 15-20/7/2018, Beijing, China.
- N. T. Hung, Q. D. Truong, L. C. Yin, P. D. Tran, I. Honma, and R. Saito, Molybdenum sulfide polymer with high capacity for sodium-ion battery, *9th A3 Symposium on Emerging Materials: Nanomaterials for Electronics, Energy and Environment*, 29-31/10/2018, Kyoto, Japan.

Bibliography

[1] L. D. Hicks and M. S. Dresselhaus, Phys. Rev. B 47, 12727 (1993).

[2] L. D. Hicks and M. S. Dresselhaus, Phys. Rev. B 47, 16631 (1993).

[3] A. I. Boukai, Y. Bunimovich, J. Tahir-Kheli, J. K. Yu, W. A. Goddard Iii, and J. R. Heath, Nature 451, 168–171 (2008).

[4] A. I. Hochbaum, R. Chen, R. D. Delgado, W. Liang, E. C. Garnett, M. Najarian, A. Majumdar, and P. Yang, Nature 451, 163–167 (2008).

[5] H. J. Goldsmid, Introduction to Thermoelectricity (Springer-Verlag, Berlin Heidelberg, 2010).

[6] C. B. Vining, Nature 413, 577–578 (2001).

[7] H. B. Callen, Phys. Rev. 73, 1349 (1948).

[8] D. M. Rowe, Thermoelectrics handbook: macro to nano (CRC press, Boca Ratcon, 2005).

[9] S. K. Yee, S. LeBlanc, K. E. Goodson, and C. Dames, Energy Enviro. Sci. 6, 2561–2571 (2013).

[10] C. B. Vining, Nature Mater. 8, 83–85 (2009).

[11] A. Majumdar, Science 303, 777–778 (2004).

[12] W. Liu, H. S. Kim, S. Chen, Q. Jie, B. Lv, M. Yao, Z. Ren, C. P. Opeil, S. Wilson, C. W. Chu, and Z. Ren, Proc. Natl. Acad. Sci. 112, 3269–3274 (2015).

[13] W. Liu, H. S. Kim, Q. Jie, and Z. Ren, Scripta Mater. 111, 3–9 (2016).

[14] J. P. Heremans, M. S. Dresselhaus, L. E. Bell, and D. T. Morelli, Nature Nanotechnol. 8, 471–473 (2013).

[15] L. D. Hicks, T. C. Harman, X. Sun, and M. S. Dresselhaus, Physical Review B 53(16), R10493 (1996).

[16] J. Kim, S. Lee, Y. M. Brovman, P. Kim, and W. Lee, Nanoscale 7, 5053–5059 (2015).

[17] Q.H. Wang, K. Kalantar-Zadeh, A. Kis, J. N. Coleman, and M. S. Strano, Nat. Nanotechnol. 7, 699–712 (2012).

[18] S. Z. Butler, S. M. Hollen, Linyou Cao, Y. Cui, J. A. Gupta, H. R. Gutiérrez, T. F. Heinz, S. S. Hong, J. Huang, A. F. Ismach, E. Johnston-Halperin, M. Kuno, V. V. Plashnitsa, R. D. Robinson, R. S. Ruoff, S. Salahuddin, J. Shan, L. Shi, M. G. Spencer, M. Terrones, W. Windl, and J. E. Goldberger, ACS Nano 7, 2898–2926 (2013).

[19] A. K. Geim and I. V. Grigorieva, Nature 499, 419–425 (2013).

[20] N. T. Hung, E. H. Hasdeo, A. R. T. Nugraha, M. S. Dresselhaus, and R. Saito, Phys. Rev. Lett. 117, 036602 (2016).

[21] Y. Saito, T. Iizuka, T. Koretsune, R. Arita, S. Shimizu, and Y. Iwasa, Nano Lett. 16, 4819–4824 (2016).

[22] R. Fei, A. Faghaninia, R. Soklaski, J. A. Yan, C. Lo, and L. Yang, Nano Lett. 14, 6393–6399 (2014).

[23] Bolin Liao, Jiawei Zhou, Bo Qiu, Mildred S. Dresselhaus, and Gang Chen, Phys. Rev. B 91, 235419 (Jun 2015).

[24] M. Yoshida, T. Iizuka, Y. Saito, M. Onga, R. Suzuki, Y. Zhang, Y. Iwasa, and S. Shimizu, Nano Lett. 16, 2061–2065 (2016).

[25] M. Kayyalha, J. Maassen, M. Lundstrom, L. Shi, and Y. P. Chen, J. Appl. Phys. 120, 134305 (2016).

[26] D. Wickramaratne, F. Zahid, and R. K. Lake, J. Chem. Phys. 140, 124710 (2014).

[27] V. Zólyomi, N. D. Drummond, and V. I. Fal’ko, Phys. Rev. B 87, 195403 (2013).

[28] V. Zólyomi, N. D.. Drummond, and V. I. Fal’ko, Phys. Rev. B 89, 205416 (2014).

[29] N. T. Hung, A. R. T. Nugraha, and R. Saito, Appl. Phys. Lett. 111, 092107 (2017).

[30] D. A. Bandurin, A. V. Tyurnina, L. Y. Geliang, A. Mishchenko, V. Zólyomi, S. V. Morozov, R. K. Kumar, R. V. Gorbachev, Z. R. Kudrynskyi, S. Pezzini, Z. D. Kovalyuk, U. Zeitler, K. S. Novoselov, Patané, L. Eaves, I. V. Grigorieva, V. I. Fal’ko, A. K. Geim, and Y. Cao, Nat. Nanotech. 12, 223 (2017).

[31] J. S. Rhyee, K. H. Lee, S. M. Lee, E. Cho, S. I. Kim, E. Lee, Y. Seung Kwon, J. H. Shim, and G. Kotliar, Nature 459, 965–968 (2009).

[32] D. Wickramaratne, F. Zahid, and R. K. Lake, J. Appl. Phys. 118, 075101 (2015).

[33] J. P. Heremans, R. J. Cava, and N. Samarth, Nat. Rev. Mater. 2, 17049 (2017).

[34] S. I. Kim, K. H. Lee, H. A. Mun, H. S. Kim, S. W. Hwang, J. W. Roh, D. J. Yang, W. H. Shin, X. S. Li, Y. H. Lee, G. J. Snyder, and S. W. Kim, Science 348, 109–114 (2015).

[35] K. Park, J. J. Heremans, V. W. Scarola, and D. Minic, Phys. Rev. Lett. 105, 186801 (2010).

[36] Z. Li, N. Miao, J. Zhou, Z. Sun, Z. Liu, and H. Xu, Nano Energy 43, 285–290 (2018).

[37] S. Sharma and U. Schwingenschlogl, ACS Energy Lett. 1(4), 875–879 (2016).

[38] G. D. Mahan and J. O. Sofo, Proc. Natl. Acad. Sci. U.S.A. 93, 7436–7439 (1996).

[39] C. Jeong, R. Kim, and M. S. Lundstrom, J. Appl. Phys. 111, 113707 (2012).

[40] R. P. Chasmar and R. Stratton, J. Electron. Control 7, 52–72 (1959).

[41] M. Lundstrom, Fundamentals of carrier transport (Cambridge University Press, New York, 2009).

[42] W. S. Liu, Q. Zhang, Y. Lan, S. Chen, X. Yan, Q. Zhang, H. Wang, D. Wang, G. Chen, and Z. Ren, Adv. Energy Mater. 1, 577–587 (2011).

[43] J. M. Ziman. Electrons and phonons, 1960.

[44] J. Callaway, Phys. Rev. 113, 1046 (1959).

[45] M. G. Holland, Phys. Rev. 132, 2461 (1963).

[46] R. A. Guyer and J. A. Krumhansl, Phys. Rev. 148, 766 (1966).

[47] S. Giorgini, L. P. Pitaevskii, and S. Stringari, Rev. Mod. Phys. 80(4), 1215 (2008).

[48] J. Zhou, R. Yang, G. Chen, and M. S. Dresselhaus, Phys. Rev. Lett. 107, 226601 (2011).

[49] D. Chattopadhyay and H. J. Queisser, Rev. Mod. Phys. 53, 745 (1981).

[50] W. Zawadzki and W. Szymańska, J. Phys. Chem. Solids 32(6), 1151–1174 (1971).

[51] J. Moon, J. H. Kim, Z. C. Y. Chen, J. Xiang, and R. Chen, Nano Lett. 13, 1196–1202 (2013).

[52] J. E. Cornett and O. Rabin, Phys. Rev. B 84, 205410 (2011).

[53] X. Sun, S. B. Cronin, J. Liu, K. L. Wang, T. Koga, M. S. Dresselhaus, and G. Chen. In Proc. 18th Int. Conf. Thermoelectrics, pages 652–655. IEEE, 1999.

[54] T. C. Harman, D. L. Spears, and M. J. Manfra, J. Electron. Mater. 25, 1121–1127 (1996).

[55] L. D. Hicks. PhD thesis, MIT, 1996.

[56] L. Weber and E. Gmelin, Appl. Phys. A 53, 136–140 (1991).

[57] Y. Zhang, B. Feng, H. Hayashi, C. P. Chang, Y. M. Sheu, I. Tanaka, Y. Ikuhara, and H. Ohta, Nat. Commun. 9, 2224 (2018).

[58] H. Ohta, S. W. Kim, S. Kaneki, A. Yamamoto, and T. Hashizume, Adv. Sci. 5, 1700696 (2018).

[59] C. Lee, Q. Li, W. Kalb, X. Z. Liu, H. Berger, R. W. Carpick, and J. Hone, Science 328, 76–80 (2010).

[60] Y. Hirayama, T. Saku, and Y. Horikoshi, Phys. Rev. B 39, 5535 (1989).

[61] J. R. Sootsman, H. Kong, C. Uher, J. J. D'Angelo, C.-I. Wu, T. P. Hogan, T. Caillat, and M. G. Kanatzidis, Angew. Chem. 120, 8746 (2008).

[62] Paolo Giannozzi, Stefano Baroni, Nicola Bonini, Matteo Calandra, Roberto Car, Carlo Cavazzoni, Davide Ceresoli, Guido L Chiarotti, Matteo Cococcioni, Ismaila Dabo, Andrea Dal Corso, Stefano de Gironcoli, Stefano Fabris, Guido Fratesi, Ralph Gebauer, Uwe Gerstmann, Christos Gougoussis, Anton Kokalj, Michele Lazzeri, Layla Martin-Samos, Nicola Marzari, Francesco Mauri, Riccardo Mazzarello, Stefano Paolini, Alfredo Pasquarello, Lorenzo Paulatto, Carlo Sbraccia, Sandro Scandolo, Gabriele Sclauzero, Ari P Seitsonen, Alexander Smogunov, Paolo Umari, and Renata M Wentzcovitch, J. Phys. Condens. Matter 21(39), 395502 (2009).

[63] J. P. Perdew and A. Zunger, Phys. Rev. B 23, 5048 (1981).

[64] We used the In.pz-hgh.UPF and Se.pz-hgh.UPF pseudopotentials from http://www.quantum-espresso.org.

[65] L. Debbichi, O. Eriksson, and S. Lebègue, J. Phys. Chem. Lett. 6, 3098–3103 (2015).

[66] C. G. Broyden, IMA J. Appl. Math. 6, 76–90 (1970).

[67] R. Fletcher, Comput. J. 13, 317–322 (1970).

[68] Donald Goldfarb, Math. Comput. 24, 23–26 (1970).

[69] D. F. Shanno, Math. Comput. 24, 647–656 (1970).

[70] S. Poncé, E.R. Margine, C. Verdi, and F. Giustino, Comput. Phys. Commun. 209, 116–133 (2016).

[71] Stefano Baroni, Stefano de Gironcoli, Andrea Dal Corso, and Paolo Giannozzi, Rev. Mod. Phys. 73, 515–562 (Jul 2001).

[72] N. T. Hung, A. R. T. Nugraha, and R. Saito, Appl. Phys. Lett. 111, 092107 (2017).

[73] A. Nissimagoudar, J. Ma, Y. Chen, and W. Li, J. Phys. Condens. Matter 29, 335702 (2017).

[74] J. P. Perdew, K. Burke, and M. Ernzerhof, Phys. Rev. Lett. 77, 3865 (1996).

[75] N. T. Hung, A. R. T. Nugraha, E. H. Hasdeo, M. S. Dresselhaus, and R. Saito, Phys. Rev. B 92(16), 165426 (2015).

[76] R. Kim, S. Datta, and M. S. Lundstrom, J. Appl. Phys. 105, 034506 (2009).

[77] Y. Pei, X. Shi, A. LaLonde, H. Wang, L. Chen, and G. J. Snyder, Nature 473, 66–69 (2011).

[78] Y. Tang, Z. M. Gibbs, L. A. Agapito, G. Li, H. S. Kim, M. B. Nardelli, S. Curtarolo, and G. J. Snyder, Nat. Mater. 14, 1223 (2015).

[79] W. Liu, X. Tan, K. Yin, H. Liu, X. Tang, J. Shi, Q. Zhang, and C. Uher, Phys. Rev. Lett. 108, 166601 (2012).

[80] H. Jin, J. Li, Y. Dai, and Y. Wei, Phys. Chem. Chem. Phys. 19, 4855–4860 (2017).

[81] Z. Jin, Q. Liao, H. Fang, Z. Liu, W. Liu, Z. Ding, T. Luo, and N. Yang, Sci. Rep. 5, 18342 (2015).

[82] G. H. Hong, Y. Teng, T. Peng, and Z. Zhi-Dong, Chinese Phys. B 23, 017201 (2013).

[83] N. T. Hung, A. R. T. Nugraha, T. Yang, Z. Zhang, and R. Saito, J. Appl. Phys. 125, 082502 (2019).

[84] F. Giustino, Rev. Mod. Phys. 89, 015003 (2017).

[85] J. M. Ziman, , 1960).

[86] S. Poncé, E. R. Margine, C. Verdi, and F. Giustino, Comput. Phys. Commun. 209, 116–133 (2016).

[87] W. Li, J. Carrete, N. A. Katcho, and N. Mingo, Comput. Phys. Commun. 185, 1747–1758 (2014).

[88] P. Gehring, B. F. Gao, M. Burghard, and K. Kern, Nano Lett. 12, 5137–5142 (2012).

[89] J. Zhang, Z. Peng, A. Soni, Y. Zhao, Y. Xiong, B. Peng, J. Wang, M. S. Dresselhaus, and Q. Xiong, Nano Lett. 11, 2407–2414 (2011).

[90] D. Kong, W. Dang, J. J. Cha, H. Li, S. Meister, H. Peng, Z. Liu, and Y. Cui, Nano Lett. 10, 2245–2250 (2010).

[91] V. A. Kulbachinskii, V. G. Kytin, A. A. Kudryashov, and P. M. Tarasov, J. Solid State Chem. 193, 47–52 (2012).

[92] X. Chen, D. Parker, and D. J. Singh, Sci. Rep. 3, 3168 (2013).

[93] T. H. Liu, J. Zhou, M. Li, Z. Ding, Q. Song, B. Liao, L. Fu, and G. Chen, Proc. Natl. Acad. Sci. U.S.A page 201715477 (2018).

[94] N. Mounet, M. Gibertini, P. Schwaller, D. Campi, A. Merkys, A. Marrazzo, T. Sohier, I. E. Castelli, A. Cepellotti, G. Pizzi, and N. Marzari, Nat. Nanotech. 13, 246 (2018).

[95] N. T. Hung, A. R .T. Nugraha, and R. Saito, Phys. Rev. Applied 9, 024019 (2018).

[96] H. W. L. Alves, A. R. R. Neto, L. M. R. Scolfaro, T. H. Myers, and P. D. Borges, Phys. Rev. B 87(11), 115204 (2013).

[97] R. H. Lyddane, R. G. Sachs, and E. Teller, Phys. Rev. 59, 673 (1941).

[98] M. D. Nielsen, V. Ozolins, and J. P. Heremans, Energy Environ. Sci. 6, 570–578 (2013).

[99] Y. S. Hor, A. Richardella, P. Roushan, Y. Xia, J. G. Checkelsky, A. Yazdani, M. Z. Hasan, N. P. Ong, and R. J. Cava, Phys. Rev. B 79, 195208 (2009).

[100] H. Yuan, H. Shimotani, J. Ye, S. Yoon, H. Aliah, A. Tsukazaki, M. Kawasaki, and Y. Iwasa, J. Am. Chem. Soc. 132, 18402–18407 (2010).

[101] Olle Hellman and David A Broido, Physical Review B 90, 134309 (2014).

[102] P. G. Klemens, Proc. R. Soc. Lond. A 208, 108–133 (1951).

[103] L. D. Zhao, H. J. Wu, S. Q. Hao, C. I. Wu, X. Y. Zhou, K. Biswas, J. Q. He, T. P. Hogan, C. Uher, C. Wolverton, V. P. Dravid, and M. G. Kanatzidis, Energy Environ. Sci. 6, 3346–3355 (2013).

[104] C. Fu, T. Zhu, Y. Liu, H. Xie, and X. Zhao, Energy Environ. Sci. 8, 216–220 (2015).

[105] W. Liu, J. Zhou, Q. Jie, Y. Li, H. S. Kim, J. Bao, G. Chen, and Z. Ren, Energy Environ. Sci. 9, 530–539 (2016).

[106] C. Carathéodory, Theory of Functions of a Complex Variable (AMS Chelsea Publishing, New York, 1954).